Convective Scale Interaction: Arc Cloud Lines and the Development and Evolution of Deep Convection

By
James F.W. Purdom

PI: Pete C. Sinclair

Department of Atmospheric Science
Colorado State University
Fort Collins, Colorado

Colorado
State
University

Department of
Atmospheric Science

Paper No. 408

CONVECTIVE SCALE INTERACTION:

ARC CLOUD LINES

AND THE DEVELOPMENT AND

EVOLUTION OF DEEP CONVECTION

by

James Francis Whitehurst Purdom

Department of Atmospheric Science
Colorado State University
Fort Collins, CO 80523

Summer 1986

Atmospheric Science Paper No. 408

ABSTRACT

This paper uses information from satellite data and research
aircraft data to provide new understanding concerning the mesoscale
development and evolution of deep convection in an atmosphere typified
by weak synoptic-scale forcing. The major topic covered is the impor-
tance of convective scale interaction (Purdom, 1979) in the development
and evolution of deep convection. This interaction is shown to manifest
itself as the merger and intersection of thunderstorm outflow boundaries
(arc cloud lines) with other convective lines, areas or boundaries.

Using geostationary satellite visible and infrared data convective
scale interaction is shown to be responsible for over 85% of the intense
convection (colder than $-42^{\circ}C$) over the southeast United States by late
afternoon (6 pm local), and an overwhelming majority of that area's
afternoon rainfall.

To bring into sharper focus the dynamical and thermodynamical
features of these arc cloud lines and their interactions, a series of
small focused research field programs were undertaken in which GOES
data were obtained and analyzed in conjunction with simultaneous
research aircraft measurements, (Sinclair and Purdom, 1983, 1984).
The aircraft observations provided valuable information concerning
critically important regions of the arc cloud line: 1) the cool
outflow region; 2) the density surge line (DSL) interface region; and
3) the sub-cloud region above the DSL. The aircraft observations,

when analyzed with rapid scan satellite data, helped in defining the arc cloud line's life cycle as three evolving stages. In stage 1, the formative stage, the arc cloud line may be thought of as an extension of the parent storm's highly channeled outflow. Convergence of a strong cool outflow jet into the rear of the DSL interface coupled with a solenoidal circulation in that region contributes to a mixed updraft region beneath the arc cloud line. As stage 1 evolves to stage 2, the mature stage, the DSL begins to move as a density current. Convergence in the warm environmental air due to the outwardly moving DSL results in the generation of a warm and positively buoyant updraft along the arc cloud line whose intensity is a function of both the strength of the DSL and the environment into which it is moving. Stage 3, the dissipating stage, is marked by a shallow and slow moving DSL above which weak overshooting thermals may cause cumulus cloud development.

Using satellite image and sounding data, as well as research aircraft information, it is shown how variations in a local environment's ability to support strong convection may be determined. Using this information, coupled with information about the arc cloud line's life cycle, four distinct properties of convective scale interaction are analyzed.

#1. Thunderstorm outflow boundaries may maintain their identity as arc cloud lines for several hours after they have moved away from their parent source.

#2. The arc cloud line outflow boundary can, and often does, cause deep convection to develop along it at distances well over 150 km from its point of generation.

#3. Deep convective development along an outflow boundary is a selective process - it only occurs where the arc cloud line merges with a cumulus region or intersects another boundary. When the arc cloud line moves into clear skies no deep convection develops.

#4. As the cumulus regime evolves on a given day, and much of the cumulus field dies away, the majority of new thunderstorms are confined to arc cloud line intersection points.

The findings presented in this paper were made possible because of a series of focused field programs designed specifically to integrate research aircraft data with geostationary satellite data. This represented the first time in-situ research aircraft measurements have been taken in conjunction with GOES satellite observations of mesoscale phenomena. Intense planning, preparation and field coordination were required to assure success of the field program. Work will continue on the investigation of arc cloud lines using a research aircraft platform in conjunction with geostationary satellite data during the MIST (MIcroburst and Severe Thunderstorm) program to be undertaken in the Huntsville, Alabama area during the summer of 1986.

ACKNOWLEDGEMENTS

TABLE OF CONTENTS

TABLE OF CONTENTS
(cont.)

LIST OF TABLES

LIST OF TABLES
(cont.)

LIST OF FIGURES

LIST OF FIGURES
(cont.)

1.0 INTRODUCTION

The purpose of this paper is to provide new understanding concerning the mesoscale development and evolution of deep convection in a weakly forced atmosphere. The major topic to be covered is the importance of convective scale interaction (Purdom, 1979) in controlling the development and evolution of deep convection. This interaction manifests itself as the merger and intersection of outflow boundaries produced by deep convective storms [arc cloud lines (Purdom, 1973a)] with other convective lines, areas and boundaries. Prior to a recent study using Doppler radar data, (Wilson and Carbone, 1984), this interaction had only been recognized using geostationary satellite imagery. Indeed, thunderstorm evolution that appears as random using operational noncoherent radar has been shown to be well ordered when observed using geostationary satellite imagery and the concept of convective scale interaction (Bohan, 1981; Zehr, 1982).

Figures 1.1a, b and c show the characteristic appearance of arc cloud lines in satellite imagery. Those figures also depict a classic case of convective scale interaction where the arc cloud line interacts with a stationary frontal zone. At that intersection a severe thunderstorm developed! In chapter 3 the arc cloud line phenomena and the concept of convective scale interaction will be illustrated and more fully developed.

The convective storm, and the forces that control its development and evolution, is an important topic for study. Convective storms

small pips
are used for
arc cloud lines
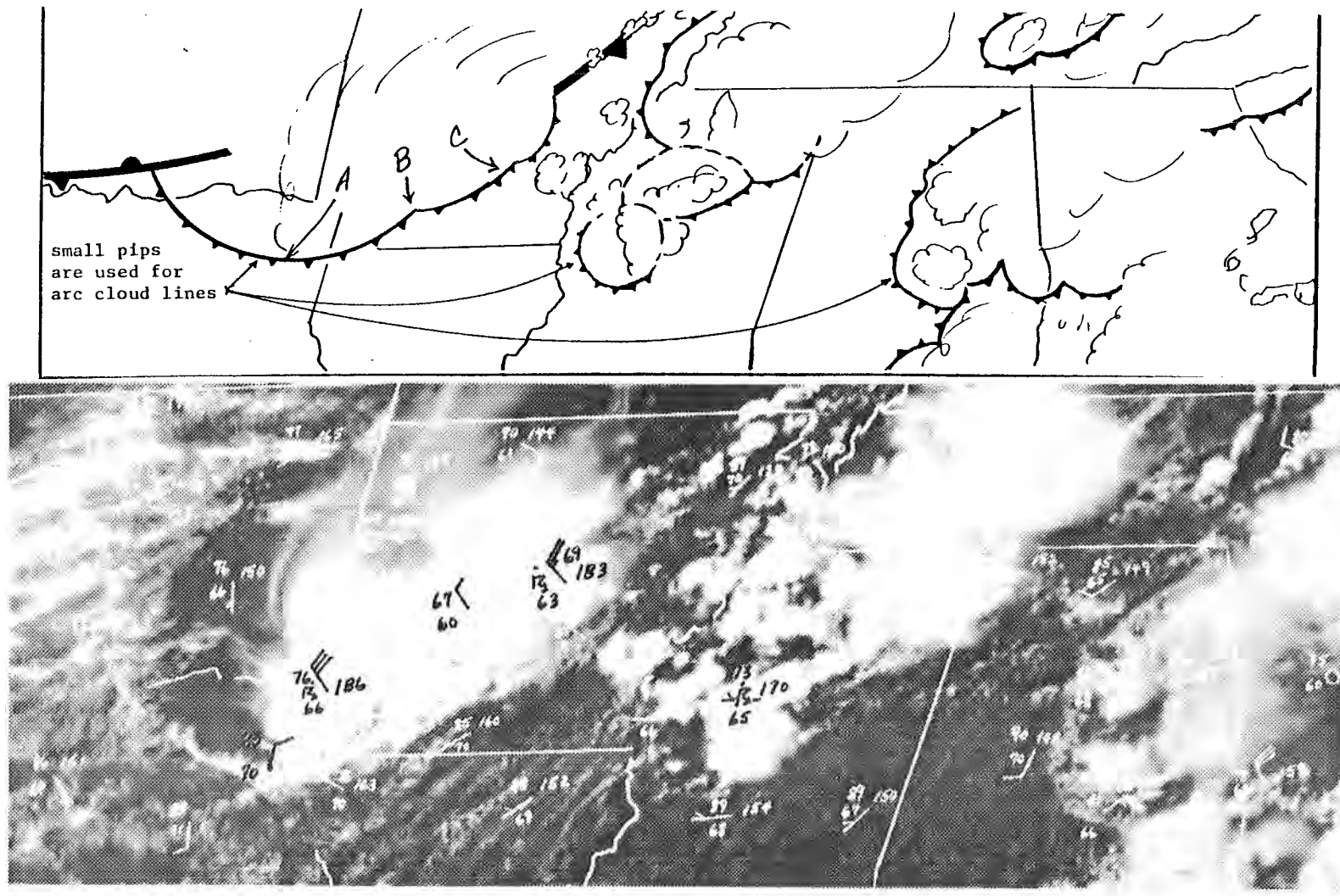
Figure 1.1a.   GOES 1 km VIS 26 May 1975; 1400 CST, and hand analysis of
important features.
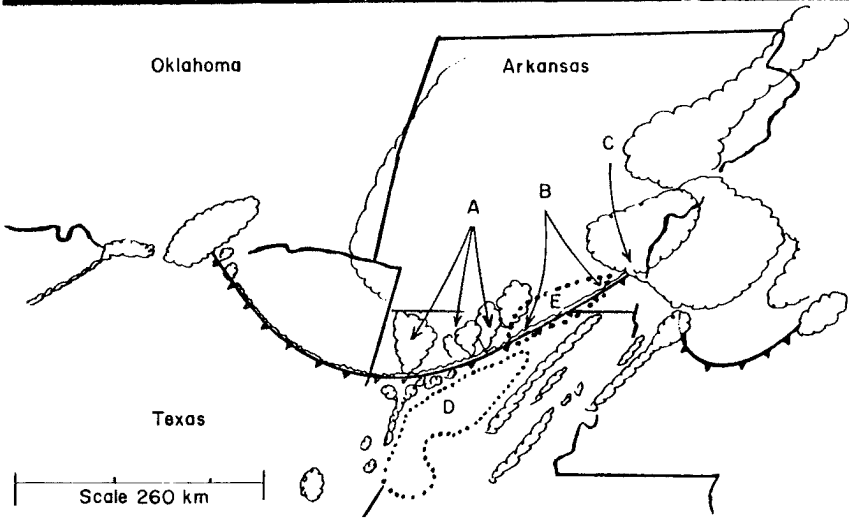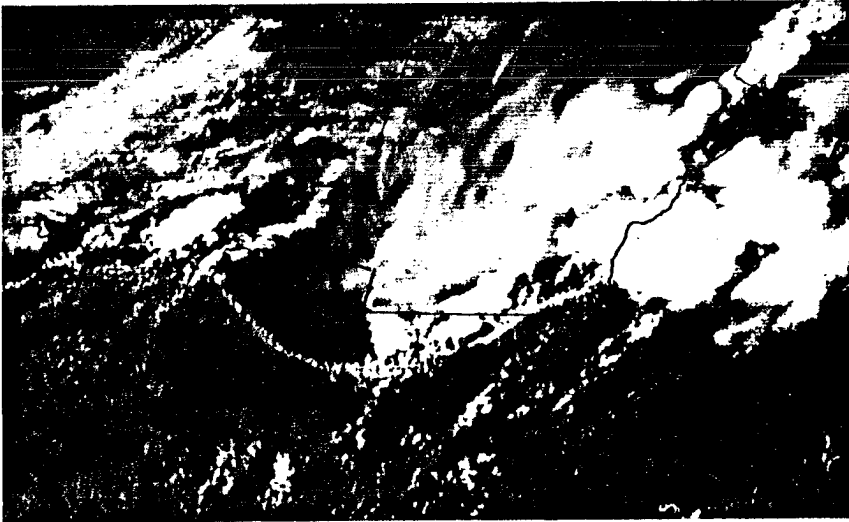
Figure 1.1b. GOES visible image for 26 May 1975 at 1532 CST with a resolution of 1 km, and hand analysis of important features in that image.
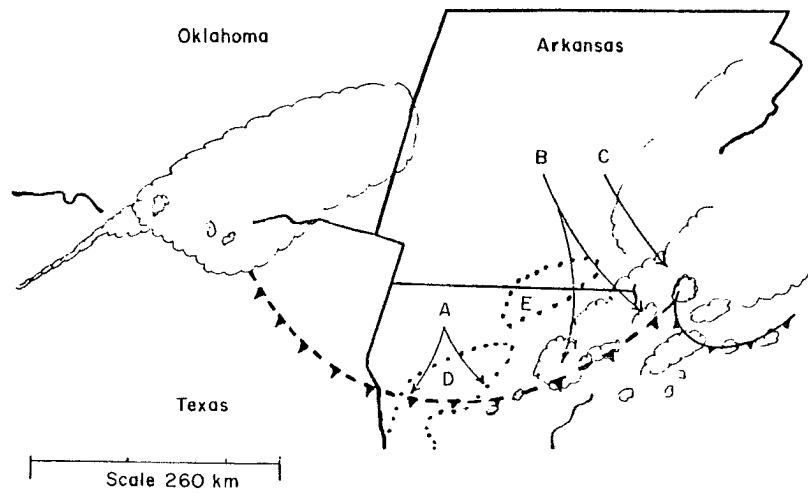
Figure 1.1c. GOES visible image for 26 May 1975 at 1747 CST with a resolution of 1 km, and hand analysis of important features in that image.

play an important role across many scales in meteorology. For example,
convective storms are important contributors to the total energy budget
of the global circulation as well as summertime tropical regions
through their release of latent heat, radiational properties, and
convective cluster scale up moist/down dry vertical circulations they
induce (Gray, 1973; Foltz and Gray, 1979). Locally, the convective
storm lies at the heart of many weather-related events that affect
everyday life. During the spring and summer months, tornadoes, flash
floods, downbursts, hail and lightning pose serious threats to life and
property throughout the United States. Table 1.1 shows some of the
more notorious of those events.

While tornadoes and flash floods receive the most nationwide media
coverage, one of the greatest weather-related killers in the United
States is lightning from the everyday thunderstorm. In fact, from the
period 1959-1983, 378 more people were killed in the United States by
lightning than tornadoes (National Climatic Data Center, Storm Data,
1983). That same "ordinary" thunderstorm can wreak havoc in the
construction industry while at the same time provide much needed water
for agricultural purposes. As was pointed out by Changnon (1978)
thunderstorms are the major source of water for agricultural purposes
throughout the southeast United States. Interestingly enough, while
convective storms are providing moisture to one part of the country,
other portions need summertime precipitation augmentation to improve
water resources for human consumption, for power generation and for
agricultural purposes. For local convective weather events, more
precise very-short-range forecasting [often termed nowcasting
(Browning, 1982)] is badly needed. Before accurate and precise local

Table 1.1

Some Notorious Weather Events Over the U.S.A.
Related to Convective Storms (since 1963)

Type	Date	State(s)	Deaths
Lightning	Dec 8, 1963	Maryland	81
Tornado	Apr 11, 1965	Indiana, Illinois, Ohio Missouri, Wisconsin	271
Flash Flood	Jun 9, 1965	South Dakota	236
Tornado	Apr 3,4, 1974	Alabama, Georgia, Ohio, Tennessee, Kentucky	350
Downburst	Jun 24, 1975	New York	112
Flash Flood	July 31, 1976	Colorado	130
Flash Flood	July 19,20, 1977	Pennsylvania	68
Tornado	Apr 10, 1979	Texas, Oklahoma	60
Downburst	July, 1982	Louisiana	153
Tornado	Mar 28, 1984	South Carolina, North Carolina	57
Tornado	May 31, 1985	Pennsylvania, Ohio Ontario	94
Downburst	Aug 2, 1985	Texas	137

thunderstorm forecasting becomes a reality, an improvement in understanding of convective storm genesis and development is required. This paper addresses how research based on satellite data is helping provide that required understanding.

Understanding the forces that control the development and evolution of deep convection is one of the most important and challenging problems in meteorology today. It remains an elusive problem even though various aspects of it have been vigorously investigated over the past quarter century. It is generally agreed that the development of a convective storm or storm array depends on the interaction of meteorological fields ranging from the synoptic scale cyclone down to the cloud condensation nuclei (Lilly, 1977). However, little is known about why a particular storm forms and develops the way it does, or why a convective array behaves in a particular manner. This is especially true for storms that form under weak synoptic scale forcing. Most of the available information about convective storm development and intensification is focused on either the large scale conditions favorable for convective development (Beebe and Bates, 1955; Miller, 1972), or the individual convective storm (Byers and Braham, 1949; Browning, 1964; Newton, 1966; Fankhauser, 1971, 1976; Brandes, 1978). As was pointed out by Simpson and Dennis (1974), more is known about synoptic scale conditions favorable for convective development and about cloud microphysics than is known about the mesoscale, which remains both poorly measured and poorly understood. That this problem still exists today can be readily verified - better understanding of mesoscale convective phenomena is

one of the cornerstones in the planning of the National STORM Program

(Zipser, 1984):

> "it is on the stormscale (or "mesoscale" to
> meteorologists) that the weather of greatest
> significance is actually experienced. It is
> mesoscale phenomena which must be understood ..."

The lack of information on the interaction between convective

clouds and their local environment has been mainly due to a gap in

meteorological observing capability in the days prior to the high

resolution geostationary satellite (Purdom, 1976). Prior to

satellites, meteorologists were forced to make inferences about the

mesoscale from macroscale (synoptic) patterns. Fujita (1955)

recognized this problem in discussing mesoscale analysis when he

pointed out: "In the short-period forecasting or extrapolation of the

weather on the meso-synoptic scale, the complete data such as used in

this paper are not available on a current basis." However, significant

advances in closing that gap are being made using data available from

geostationary satellites. The geostationary satellite is the only

meteorological observing tool that can simultaneously observe the

evolution of clouds from the synoptic scale down to the cumulus scale.

When satellite information is combined with more conventional data, the

trigger mechanisms that are important in the formation and maintenance

of deep convection may be analyzed and better understood, Purdom

(1979), Maddox (1980). It is from satellite imagery that the

importance of convective scale interaction, manifested through

thunderstorm outflow boundary interaction, became recognized.

It was Purdom (1973) who first pointed out:

> In satellite imagery, the leading edge of the
> meso-high [thunderstorm outflow boundary] appears
> as an arc-shaped line of convective clouds moving

> out from a dissipating thunderstorm area. The arc-
> shaped cloud line is normally composed of cumulus,
> cumulus congestus, or cumulonimbus clouds ... the
> majority of new convective activity will form along
> this boundary.

Later, Purdom (1979) was to introduce the concept of "convective scale interaction" and discuss its role in controlling the development and evolution of deep convection. That interaction, most often observed in satellite imagery, manifests itself as the merger and intersection of arc cloud lines with other convective areas, lines and boundaries. This type interaction has recently been observed by Wilson and Carbone (1984) using Doppler radar data to investigate new thunderstorm generation at the collision of two thunderstorm outflows.

In the chapters that follow, the fundamental importance of convective scale interaction in the development and evolution of deep convection will be investigated. It will be shown how this new knowledge concerning the development and evolution of deep convection has impacted, and will continue to impact, the field of mesoscale meteorology. In chapter 2, the importance of geostationary satellite imagery to mesoscale meteorology will be discussed. In chapter 3, high resolution geostationary satellite imagery, along with conventional meteorological data, will be used to define and illustrate the concept of convective scale interaction. In chapter 4, data will be presented to show that under weak synoptic scale forcing, convective scale interaction is of fundamental importance in controlling the development and evolution of deep convection and its ensuing rainfall. Chapter 5 will address the dynamic and thermodynamic characteristics of arc cloud lines; that chapter relies heavily on information gathered from research aircraft flights specifically designed to study arc cloud

lines. In chapter 6, a physical model will be presented to describe the observed behavior of arc cloud lines and the process of convective scale interaction. In chapter 7, the information from the previous chapters will be summarized along with their implications for a range of problems that deal with convective phenomena.

2.0   SATELLITE DATA AND SATELLITE OBSERVATIONS OF MESOSCALE PHENOMENA

From the earliest days of meteorology, the importance of clouds in

defining the state of the atmosphere has been recognized. As pointed

out in the Handbook of Meteorology section on "Clouds and States of the

Sky" (Schereschewsky, 1945):

> Clouds have been observed and used for short-
> period weather forecasting from time immemorial...
> Clouds are now considered essential and accurate
> tools for weather forecasting. Every measure of
> the air masses (discontinuity, subsidence,
> instability and stability, etc.) is reflected by
> the shape, amount, and structure of the clouds.
> Thus close scrutiny of clouds will assist the
> analyst in identifying and analyzing air masses.

From the inception of the meteorological satellite program,

the importance of cloud imagery was recognized. According to

Kellogg (1982):

> The idea that satellites could be used as
> weather reconnaissance vehicles seemed fairly
> obvious... What we needed was evidence that
> observations from a satellite would be useful in
> meteorology.

> Delbert Crowson (Crowson, 1949) ... showed for
> the first time a photograph taken looking down on
> clouds from a rocket, and he included a short
> analysis.

> Joc Bjerknes had great enthusiasm for the idea
> of doing a detailed analysis of rocket pictures ...
> Bjerknes wrote "...it may be said that the rocket
> pictures add a considerable amount of interesting
> information to the ordinary weather map analysis
> and, in addition, that the accumulated knowledge
> from the maps help us in the new problem of
> interpreting what we see from high-level rocket
> pictures. It may be added that although in the
> present report the ordinary surface and upper wind
> maps had to be used to a great extent to arrive at

> the total picture, accumulated experience from
> several analyses from joint rocket and conventional
> methods would make it possible to arrive at the
> right analysis by rocket pictures only."

With the launch of TIROS-I on April 1, 1960 cloud imagery from

space became available. Since that time routine global cloud

observations from polar orbiting satellites have helped advance

meteorological understanding of synoptic scale phenomena. In a similar

fashion, routine local scale observations from high resolution

geostationary satellites are helping advance our understanding of

mesoscale phenomena.

2.1. Geostationary Satellite Observations of Mesoscale Phenomena

Prior to the high resolution geostationary satellite, there

existed a lack of routine observational information on the mesoscale

evolution of deep convective clouds and their local environment. The

mesoscale was a "data sparse" region. Over the 48 contiguous

continental United States, approximately 1000 hourly surface observing

sites and 126 upper air sounding sites cover an area of approximately

8×10^6 sq km, forcing meteorologists to make inferences about

mesoscale phenomena from macroscale observation. With GOES imagery,

meteorological phenomena that are infrequently detected at fixed

observing sites are routinely observed: a "reporting station" exists

every 1 km using the information implicit in the visible data, and

every 8 km with that in the infrared data. This may be readily

verified by inspecting figure 1.1 which shows satellite imagery and

corresponding surface data plots.

Figure 1.1 illustrates one important class of mesoscale convective

phenomena, the arc cloud line, which is routinely observed using

satellite imagery (to be discussed in detail in the following chapters). Other mesoscale phenomena that are routinely observed in satellite imagery are squall line development (well known) and thunderstorm development due to early morning cloud cover effects (not well known). Examples of those phenomena are shown in figure 2.1 and figure 2.2.

Purdom (1973b), Purdom and Gurka (1974), and Weiss and Purdom (1974) were the first to discuss the effects of early morning cloud cover on afternoon thunderstorm development. They likened the situation to that of a land-sea breeze regime, with the circulation and resulting vertical motions that develop being due to differential heating between adjacent cloudy and clear regions. Figure 2.1 is a good example of that phenomenon. It is interesting to note that, similar to the arc cloud line phenomena first introduced by Purdom (1973), effects of early morning cloud cover on afternoon thunderstorm development are now beginning to be investigated using mesoscale numerical models (Segal, et al, 1986).

Generally, organized convergence lines that might trigger strong convection, such as some fronts, pre-frontal squall lines or dry lines, can be detected in satellite imagery prior to deep convection developing on them and their being detected by radar (Purdom 1971, 1982). An example of a frontal system that develops into a severe squall line is shown in figure 2.2. Early squall line development of this type is routinely detected in GOES imagery prior to deep convective development along them and their being detected by radar. Near the time of the image in figure 2.2b, large hail and funnel clouds were reported in eastern South Dakota, a tornado injured six people in
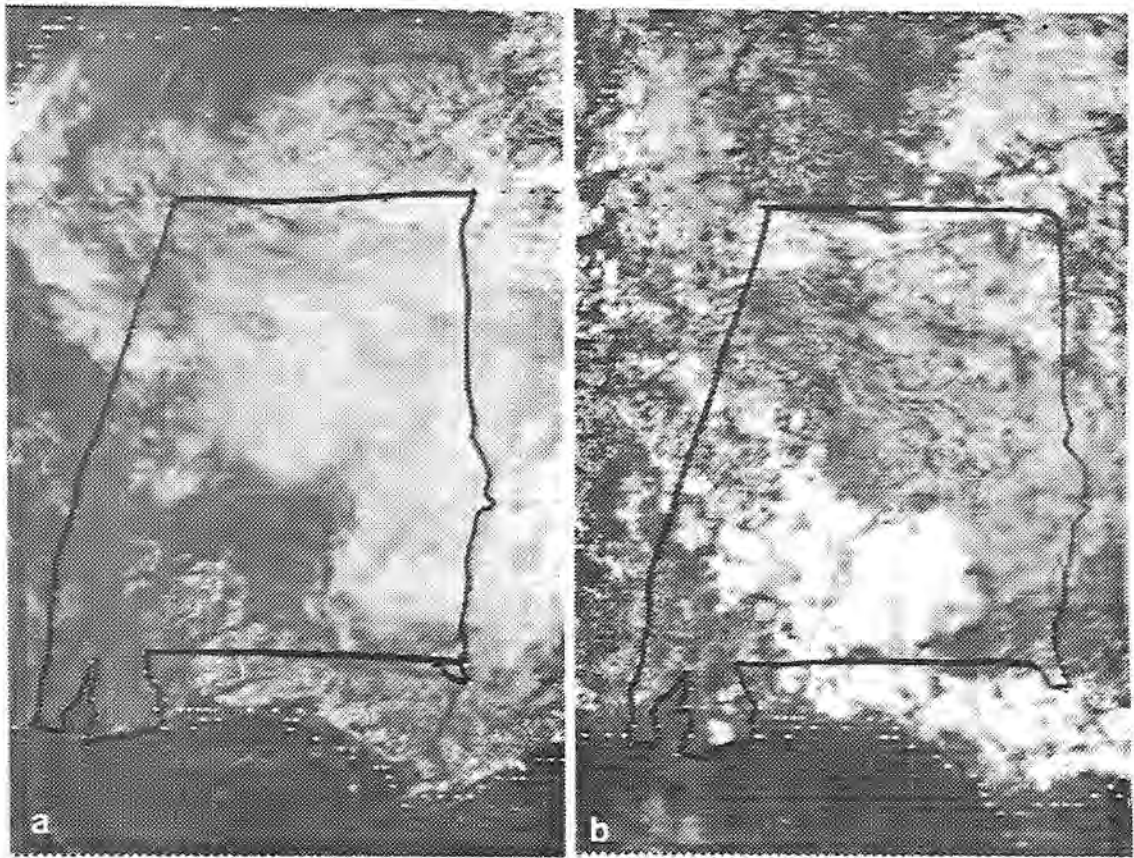
Figure 2.1. GOES visible images for 27 May 1977 for (a) 1130 and (b) 1330 CST. This pair of images shows the dramatic effect early cloud cover can have on afternoon thunderstorm development. Note that the early clear region in southwest Alabama becomes filled with strong convection during the day, while the early cloudy region over the remainder of the state evolves into mostly clear skies.
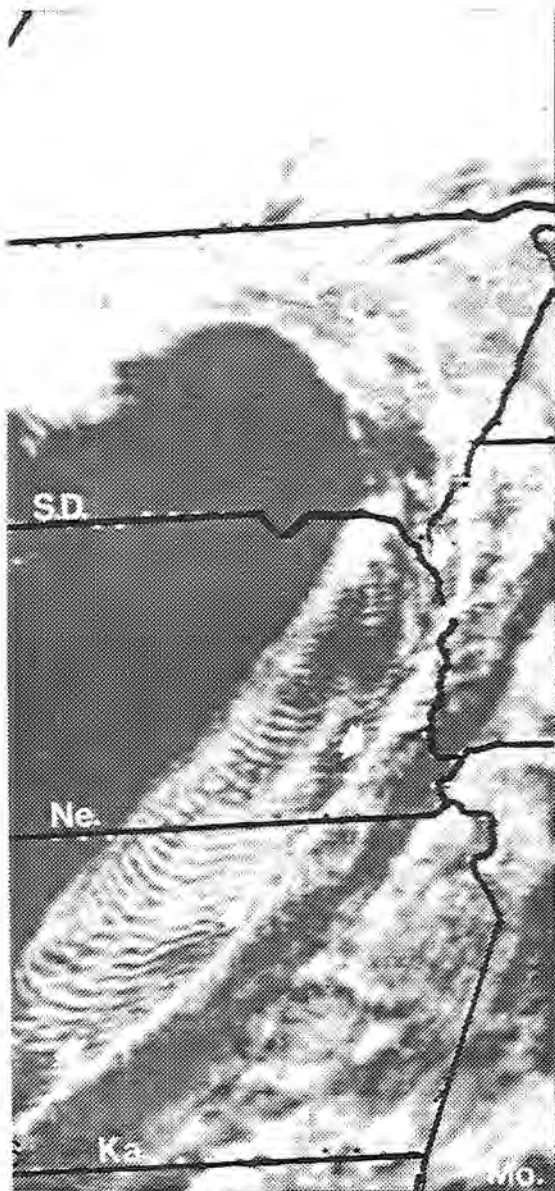
Figure 2.2a. GOES visible images
for 14 June 1976 for 1300 and
1400 CST with a resolution of 1 km.
These images show a narrow frontal
zone, extending from central Kansas
into eastern Nebraska and South
Dakota, prior to the development
of severe convection along it.
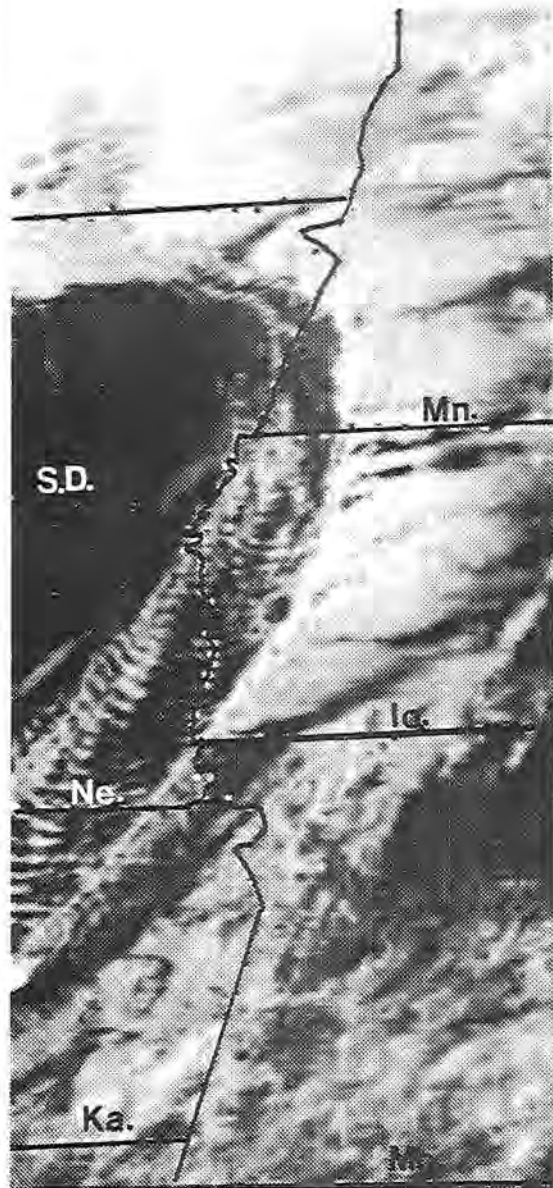
Figure 2.2b. GOES visible
image for 14 June 1976 at 1700
CST with a resolution of 1 km.
This image shows the severe
convection that has developed
along the front as it pushed
into Minnesota and Iowa.

Minnesota, and a tornado was reported in Iowa. Later in the evening, six people were injured and one was killed by tornado activity in Minnesota, severe winds were reported in Iowa, and the developing thunderstorms in Central Kansas produced numerous funnel reports, one confirmed tornado and several reports of hail.

Figure 2.2b illustrates why an atmosphere under strong synoptic scale forcing is not well suited for satellite image based investigations of the arc cloud line phenomena. Since squall line situations are often associated with strong dynamics and vertical wind shear, the thunderstorm's anvil often spreads out in the direction of motion of the storm, masking the thunderstorm outflow arc cloud line. In some instances, arc cloud lines are detectable in severe storm situations, however, this is more the exception than the rule.

The clouds and cloud patterns in a satellite image may be thought of as a visualization of mesoscale meteorological processes. When that imagery is viewed in animation, the movement, orientation and development of important mesoscale features can be observed, adding a new dimension to mesoscale analysis. Furthermore, animated GOES imagery provides observations of convective behavior at temporal and spatial resolutions compatible with the scale of the mechanisms responsible for triggering deep and intense convective storms. It was only after high resolution geostationary satellite imagery became available that arc cloud lines and their importance in subsequent thunderstorm development was realized (Purdom, 1979).

2.2. Geostationary Satellite Data

Normally, there are five geostationary satellites in orbit around the globe, all of which provide routine meteorological observations.

They are: (a) METEOSAT (Europe) at the 0° meridian; (b) GMS (Japan) at 130° East; (c) INSAT (India) at 80°E; (d) GOES-VAS East (United States) at 75°W; (e) GOES-VAS West (United States) at 135°W.

The heart of the GOES satellite is its Visible and Infrared Spin Scan Radiometer (VISSR) which on a nominal half hourly basis observes the full earth disk in the infrared portion of the spectrum (10.5 - 12.5 μm) at 7 km resolution both day and night and in the visible portion of the spectrum at 1 km resolution during day time. For the current GOES satellites, the VISSR's capabilities have been expanded so that it can act as an Atmospheric Sounder: thus the acronym GOES-VAS. The VAS instrument measures outgoing radiation from the earth-atmosphere system in 12 spectral regions (in addition to visible) with a horizontal resolution of either 7 km or 14 km, depending on the wavelength being observed. Specific information about each of the 12 channels is given in table 2.1. The majority of the satellite imagery to be used in the sections that follow are from the GOES visible channel and the 11.2 μm infrared window channel (channel 8).

The earth-atmosphere system's radiance to space varies with wave length because absorption bands cause abrupt changes in atmospheric transmission at different wave lengths. Figures 2.3a and 2.3b show characteristics of atmospheric transmission in the portions of the spectrum surrounding the region sensed by the GOES visible detector as well as the channel 8 infrared detector. Note that both those regions suffer very little contamination. Planck's law is given by:

$$B_\lambda = \frac{C_1 \lambda^{-5}}{e^{C_2/\lambda T} - 1} \quad (Wcm^{-2} \; \mu m^{-1} \; sr^{-1}) \qquad (2.0)$$

Table 2.1 VAS Instrument Characteristics

VAS Instrument Characteristics

Weighting Function

Spectral Channel	Central Wavelength (μm)	Absorbing Constituent	Peak Level (mb)	Representative Thickness (mb)	Surface or Cloud Emission Effect
1	14.7	CO_2	40	150-10	usually none
2	14.5	CO_2	70	200-30	nothing below 500 mb
3	14.5	CO_2	300	500-10	nothing below 800 mb
4	14.0	CO_2	450	800-300	weak
5	13.3	CO_2	950	SFC-500	moderate
6	4.5	CO_2	850	SFC-500	moderate
7	12.7	H_2O	surface	SFC-700	strong
8	11.2	window	surface	---	strong
9	7.2	H_2O	600	800-400	weak at sfc
10	6.7	H_2O	450	700-250	nothing at sfc
11	4.4	CO_2	500	800-100	weak
12	3.9	window	surface	---	strong
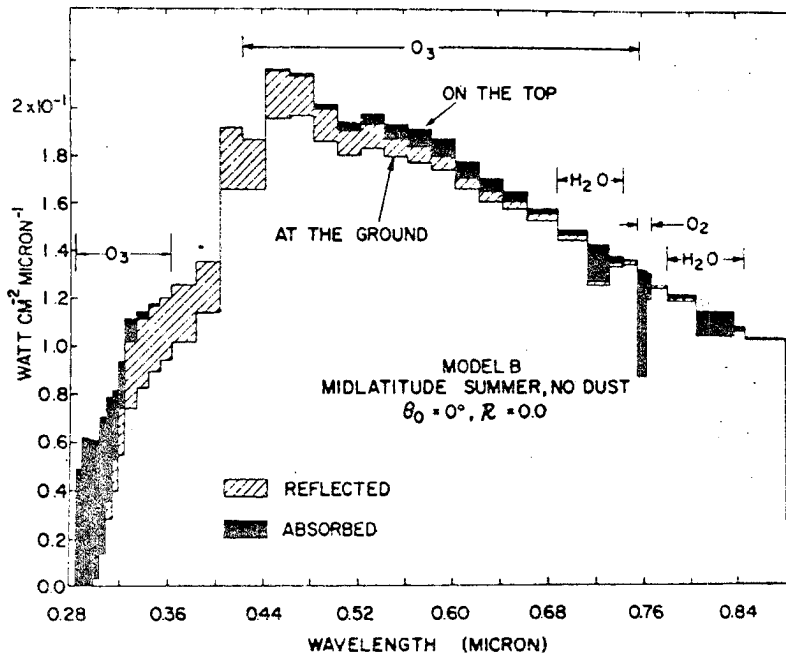
Figure 2.3a. Atmospheric transmission in the visible portion of the spectrum. From Paltridge and Platt, 1976.
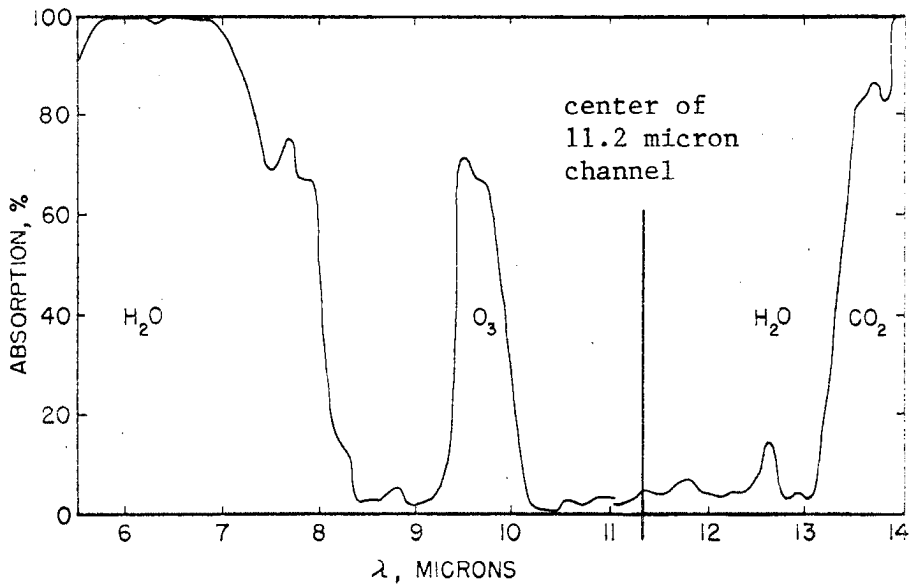
Figure 2.3b. Absorption by the atmosphere between 5.5 and 14μ (after Hess, 1959). There were 2.1 mm of precipitable water present for the observations below 11μ and 1.3 mm above 11μ.

where B_λ is the emitted radiance, C_1 and C_2 are constants, λ is the wavelength of the radiance and T is the temperature of the scene. Figure 2.4 is a plot of B_λ scaled by temperature versus wavelength for 5800°K (visible), and 220°K (comparable to infrared cloud top temperatures for intense thunderstorms) and 300°K. The spectral widths of the GOES visible channel and infrared channel 8 are superimposed. Differentiation of 2.0 with respect to wave length and solving for λ_{max} as a function of temperature yields Wien's law,

$$T \, \lambda_{max} = 2897.8 \, (\mu m \, °K), \qquad (2.1)$$

which indicates that both the visible channel and IR window channel on GOES take good advantage of the energy available in their respective wave lengths. This fact can be seen by inspecting figure 2.4. Thus, the GOES visible detector receives energy leaving the earth-atmosphere system due to reflected sunlight, which depends on the characteristics of the reflecting surface. The GOES channel 8 infrared detectors receive energy leaving the earth-atmosphere system in the "window" region due to radiation emitted by the surface of the earth and clouds, with a small amount of water vapor attenuation. Thus, information from that channel is useful for inferring cloud height and thunderstorm intensity. A more detailed discussion of the suitability of this channel's information for monitoring thunderstorm intensity may be found in a report by Purdom and Vonder Haar (1983).
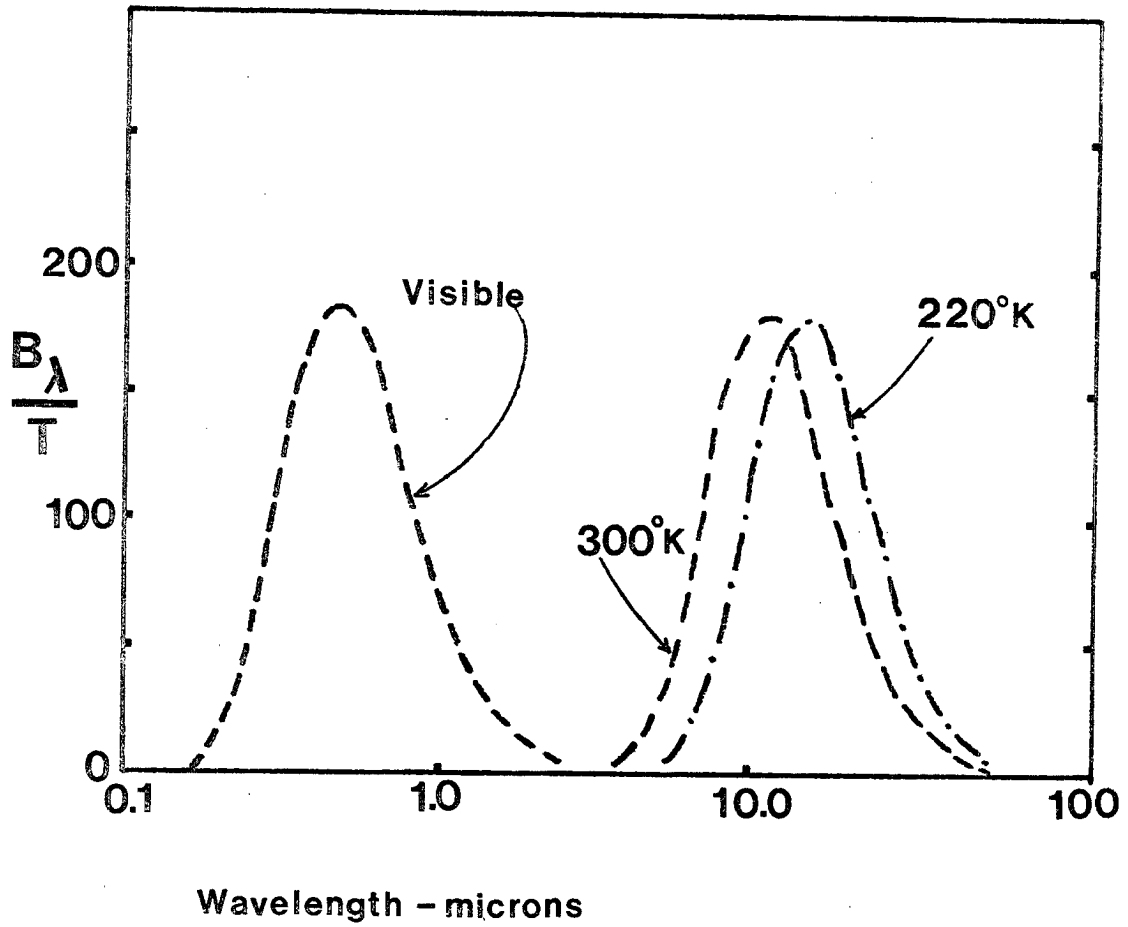
Figure 2.4. B_λ scaled by temperature versus wavelength for 5800°K (visible) and 220°K (infrared).

3.0 SATELLITE OBSERVATIONS OF THE ARC CLOUD LINE PHENOMENA
AND CONVECTIVE SCALE INTERACTION

High resolution GOES imagery has made available for the first time observations of convective development at spatial and temporal resolutions compatible with the scales of the mechanisms responsible for the triggering of deep and intense convective storms. Movies made from these data (Bohan, 1981) show that convective scale interaction (Purdom, 1979) is of primary importance in determining the development and evolution of deep convection. This interaction manifests itself as the merger and intersection of convection produced outflow boundaries with other convective areas, lines and boundaries. This process is fundamental in the evolution and maintenance of deep convection; it is complex because of the continuously evolving nature of a convective environment. Until recently (Wilson and Carbone, 1984), convective scale interaction had only been observed using satellite imagery.

The original convective storm or storms which produce an outflow boundary may or may not be the result of earlier convective scale interaction. There are a large number of other local forcing mechanisms that may be responsible for triggering convective storms which subsequently produce outflow boundaries. Among these local forcing mechanisms are: a) frontal zones; b) land-sea breeze fronts; c) early cloud cover induced convergence zones (figure 2.1); d) squall lines (figure 2.2); e) mesoscale convective complexes; and f) other differential heating related mechanisms such as river breezes and wet

versus dry ground areas. However, as will be shown in Chapter 4, under conditions of weak synoptic forcing convective scale interaction is the dominant storm generation mechanism that is active late in the day.

3.1. Satellite Observations of Outflow Boundaries

Convective scale interaction is directly associated with outflow boundaries produced by precipitating convective storms. Purdom (1973) showed that in satellite imagery the leading edge of a thunderstorm's outflow boundary appeared as an arc shaped line of convective clouds moving out from a dissipating thunderstorm area. The arc shaped cloud line is normally composed of cumulus, cumulus congestus, or cumulonimbus clouds. He also pointed out that the arc cloud line was often not detectable by operational noncoherent radar. This point has recently been corroborated by Wilson and Carbone (1984). Later, Purdom (1973) showed that the intersection of an arc cloud line with another boundary located a point with a high potential for intense convection, and under favorable conditions, severe weather. This type storm is seen in southeast Oklahoma in figure 1.1c. Figure 1.1a (shown again as figure 3.1a) shows the characteristic appearance of arc cloud lines in satellite imagery along with a mesoscale analysis/nephanalysis in which the arc cloud lines in figure 3.1 were analyzed with the aid of 15 minute interval satellite images. While Purdom (1979) was the first to recognize the prevalence and importance of such boundaries as shown in satellite imagery, a number of authors have studied the thunderstorm outflow phenomena. Their works may be broken into four broad categories: a) observational; b) laboratory; c) atmospheric probes, and; d) numerical models. Rather than provide a detailed description of those works in this section, table 3.1 is given to recognize
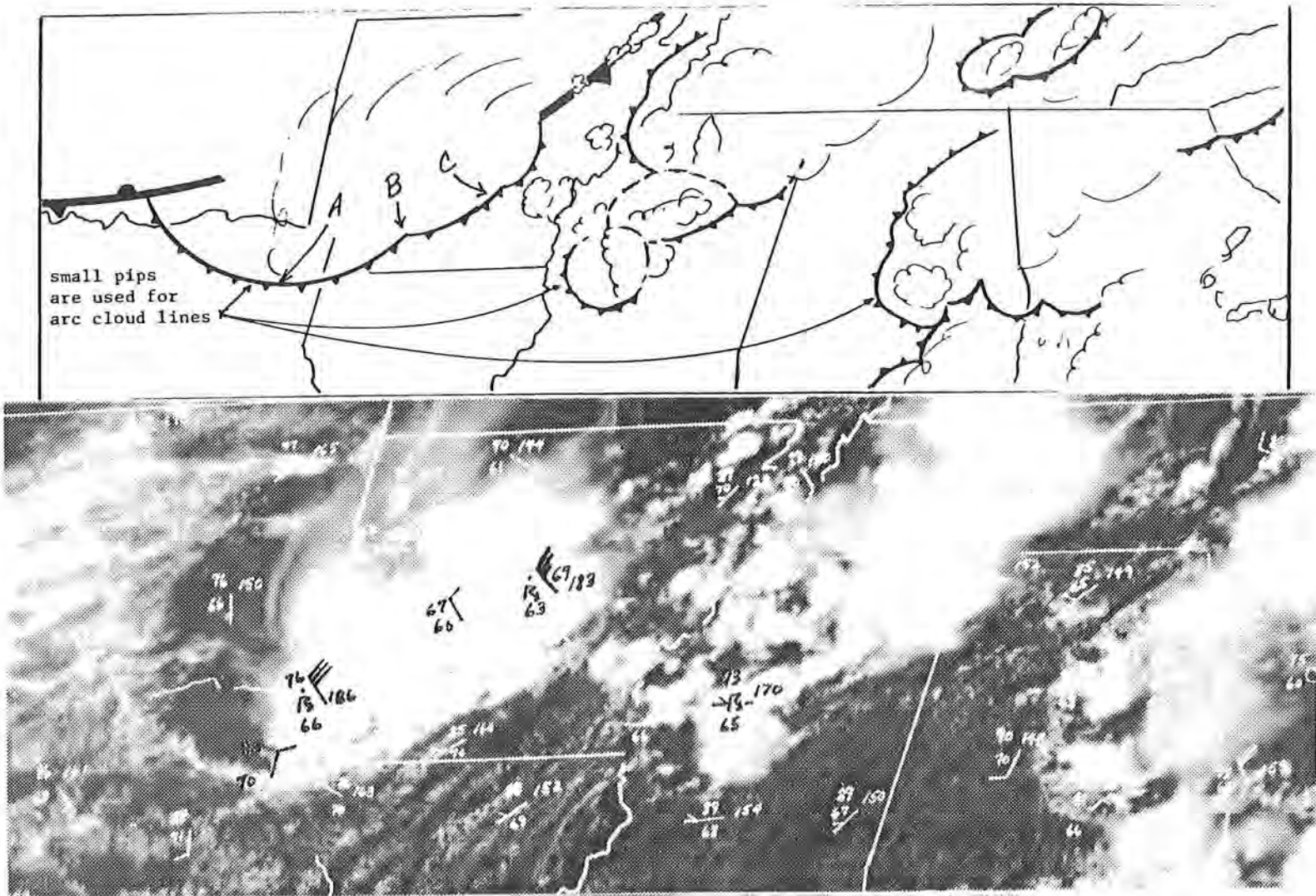
Figure 3.1a. GOES 1 km visible imagery for 26 May 1975 at 1400 CST, and hand analysis of important features in that image.
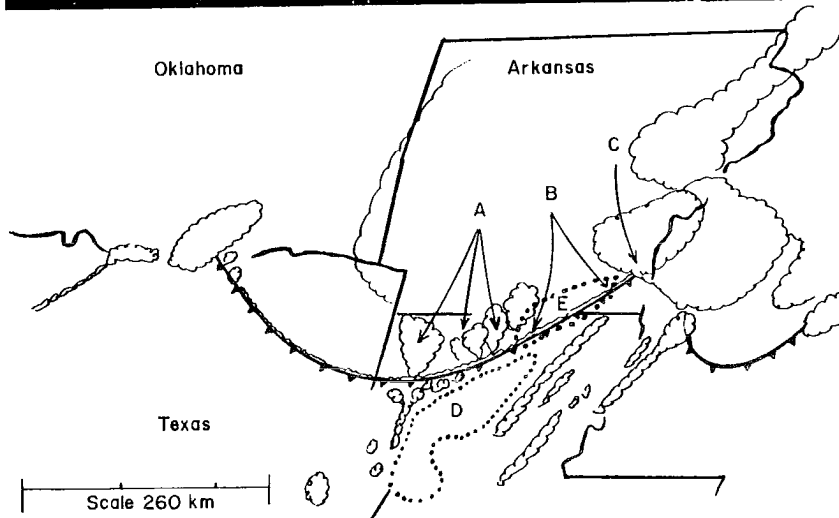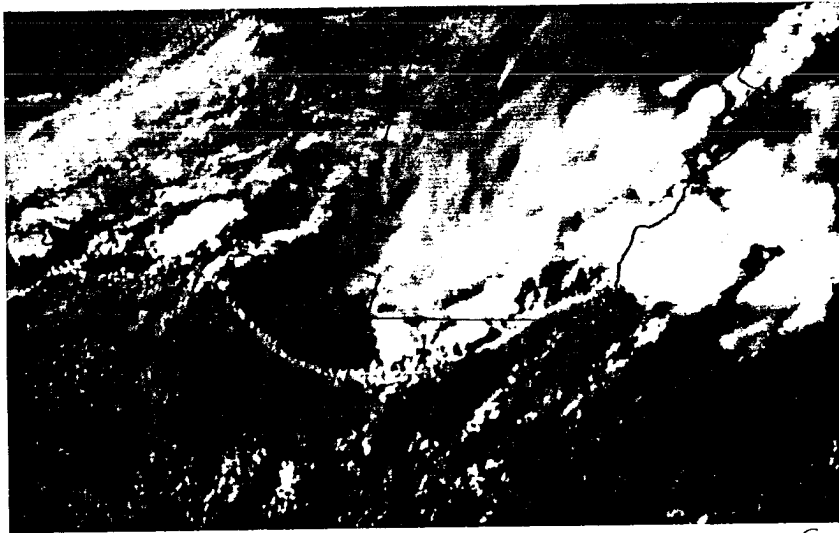
Figure 3.1b. GOES visible image for 26 May 1975 at 1532 CST with a resolution of 1 km, and hand drawing of important features in that image.
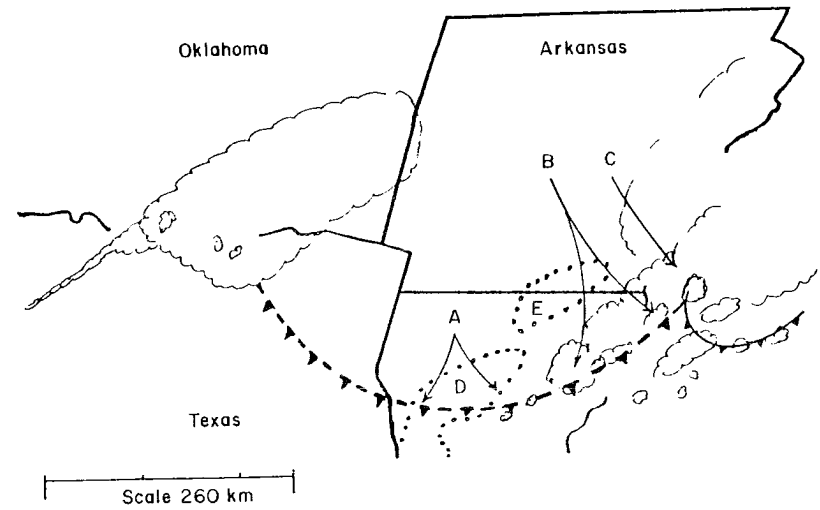
Figure 3.1c. GOES visible image for 26 May 1975 at 1747 CST with a resolution of 1 km, and hand drawing of important features in that image.

Table 3.1

Selected Works Relating to Outflow

Observational

a. Espy (1841): early recorded observations
b. Humphreys (1914): related evaporation to downdraft production
c. Byers & Braham (1949): Thunderstorm Project
d. Fujita (1955): mesoanalysis and mesohigh
e. Fujita (1959): quantify mesohigh production
f. Purdom (1973): satellite observations of arc cloud lines
g. Purdom (1979): convective scale interaction (csi) through arc lines
h. Holle and Maier (1980): document csi using FACE data
i. Weaver and Nelson (1982): csi in supercell tornado production
j. Wilson and Carbone (1984): Doppler radar documentation of csi

Laboratory Measurements

a. Keulegan (1958)
b. Middleton (1966)
c. Simpson (1969)

Atmospheric Probes

a. Byers & Braham (1949): Thunderstorm Project
b. Charba (1974): Oklahoma City, WKY-TV Tower
c. Goff (1976): Oklahoma City, WKY-TV Tower
d. Wakimoto (1982): Project NIMROD
e. Sinclair and Purdom (1981): Aircraft penetrations

Numerical Models

a. Mitchell and Hovermale (1977): severe storm gust front
b. Klemp and Wilhelmson (1978): cloud development along outflow
c. Seitter (1983): arc cloud and thunderstorm gust front motion
d. Droegemeier and Wilhelmson (1983): intersecting outflows

selected of the more important of those works that relate to this paper.

Certain of the earlier observational works are of particular interest when relating conventional observations to satellite observations of arc cloud lines. Among the earliest to address the outflow phenomena was Espy (1841), when he spoke of the outflowing cool winds from storms at the times being observed at a considerable distance from the storm. Later Humphreys (1941) pointed out the importance of evaporation of raindrops in the production of the storm's downdraft and the subsequent cold outflow. Fujita (1959) showed that the cold air production within an outflow's cold dome was caused by evaporation of raindrops from the parent storm or storm system. He further showed, that for different regions of the United States, there was a direct relationship between the amount of surface rainfall and excess mass of a cold dome. In addressing the storm outflow phenomena, the Thunderstorm Project (Byers & Braham, 1949) noted that the storm's cold air outflow could cover an area larger than the storm, as in figure 3.1. This is because an outflow region represents the integrated effect of cold air production by a thunderstorm (or storm system). As the arc cloud line begins to move away from its parent storm, it may cut off the source of unstable air for the storm which leads to the ultimate demise of both the storm and its arc cloud line. However, it is more often the case that unstable environmental air continues to interact with the arc cloud line's parent storm by flowing over and across the top of the outflow cold dome, thus feeding the storm's updraft from above the outflow boundary. The parent storm may also continue to feed on unstable environmental air from its back side

as the arc cloud line moves away from its forward flank. Thus, the excess mass required to feed a storm's updraft and balance the cold dome's outflow mass may continue to be provided by a storm's environment as the outflow arc expands in size.

Fujita (1955) showed that at the boundary of the mesosystem associated with the thunderstorm outflow was a pressure surge line which had characteristics similar to a mesoscale cold front, figure 3.2. This corresponds to satellite observations of arc cloud lines similar to those shown in figure 3.1, and throughout this paper. In figure 3.1 note the windshifts, pressure rises and temperature drops associated with the various arc cloud lines. Figure 3.3, from Fujita (1959), illustrates another important feature of the mesohigh: a change in the vertical temperature and moisture distribution within the cold dome produced by subsidence. This subsidence is due to the greater hydrostatic pressure within the cold dome, which causes it to sink and spread outward in an attempt to reach equilibrium with its surrounding environment. This sinking often leads to a clearing within the cold dome – such clearing is one of the major defining character-istics of arc cloud lines as they appear in satellite imagery. Figure 3.4 is an excellent example of this phenomena.

Figure 3.5 is another example of an arc cloud line as detected in GOES imagery. In this example, the interaction of the arc cloud line with the sea breeze front produced a large thunderstorm in Texas (Zehr, 1982). The arc cloud lines in figure 3.5 were not detected by the network radar located at Hondo, Texas. Arc cloud lines are a natural part of the convective development and evolution process. As will be seen in chapter 4, they are the controlling mechanism for the majority
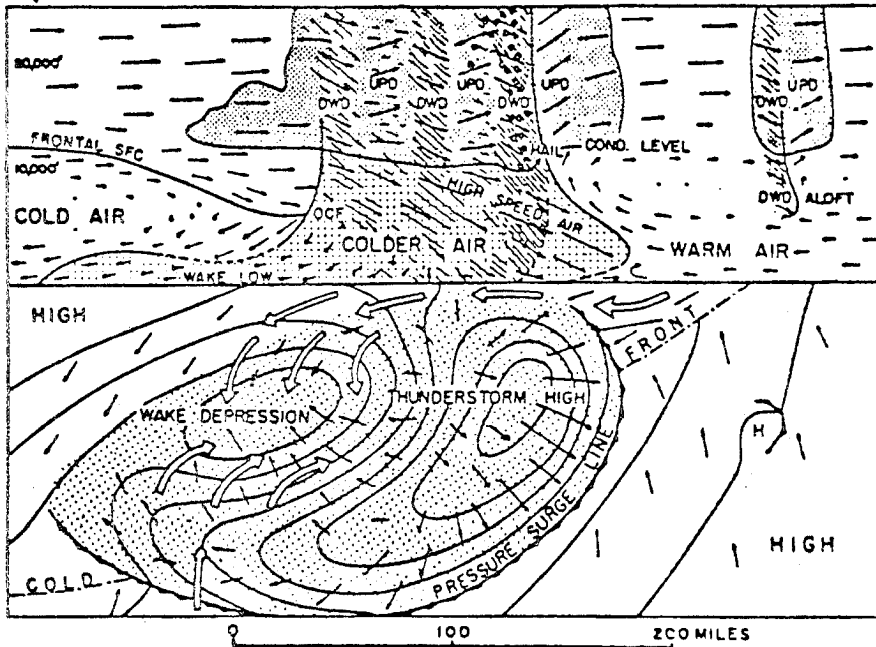
Figure 3.2. From Fujita (1955) illustrating the importance of rain-cooled air in the production of the mesoscale high pressure system.
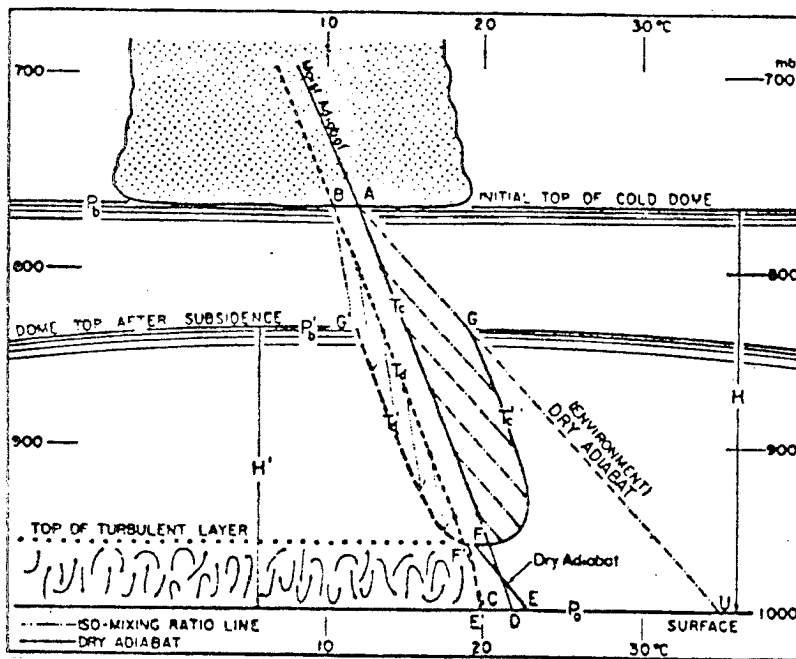
Figure 3.3. From Fujita (1959) illustrating the importance of subsidence within the cold dome, after the passage of the thunderstorm system, which leads to clearing in that region.
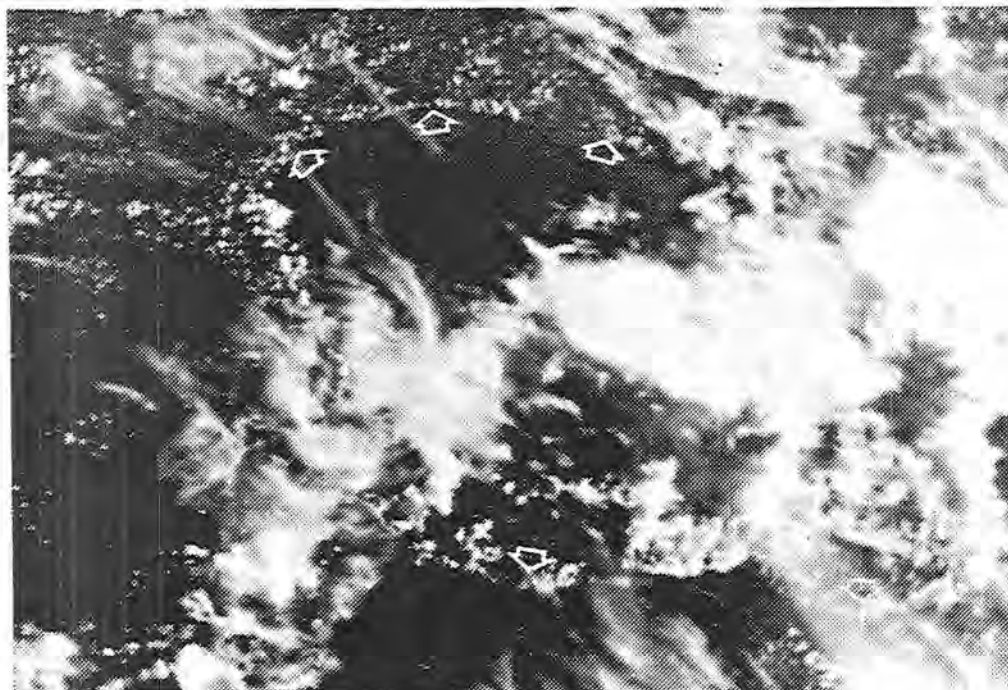
Figure 3.4. Photograph taken from a manned spacecraft of thunderstorm activity and resultant clearing within the cold dome.
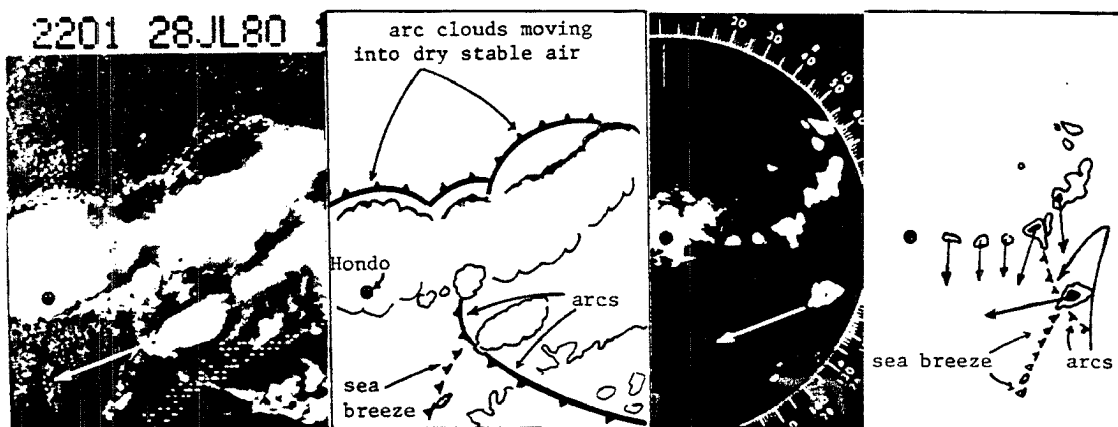
Figure 3.5. Three panel figure showing GOES-East visible image for 1520 CST, 30 July 1980 (left), an analysis of the image (middle) and radar echo movements centered on 1600 CST (right). The large thunderstorm generated at the sea breeze and arc cloud line merger propagated (continuously regenerated) along the moving intersection of those two boundaries.

of the rainfall that occurs over the southeast United States in
summertime.

Arc cloud lines occur throughout the world and are often
associated with intense local weather such as tornadoes (Purdom, 1976;
Parker & Hickey, 1981) and downburst (Caracena et al., 1982). Figures
3.6, 3.7, 3.8 and 3.9 are examples of arc cloud lines interacting with
intense thunderstorms that become tornadic in nature after that
interaction. Figures 3.10 and 3.11 are examples of arc cloud lines
over various other regions of the world.

3.2. Satellite Observations of Convective Scale Interaction

As was pointed out in the previous sections, satellite imagery has
greatly enhanced mesoscale meteorologist's ability to analyze the
development and evolution of deep convection - particularly in an
atmosphere with weak synoptic scale forcing. This is because with
satellite imagery meteorologists are able to observe convective
behavior on a temporal and spatial scale compatible with those of the
mechanisms responsible for the triggering, development and evolution of
deep convective storms.

The Thunderstorm Project (Byers & Braham, 1949) recognized that
many "air mass" thunderstorms formed in preferred regions of low level
convergence and ascent. In such regions, convective cells were often
observed to develop, with an aggregate of cells making up a
thunderstorm, figure 3.12. However, little was known about why a storm
would form at a particular location or behave in a given manner. In
fact, the myth that "air mass" thunderstorms behave in a random fashion
continued until routine observations from geostationary satellites
became available.
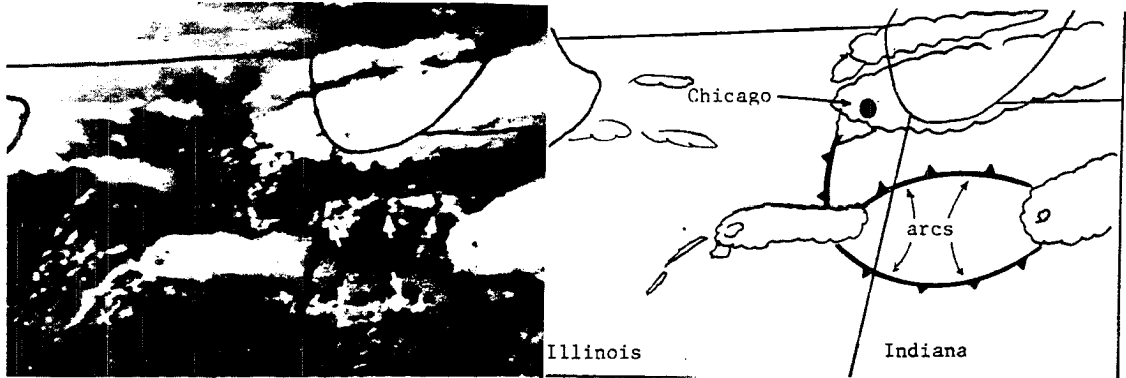
Figure 3.6. GOES-East 1 km visible image at 1645 CST of the arc cloud line associated with Chicago tornadoes of 13 June 1976.
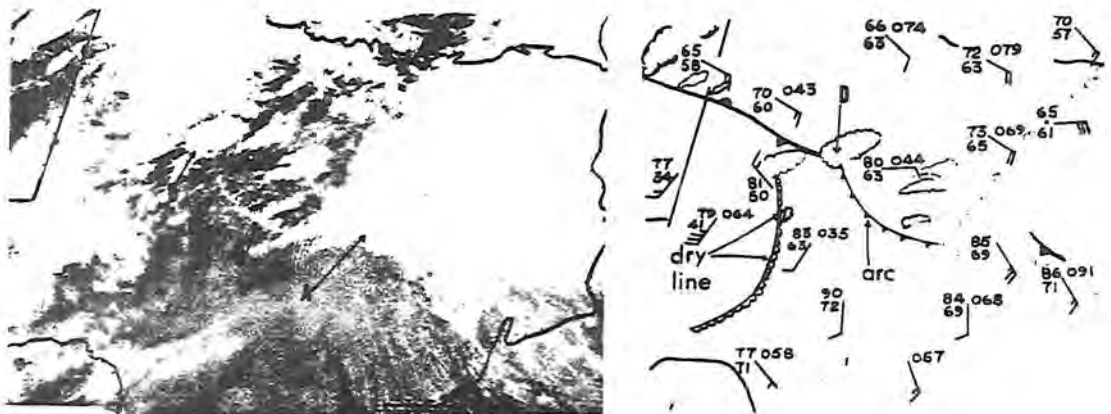
Figure 3.7. GOES-East 1 km visible image at 1345 CST on 25 May 1976: note the arc cloud line interacting with the thunderstorm (tornadic) near Abileen.
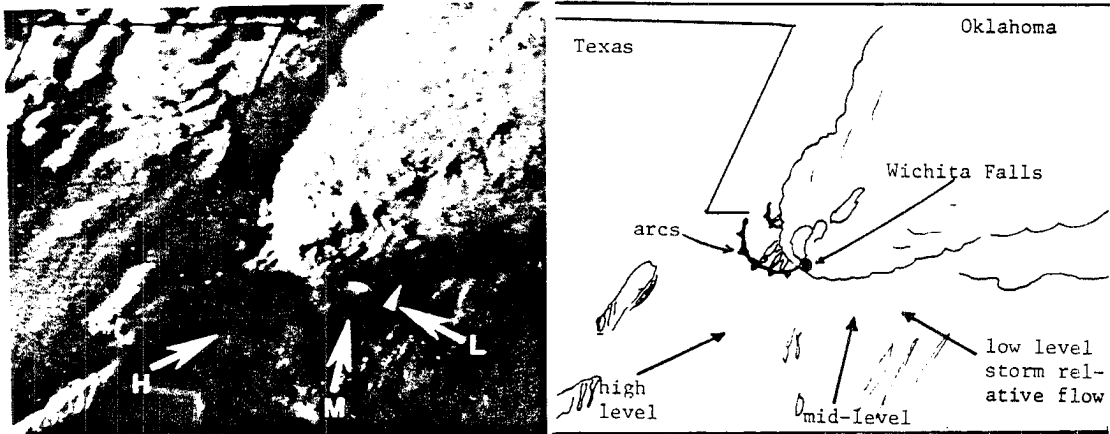
Figure 3.8. GOES-East 1 km visible image on 10 April 1979 at
1815 CST, the day of the Wichita Falls tornado.
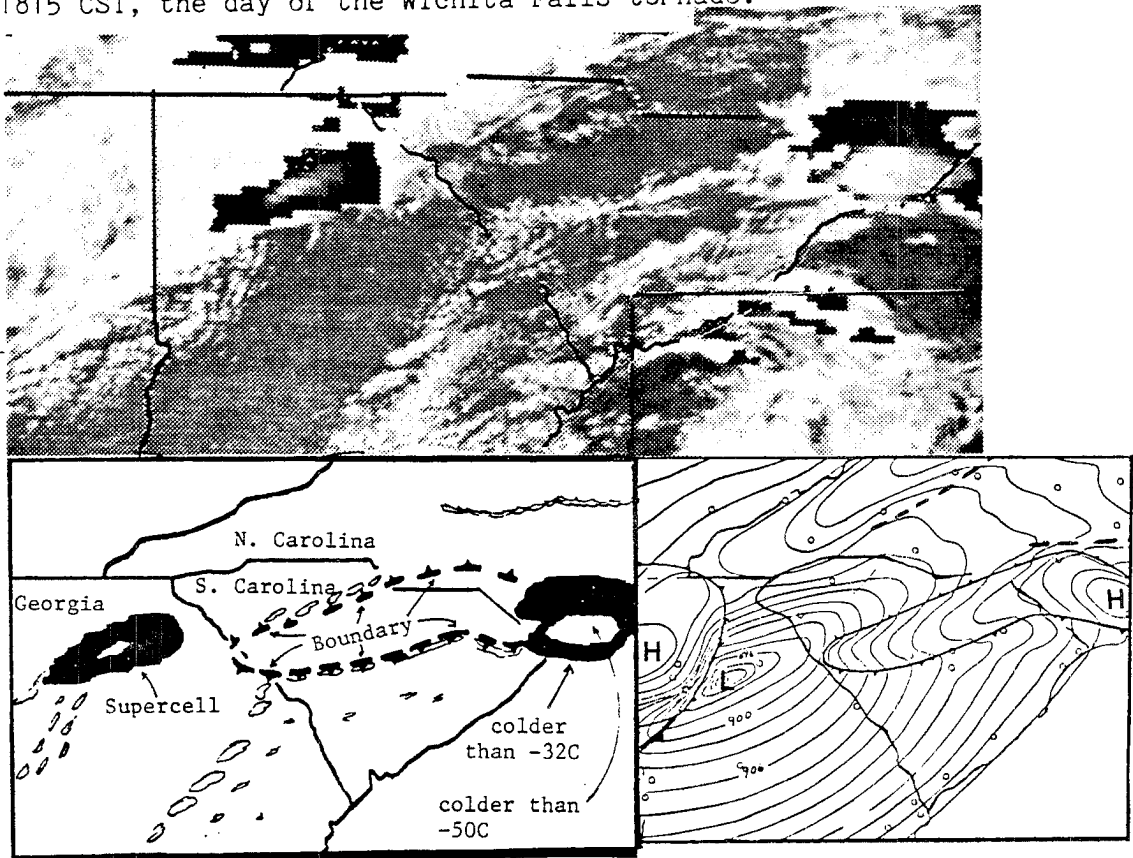
Figure 3.9. GOES-East 1 km visible image on 28 March 1984 at 1430 CST:
note the arc cloud line boundary. The supercell located in Georgia
produced continuous long track tornado activity after interacting with
the arc cloud line boundary. The analysis on the right is based on
conventional surface observations.

Figure 3.10.   DMSP image of arc cloud lines over South America at 1430 GMT on 24 September 1985.
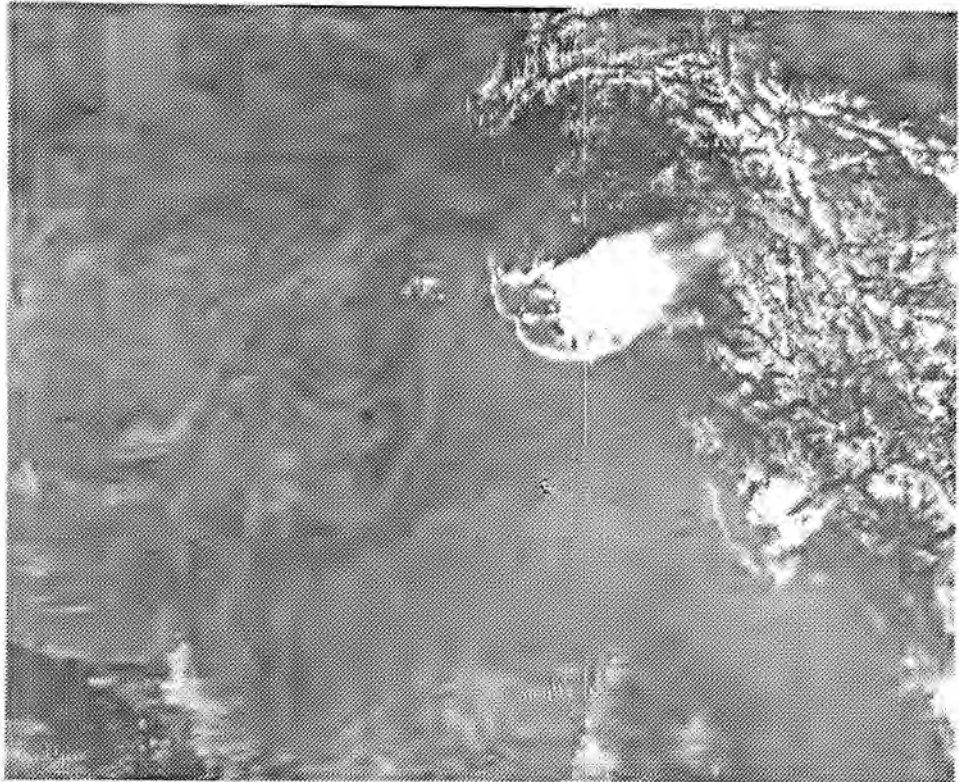
Figure 3.11.   DMSP image of arc cloud lines over Afghanastan at 0512 GMT on 29 June 1985.

Movie film strip analyses of high resolution visible GOES imagery
have shown that CONVECTIVE SCALE INTERACTION IS OF PRIMARY IMPORTANCE
IN DETERMINING THE DEVELOPMENT AND EVOLUTION OF DEEP CONVECTION
(Purdom, 1979; Purdom and Marcus, 1981; Bohan 1981). This interaction
manifests itself as the merger and intersection of arc cloud lines with
other convective lines, areas and boundaries (Purdom, 1979).

The convective scale interaction process is fundamental to the
evolution and maintenance of deep convective activity -- until
recently, it was only observed by satellite. In fact, thunderstorm
evolution that appeared as random using conventional radar has been
observed to be well ordered when viewed in time lapse using high
resolution geostationary satellite imagery.

Since this earlier work of Purdom, numerous investigators have
begun to study the effects of thunderstorm outflow on new storm
generation. Achtemeier (1983) in studying the relationship between the
surface wind field and convective precipitation in Missouri found,

> the preferred area for new cell development were in
> agreement with the findings of Purdom ... eight of the
> fourteen rain cells related to gust fronts formed at the
> intersection of gust fronts, or at the intersection of gust
> fronts with network scale convergence zones.

Holle and Maier (1980) traced two outflows across the FACE mesonetwork
and found an intense thunderstorm with a weak tornado formed at their
intersection. Based on the observational studies of Purdom (1979) and
Sinclair and Purdom (1982), Droegemeier and Wilhelmson (1983) used a
three dimensional cloud model to study the convective scale interaction
phenomena. Figure 3.13 is an adaptation from Droegemeier and
Wilhelmson (1983), and shows their results using a three dimensional
numerical cloud model to study thunderstorm outflow collision with a
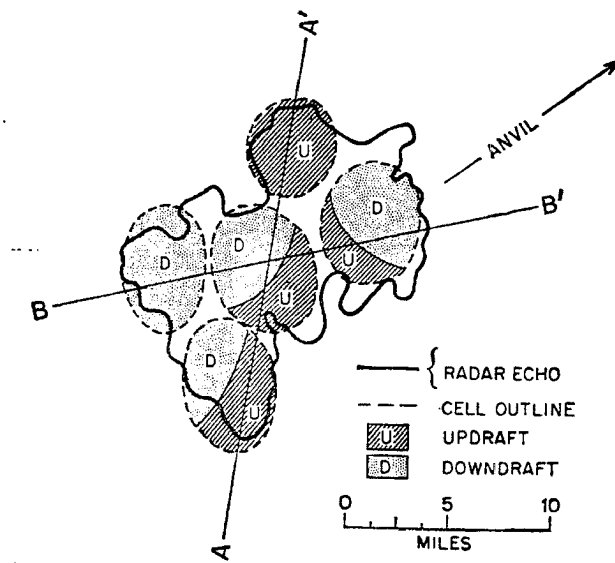
Figure 3.12. Three-dimensional structure of a thunderstorm containing several cells. In the above figure, the thunderstorm and its cells are represented in map plan. U stands for updraft, D for downdraft. From Byers and Braham, 1949.
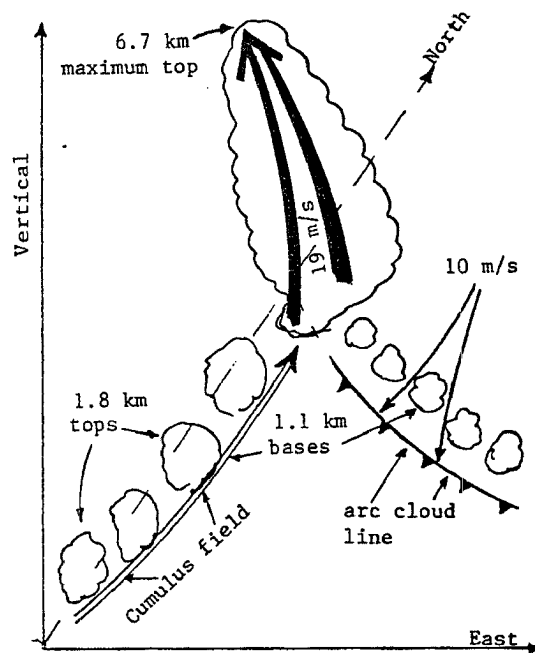
Figure 3.13. Adaptation of numerical modeling results of thunderstorm outflow collision with a convective cloud line, from Droegemeier and Wilhelmson.

convective cloud line. In that simulation they found a deep convective

cloud with maximum vertical motions on the order of 19 m sec^{-1}

developed where the outflow interacted with the convective cloud line.

They noted that such convective scale interaction was not observed in

the simulation where the outflow moved into clear regions. Convective

scale interaction has also recently been observed by Wilson and Carbone

(1984) using Doppler radar data to investigate new thunderstorm

generation at the collision of two thunderstorm outflows.

Examples of convective scale interaction are shown in the

three cases that follow. In these cases hand drawings beside the

satellite imagery are on a map base with the same projection as that of

the image.

3.2.1. Case 1, 26 May 1975 (refer to figures 3.1a - 3.1c)

This is a case of selective development of deep convection along

the outflow of a large mesoscale system. While the development of

severe thunderstorms at the intersection a thunderstorm outflow

boundary with an organized convergence boundary seems to be fairly well

recognized, (Miller (1972), Purdom (1976 and 1985), Maddox et al

(1979)), why deep convection forms along one portion of an arc cloud

line but not another as it advances into a "uniform" warm sector is not

well understood. Inspection of figures 3.1a -3.1c reveals a large

variation in thunderstorm activity as the arc cloud line moves through

Arkansas into northern Louisiana and the border area of Mississippi and

Arkansas. Why this variation? The answer lies in the variations in

the cumulus field through which the arc cloud line moves. In

figure 3.1a, there is deep convection along the arc cloud line from A

to C. A little under two hours later, figure 3.1b, significant changes
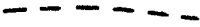
in the distribution of deep convection along the arc cloud line have
occurred:

1) thunderstorm activity continues along the arc cloud line's
   western portion, A, as it moved through the fairly homogeneous
   cumulus field to its south;

2) near the middle of the arc cloud line, at B, thunderstorms
   dissipated as the arc cloud line moved into the clear area, E;

3) strong thunderstorms developed at C as the arc cloud line
   merged with developing convection to its east.

Two hours later, figure 3.1c, intense convection continues at C,
however there has been a complete reversal in the type of convection at
other locations along the arc cloud line. Thunderstorm activity along
segment A dissipated as the arc cloud line moved into the clear area D;
yet along B to its east, new thunderstorms formed as the arc cloud line
moved into the convective cloudiness to the south of E. A severe
thunderstorm has developed along the Texas and Oklahoma border where
the arc cloud line has interacted with a stationary frontal zone. This
correlation between arc cloud line and convective cloud merger leading
to deep convective development, as well as no deep convection forming
along an arc cloud line as it moves into a clear region is even more
dramatic when viewed in movies made from the 15 minute interval imagery
that was available on this day; see for example the film by Bohan
(1981).

3.2.2. Case 2, 25 June 1978

This case illustrates the role of convective scale interaction along a sea breeze frontal zone. In this case the following symbols are used:

(1) sea breeze zone; ⎯ ⎯ ⎯ ⎯ ⎯ ⎯

(2) arc cloud line outflow boundary; ⎯▲⎯⎯⎯▲⎯⎯▲⎯

(3) radar echo (from Daytona Beach); ●

(4) cloud area. ◯

Figures 3.14a - 3.14e show typical thunderstorm development and evolution along the sea breeze front. In figure 3.14a, an arc cloud line (A) has moved into southwest Florida triggering convection where it intersects the west coast sea breeze at location B. Like a chain reaction, the storm produced at location B produces an outflow arc cloud line that triggers new convection along the sea breeze eventually resulting in the thunderstorm at B', figure 3.14e. As the arc cloud line A moves eastward and decays, new deep convection develops along it at location C in figure 3.14b. The convection at C in turn produces another arc cloud line boundary, D in figure 3.14c. Another arc cloud line, produced by the thunderstorm activity at E, merges with the arc cloud line boundary produced at D causing a rapid increase in thunderstorms there, figure 3.14d. Along its northern edge, the arc cloud line produced by the thunderstorm activity at location E merges with the southern end of the large arc cloud line due to the storm at location B (figure 3.14d) triggering the large thunderstorm at F by 2301 GMT, figure 3.14e. Similar type interaction is evident all along the east coast sea breeze. As the thunderstorm at G dies, figures 3.14a - 3.14b, its outflow arc cloud line triggers new
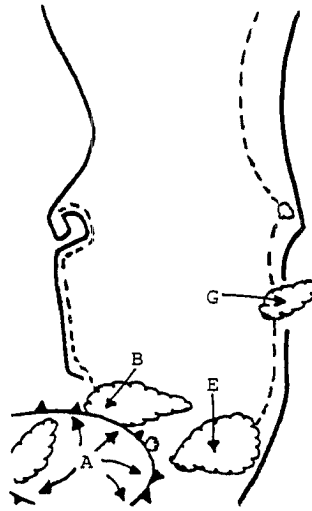
Figure 3.14a. 1230 EST, 25 June 1978. Details in text.
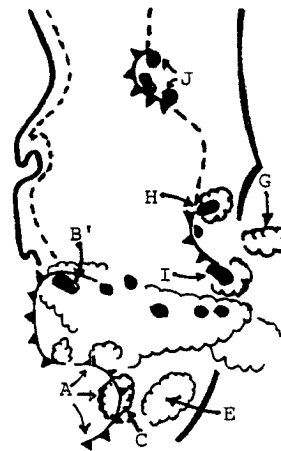
Figure 3.14b. 1430 EST, 25 June 1978. Details in text.
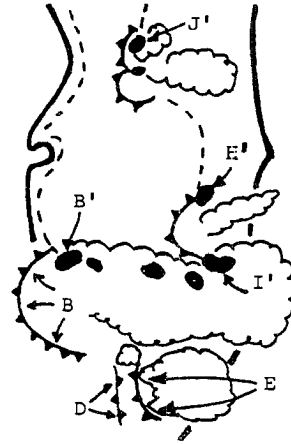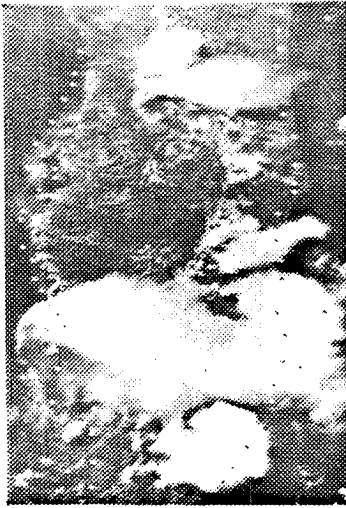
Figure 3.14c.   1531 EST, 25 June 1978.   Details in text.
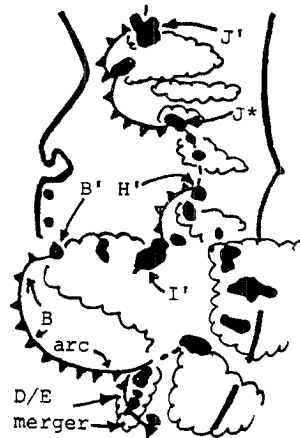
Figure 3.14d.   1631 EST, 25 June 1978.   Details in text.
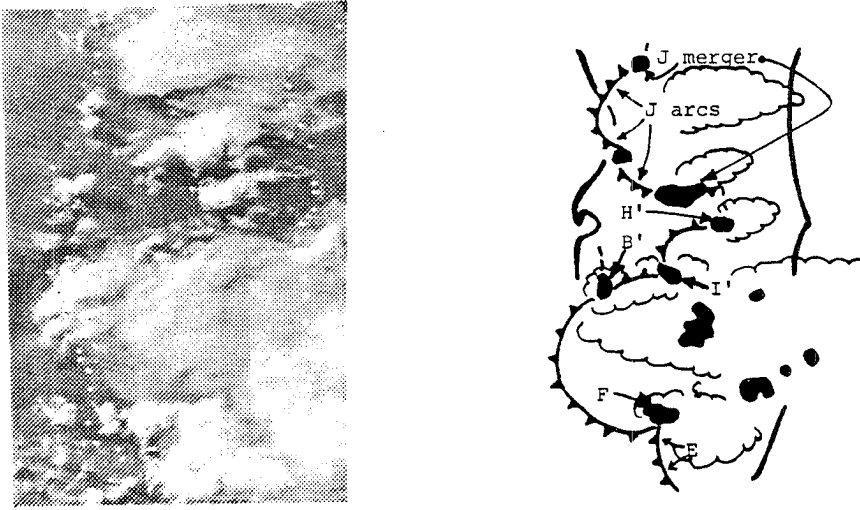
Figure 3.14e.   1801 EST, 25 June 1978.   Details in text.

thunderstorms along the sea breeze both to the north at H and to the south at I, figure 3.14b. As with storm B to storm B', the chain reaction begins, eventually resulting in storms at H' and I' in figure 3.14e. The thunderstorm array at J in figure 3.14b behaves in the same manner. J's initial outflow is reinforced by new thunderstorms that form both to its north and south as it intersects the sea breeze front. This reinforced outflow region from J eventually travels across Florida and triggers thunderstorms along the west coast sea breeze front, figure 3.14e. By the end of the day, nearly every thunderstorm shown in the imagery is a direct result of the sea breeze frontal zone's interaction with thunderstorm produced arc cloud lines, as well as that of arc cloud line interactions with one another.

3.2.3. Case 3, 28 July 1977

This is a case of summertime convective development over the midwestern United States. Symbols are the same as for the previous case. Trying to understand the evolution of deep convection using only surface observations and radar data is virtually impossible. This case is no exception to that rule. However, using high resolution three minute interval satellite imagery and the concept of convective scale interaction makes the evolution of convection over the five hour period spanned between figures 3.15a and 3.15b understandable. By 1900 GMT, figure 3.15c, precipitating convection has developed southwest of Oklahoma City at location A: this storm exerted a major control on deep convection that formed through Oklahoma during the day. Other rain areas have developed north of the Red River at locations B and C, and along an early morning cloud/clear boundary in Texas at D. By 2023 GMT, figure 3.15d, arc cloud lines have been produced by the storms at

Figure 3.15a. 1130 CST, 28 July 1977. Details in text.
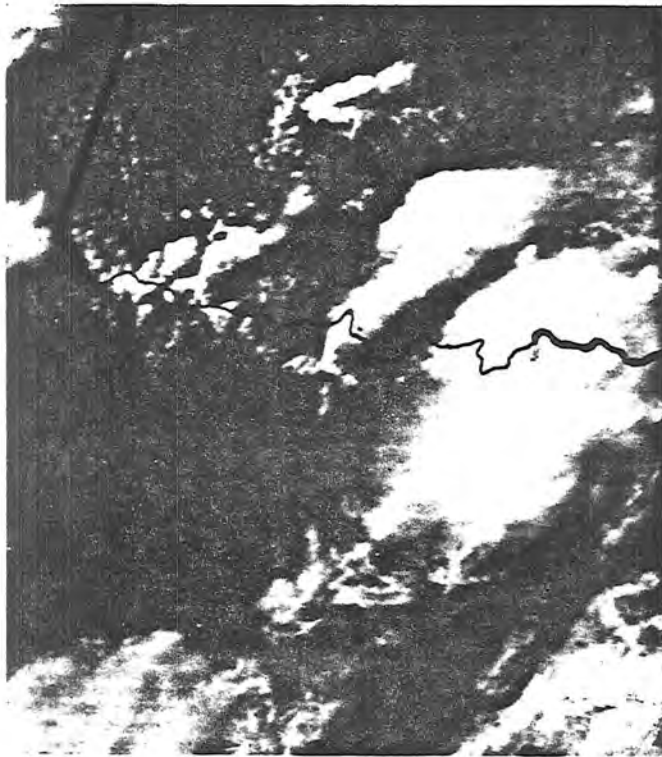
Figure 3.15b. 1630 CST, 28 July 1977. Details in text.
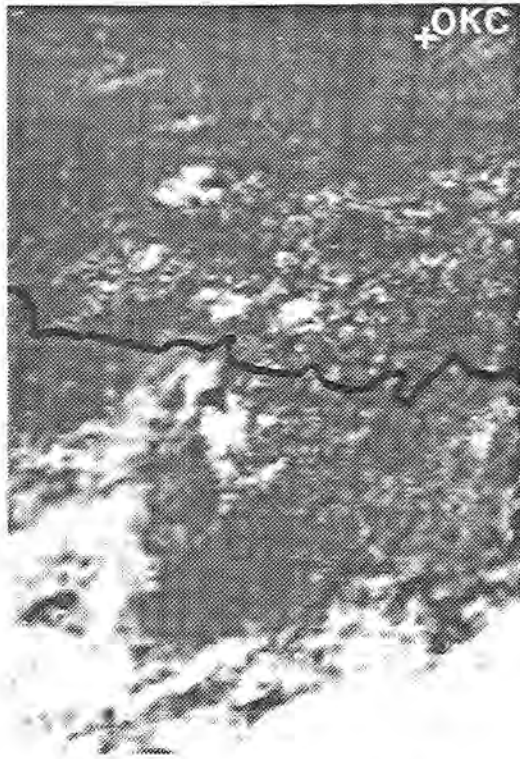
Figure 3.15c.   1300 CST, 28 July 1977.   Details in text.
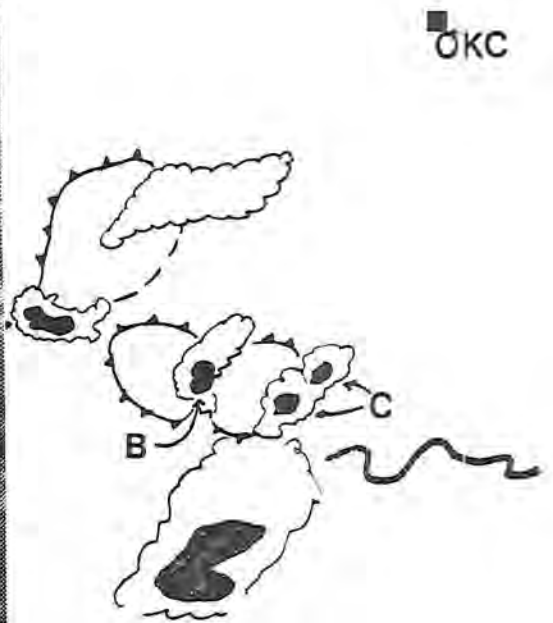
Figure 3.15d.   1423 CST, 28 July 1977.   Details in text.
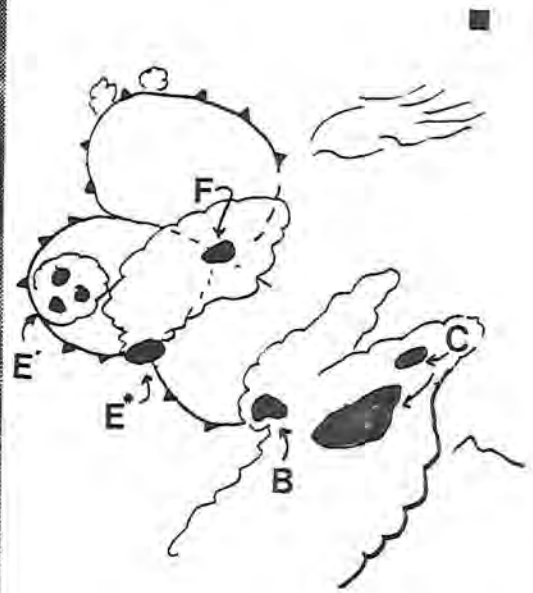
Figure 3.15e. 1524 CST, 28 July 1977. Details in text.
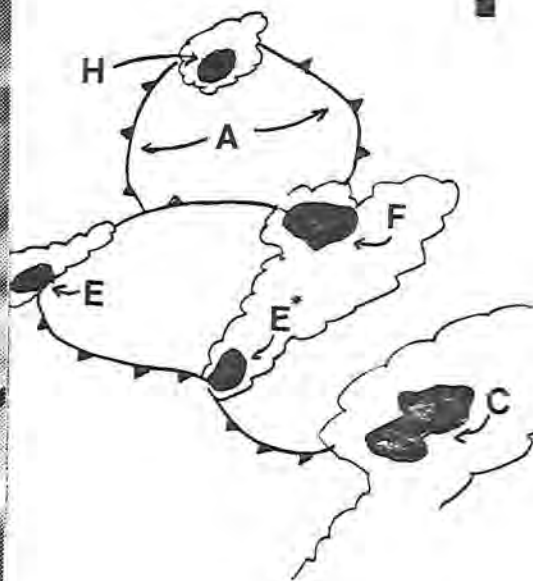
Figure 3.15f. 1609 CST, 28 July 1977. Details in text.

locations A, B and C. Note that the echo at location A has dissipated, and its outflow has helped trigger a new storm as it merged with the convective region E. By 2214 GMT, figure 3.15e, the storm at E had split into E' and E*, with E* moving eastward as its outflow interacts with the arc cloud line produced by the storm at locations B. The precipitation area at E' develops to its west as its outflow continues to merge with the convective cloudy region there. In a manner similar to E*, the thunderstorm at B continues to move eastward along the outflow boundary left by C, while the thunderstorm area at C continues to develop eastward. A new thunderstorm has formed at F where the northern portion of E's outflow merges with the outflow from storms A and B. By 2209, figure 3.15f, the development at F, E' and E* continues as in figure 3.15d. By the end of the day, a new thunderstorm has been triggered at H by the outflow from storm A, merged with the convective regime to the north. Note that storm A had dissipated over three hours prior to the new storm's development at H. The analyses presented for this case in conjunction with three minute interval GOES imagery and Oklahoma City radar imagery make up one of the more spectacular segments in the film, "The importance of thunderstorm outflow boundaries in the development and evolution of deep convection," (Bohan, 1981).

3.3. Summary of Convective Scale Interaction Properties as Observed in GOES Satellite Imagery

Convective development similar to the type shown in this chapter occurs daily during the convective season. From these observations, some very important new facts concerning deep convective development and evolution may be surmised.

- Thunderstorm outflow boundaries may maintain their identity as arc clouds for several hours after they have moved away from their parent source.

- The arc cloud line outflow boundary can, and often does, cause deep convection to develop along it at distances well over 150 kilometers from its point of generation.

- Deep convective development along an outflow boundary is a selective process - it only occurs where the arc cloud line merges with a cumulus region or intersects another boundary. When the arc cloud line moves into clear skies no deep convection develops.*

- As the convective regime evolves on a given day, and much of the cumulus field dies away, the majority of the new thunderstorms that develop are confined to arc cloud line intersection points.

As was shown in this chapter, deep convection is initiated by convective scale interaction between arc cloud lines and other boundaries or existing convection. A question naturally arises concerning the importance of convective scale interaction in convective storm genesis and ensuing precipitation versus other storm generation mechanisms. The next chapter will address that question.

---

*While this statement is true for areas with abundant low level moisture, such as the southeast United States, it may not always be true in more arid regions such as the High Plains of the United States.

4.0   THE SIGNIFICANCE OF CONVECTIVE SCALE INTERACTION IN THE
      DEVELOPMENT OF NEW DEEP CONVECTION AND PRECIPITATION*

To assess the relative importance of arc cloud lines in the
development and evolution of deep convection, a storm generation
mechanism classification study was undertaken. The area chosen for the
study was the portion of the southeast United States shown in
figure 4.1, an area of approximately 7.7×10^5 km^2. For the study,
GOES-East 1 km resolution visible imagery and 8 km resolution enhanced
infrared imagery were used to classify convective development with
respect to storm generation mechanism and storm intensity. The
sections that follow discuss: 1) Factors influencing the geographic
area chosen for the study; 2) the time period chosen for classification
of convective generation mechanisms; 3) the decision to use GOES VISSR
data for classifying both storm generation mechanism and storm
intensity; 4) the mechanics of how the study was performed; 5) results
of the study which identify major thunderstorm trigger mechanisms as a
function of the time of day; and 6) a comparison of those results (5
above) with rainfall over the area during the study period.

It is important to note that no mesoscale convective complexes,
MCC's (Maddox, 1980), were observed over the study area during the
study period. This was determined by an inspection of a climatology of
the MCC (Bartels, et al., 1984). Indeed, MCC's are rare events over
the southeast United States during the summertime.

*Portions of this section are based on previous work by the author
(Purdom and Marcus, 1981).
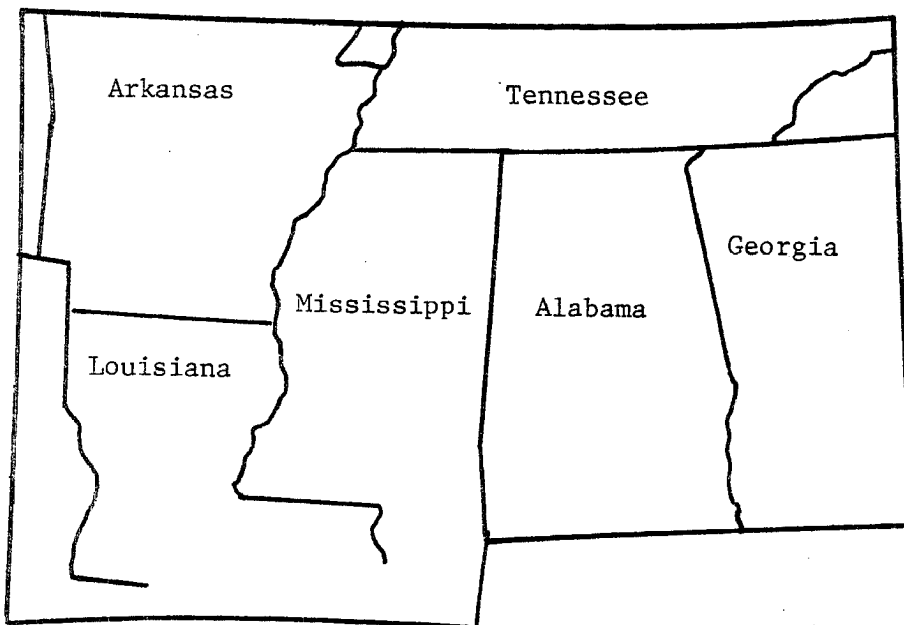
Figure 4.1. Convective study area. Note that Florida and the Gulf of Mexico were not included in this study.

4.1   Factors Influencing the Study

4.1.1.   Choice of data type

While arc cloud lines are readily detected in GOES visible imagery they are rarely observed using conventional radar. Futhermore, the capturing of an arc cloud line in a surface station oriented mesoscale analysis requires an observation in the right place at the right time. As was shown in the previous chapter, arc cloud lines are easily detected using high resolution GOES visible imagery. However, visible imagery are only available during daylight, while GOES infrared data are available 24 hours per day. GOES infrared data are useful in determining storm intensity; unfortunately, with those data it is very difficult to detect local thunderstorm trigger mechanisms such as arc cloud lines. This is because of the GOES infrared detector's poor spatial resolution coupled with its response characteristics (Purdom & Vonder Haar, 1983). Thus, high resolution visible GOES imagery is the only practical observational data set available for undertaking a study over a large geographical area in which arc cloud line interactions are to be monitored.

Upon initial reflection, it might come as a surprise that for this study, GOES infrared data (rather than radar data) represent the best source of information for storm intensity classification. Reasons for this are summarized in table 4.1. One important factor to keep in mind when examining table 4.1 is the requirement for an experiment to be repeatable. Although the data to be discussed were taken during the summer of 1979, others undertaking similar classification studies (regardless of the year) should be able to obtain similar results in terms of both storm generation mechanisms and storm intensity.

Table 4.1

Comparison of the Suitability of Satellite Infrared
Data versus Radar Data for Storm Intensity Classification

GOES Infrared Data	Conventional Radar
1. One uniformly calibrated sensor makes all of the observations for the entire study period	Observations from a variety of radars that are not intercalibrated.
2. Data does not require re-mapping to identify specific storm on visible image and corresponding infrared image.	Data requires re-mapping to satellite coordinates for precision identification.
3. Data source is digital, available on tape (not used) and as enhanced infrared image photographs.	Data source is analog, on 35 mm film.
4. Visible and infrared data are from the same spacecraft. Data are precisely coincident in both space and time.	For a variety of reasons radar data may not be available or cover the area of interest. Precise time matching would be both infrequent and random, if at all.
5. Under certain conditions, cirrus from a thunderstorm anvil may mask weaker convection whose top is at a warmer infrared temperature.	Under certain thunderstorm situations, a radar's display of thunderstorm activity may be rendered unusable due to anomalous propagation.

As shown in table 4.1, there are distinct advantages in using GOES infrared data for classification of storm intensity. However, the question still must be addressed concerning GOES infrared data's suitability for that task. For almost the past forty years, radar reflectivity has been the norm for remotely assessing a thunderstorm's intensity, while GOES infrared data's use in that area has yet to span a decade. How do the two data sets relate in the area of storm intensity assessment? Both satellite and radar data have important roles to play in that area. To help assess storm intensity satellite infrared data provides information about cloud top mean vertical growth rates, cloud top temperature, and anvil expansion rates. On the other hand, conventional radar data provide information about echo reflectivities and their changes in time (Purdom, Green and Parker, 1982). Recent studies have extracted quantitative information concerning thunderstorm intensity from both satellite and radar data. Negri and Adler (1981) found that the location of satellite defined thunderstorms coincided with radar echo locations and that radar reflectivity correlated with satellite based estimates of intensity. Similar results were found concerning satellite defined thunderstorm tops and those defined by radar by Purdom, Green and Parker (1982), Parker (1983) and Green and Parker (1983). Other studies have favorably correlated storm intensity with satellite observed cloud top parameters (Sikdar, et al., 1970; Purdom, 1971; Adler & Fenn (1977, 1979); Pryor 1978). Additionally, infrared satellite imagery are being successfully used by the National Weather Service for routine rainfall estimations in areas of heavy precipitation (Scofield, 1984).

Taking the above considerations into account, one kilometer GOES visible imagery were chosen for classification of storm generation mechanisms, and GOES enhanced infrared imagery were chosen for storm intensity classification.

4.1.2 Choice of study area

Because the data set chosen for classification of generation mechanism was GOES visible imagery, the area over which the study was to be conducted should exhibit a preference for daytime thunderstorm activity - preferably a maxima. Since GOES infrared data are to be used for intensity classification, another type observational data should be available in sufficient quantity to verify the use of the infrared data for that purpose - in this case hourly rainfall data was determined to be the best suited comparative data set. Finally, the study area should cover a large geographical area so that single meteorological events could not contaminate the results.

Several separate studies pointed to the suitability of the southeast United States as the study area. First, as is shown in figure 4.2 from the Thunderstorm Project, the southeast United States can be expected to be data rich for studying afternoon thunderstorm development. Second, as is shown in figure 4.3 from Wallace (1975), there is a distinct preference for thunderstorm activity over the southeast United States to be concentrated during the daytime period chosen for the study. Third, the amount of summertime daytime rainfall received over the southeast United States is much greater than other United States regions exhibiting a preference for daytime thunderstorm activity. This latter point can be seen by inspecting the NOAA Climatological precipitation data for June, July and August 1979 shown
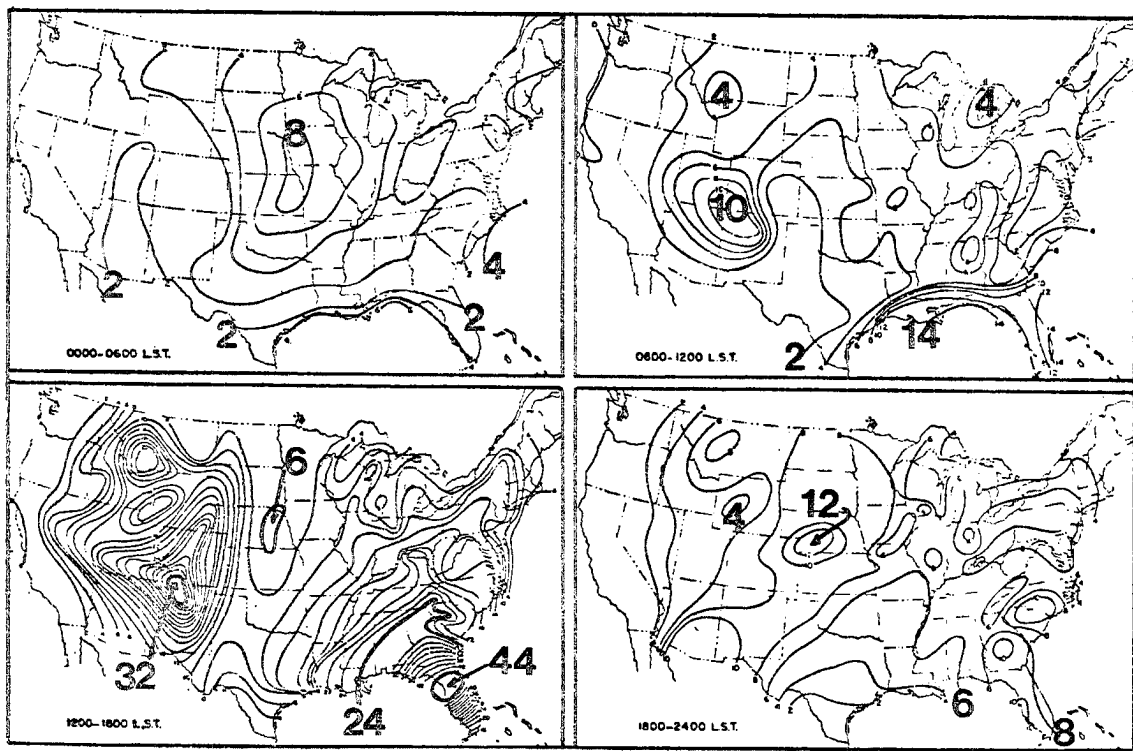
Figure 4.2. Charts showing the average number of thunderstorms
reported during the four quarters of the day for June, July and August.
Isopleths have been geometrically smoothed and, while not
representative of local frequency differences, are fairly reliable for
large-scale differences in frequency. Data used are 20-year averages
(1906-1925) from 192 reporting stations. (Charts taken from U.S.
Weather Bureau Hydrometeorological report No. 5 [55].) From Byers and
Braham, 1949.
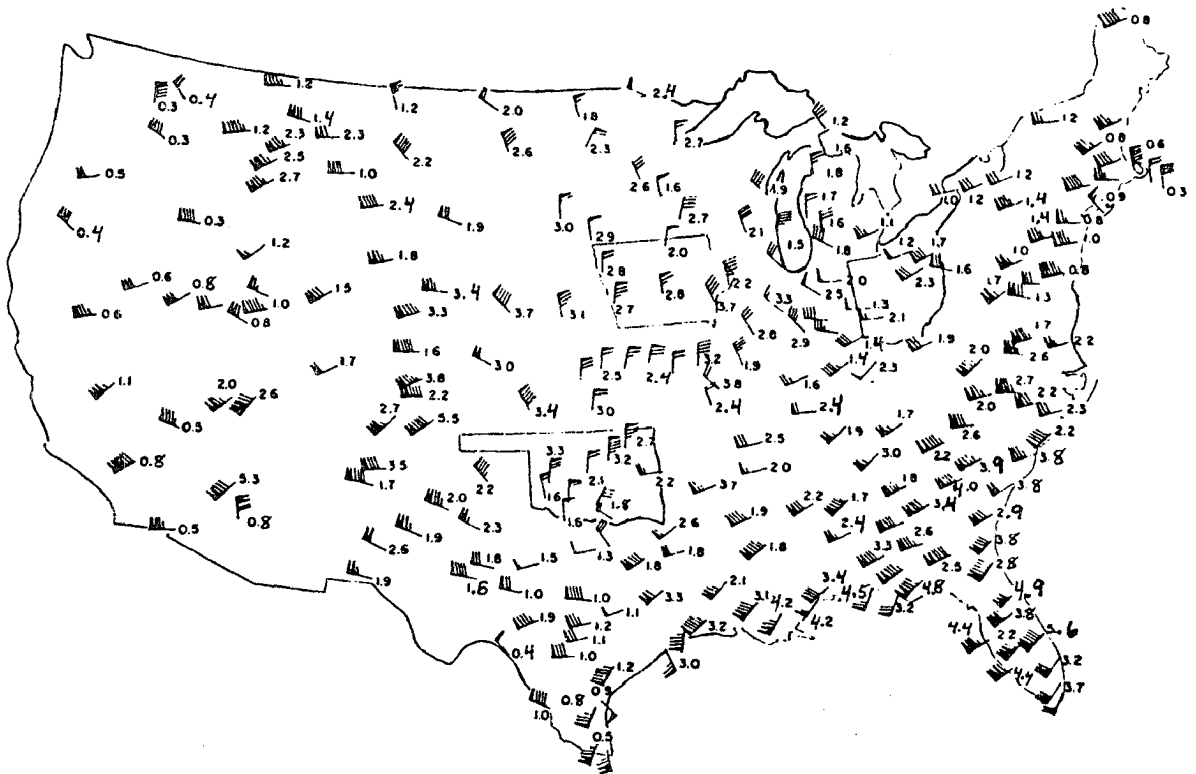
Figure 4.3. Normalized amplitude and phase of the diurnal cycle in the thunderstorm frequency for the summer season (June-August). Normalized amplitude is indicated by the configuration of barbs on the tails of the arrows, where each half barb represents 5%, each full barb 10% and each triangular flag 50%. Stations with circles around them have normalized amplitudes less than 2.5%. Phase is indicated by the orientation of the arrows. An arrow pointing from the north indicates a midnight maximum (local time); one pointing from the east indicates a 0600 maximum, etc. The numbers plotted next to the stations represent the 24-hour mean frequencies in terms of percent of hours with precipitation. From Wallace (1975).

in figures 4.4a, 4.4b and 4.4c. For example, while both the southeast
United States and Rocky Mountain areas show distinct preferences for
afternoon thunderstorms (figure 4.3), the amount of total summertime
rainfall recorded over the southeast United States is nearly an order
of magnitude greater than that recorded over the Rockies.

It should also be noted that during the summertime, the southeast
United States is normally under conditions of weak synoptic scale
forcing with an airmass exhibiting relatively uniform characteristics
covering the area (Willet, 1938). With the southeast United States
covering an area of approximately 7.7 x 10^5 km^2, single meteorological
events influencing weather over a significant portion of the study area
are not common (although six days were omitted from the study because
of tropical storm influences). Finally, numerous hourly rainfall
reporting stations are available over the study area, with an average
density of approximately one station for every 2.8 x 10^3 square
kilometers.

4.2. Mechanics of the Study

Data were analyzed using an image analysis system at NESDIS[*]
(NESS[**] at the time of the study) with capabilities similar to other
state of the art interactive display and analysis systems available in
1979. Input into the system was through a video camera using
operational NESDIS GOES-East image sectors. Those sectors covered
area A, figure 4.5, which provided half hourly 1 km resolution visible

[*]National Environmental Satellite Data and Information Service
[**]National Environmental Satellite Service

Chart II. A. Total Precipitation (Inches), August 1979

SCALE OF SHADES

☐ 0 - 1 Inch

☐ 1 - 2 Inches

☐ 2 - 4 Inches

☐ 4 - 8 Inches

☐ Over 8 Inches

Environmental Data And Information Service NOAA Based on preliminary telegraphic reports
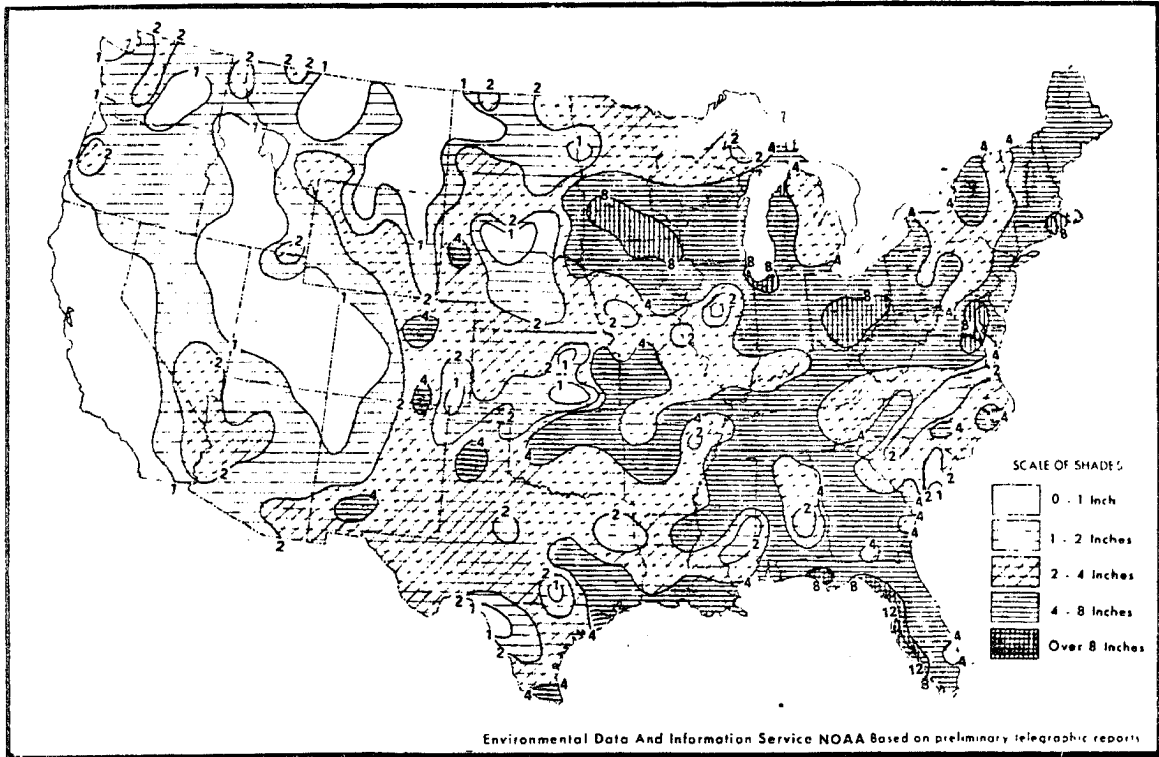
B. Percentage of Normal Precipitation, August 1979

SCALE OF SHADES

☐ Under 50 Percent

☐ 50 to 75

☐ 75 to 100

☐ 100 to 150

☐ Over 150

Environmental Data And Information Service NOAA Based on preliminary telegraphic reports
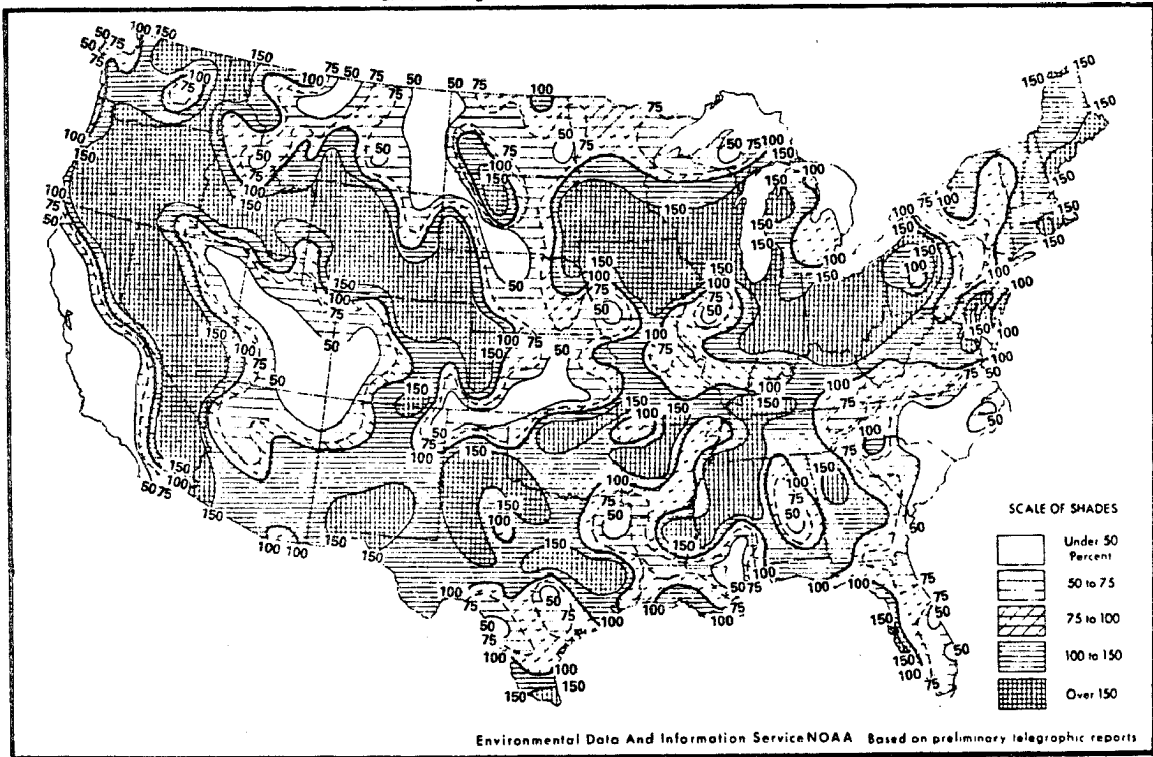
Figure 4.4a. Total precipitation for June 1979 (top), and percentage of normal during June 1979 (bottom).

58

Chart II A Total Precipitation (Inches), July 1979
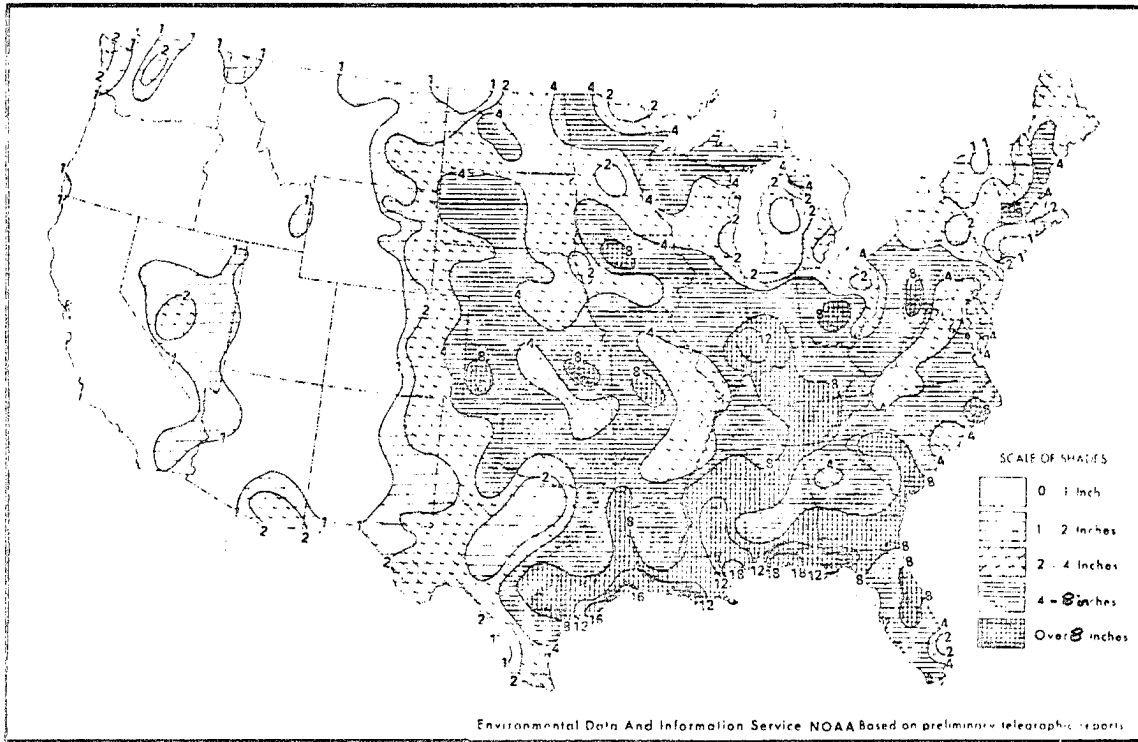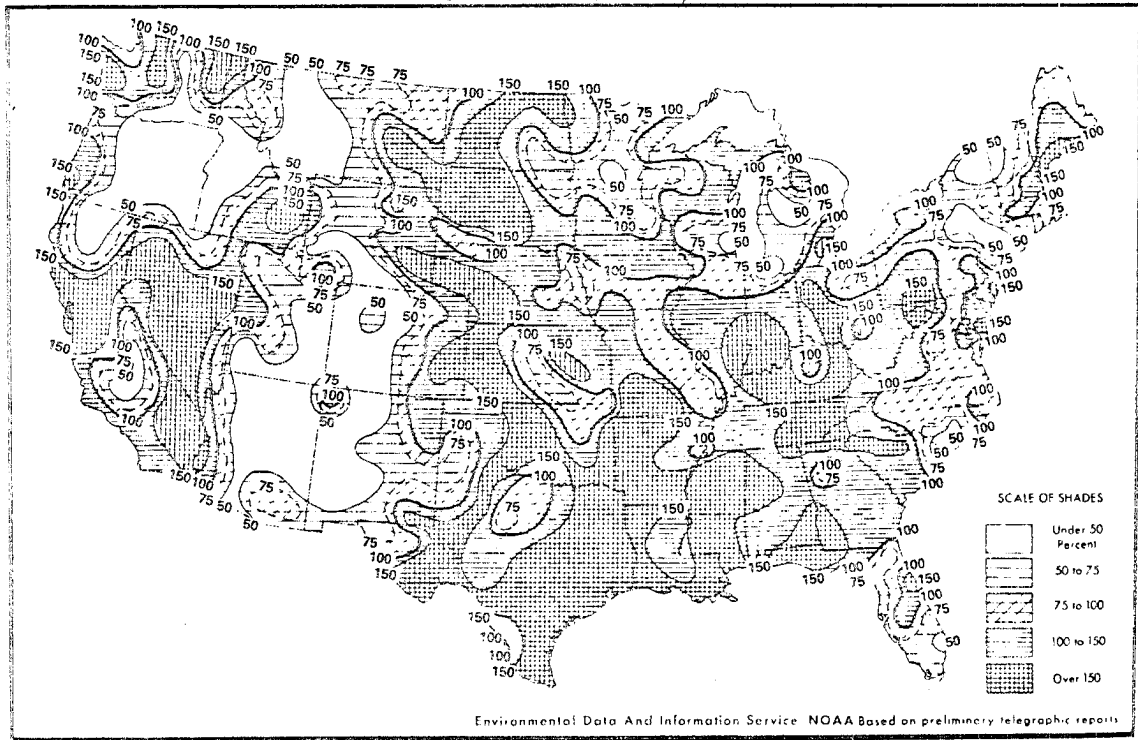
Figure 4.4b. Total precipitation for July 1979 (top), and percentage of normal during July 1979 (bottom).

Chart II. A. Total Precipitation (Inches), June 1979

SCALE OF SHADES

0 - 1 Inch

1 - 2 Inches

2 - 4 Inches

4 - 8 Inches

Over 8 Inches

Environmental Data And Information Service. NOAA Based on preliminary telegraphic reports
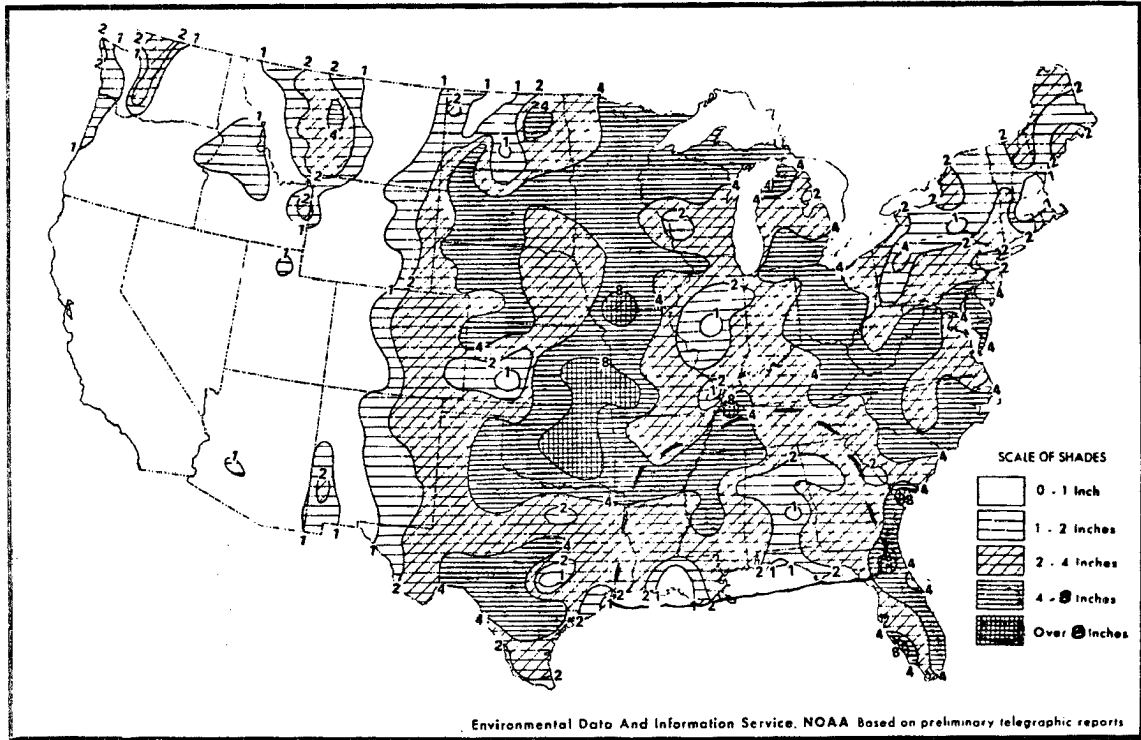
B. Percentage of Normal Precipitation, June 1979

SCALE OF SHADES

Under 50 Percent

50 to 75

75 to 100

100 to 150

Over 150

Environmental Data And Information Service. NOAA Based on preliminary telegraphic reports
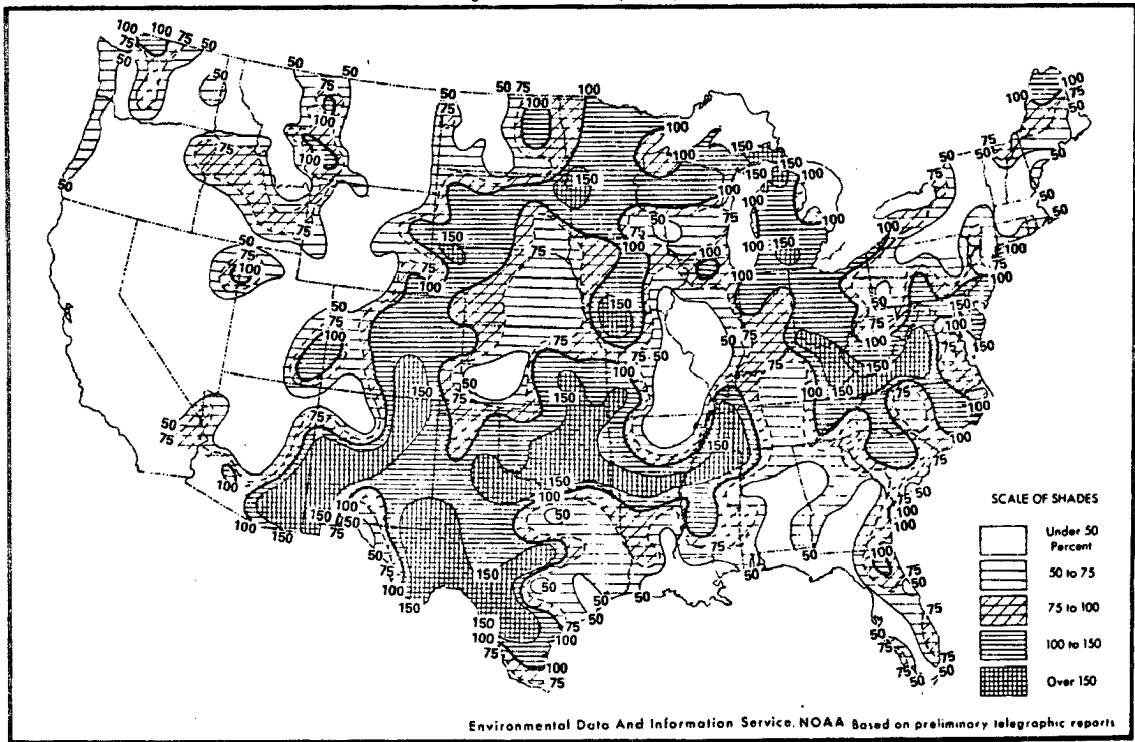
Figure 4.4c. Total precipitation for August 1979 (top), and percentage of normal during August 1979 (bottom).

imagery; and area B, figure 4.5, which provided hourly 2 km equivalent resolution infrared images using the MB enhancement curve, as in figure 4.6.

In the study, convective storms were classified with respect to storm generation mechanism and intensity for the six hour period 1800-0000 GMT (noon to 6 p.m. CST). Intensity was classified using GOES infrared temperature as shown by the MB curve, with all storm tops colder than -20°C classified. Intensity was divided into three levels: a) -20°C to -41°C; b) -42°C to -58°C; and, c) -59°C to -80°C (because of the dynamic range of the analysis system, temperatures less than -80°C were unable to be determined). The -20°C temperature was determined by thresholding capabilities of the image analysis system. That temperature was chosen as an upper bound because of previous satellite-rainfall estimation studies (Griffith, et al., 1978).

Using GOES visible imagery, generation mechanisms were classified into one of four categories: (1) merger, i.e. development of a storm on an arc cloud as it moved into a pre-existing cumulus or cumulus congestus region; (2) intersection, i.e. development of a new storm where two arc clouds came into contact; (3) local forcing, i.e. storm development due to some mechanism not directly involving an arc cloud; (4) indeterminable, i.e., storms whose development mechanism could not be clearly determined, such as new storms that appear from beneath a cirrus deck. Using the imagery analysis system, visible imagery was observed in animation up to 1800 GMT and then hourly from 1800 GMT to 0000 GMT. Interpretation of these animated GOES image sequences were used as a basis for classification of storm generation mechanism. A flicker mode between frames allowed for exact matching between the
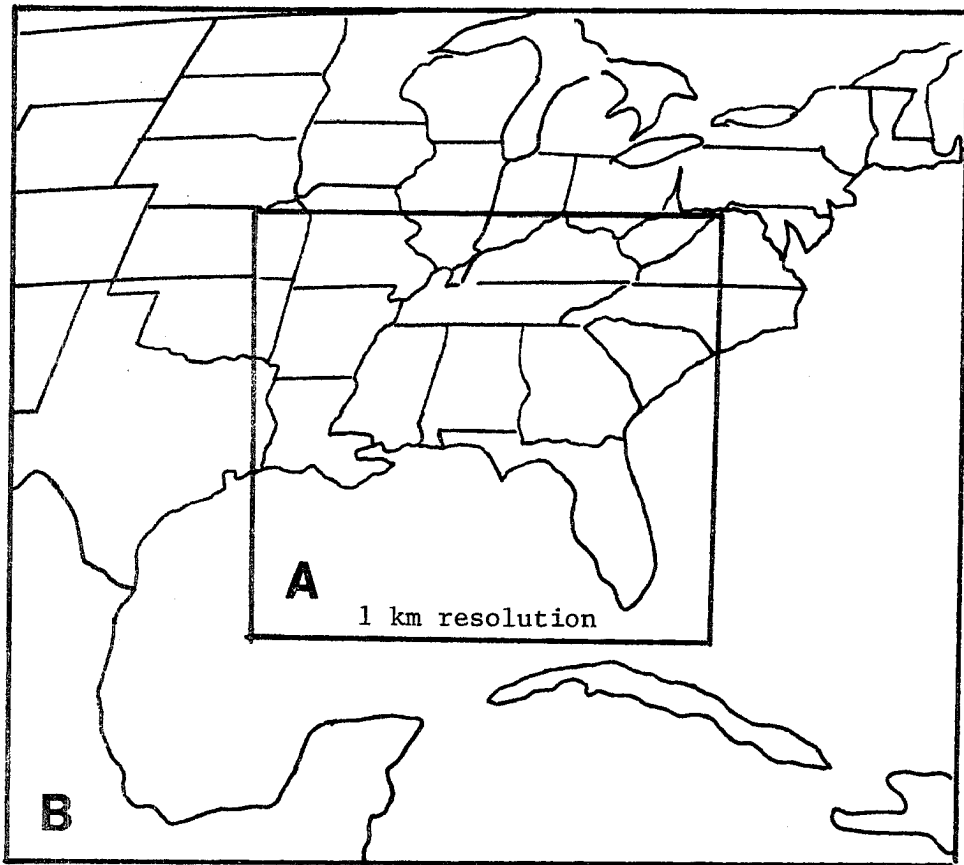
Figure 4.5. Areas covered by A (visible) and B (infrared) sectors.

COUNT VALUE (INPUT)

Figure 4.6. Enhancement Curve MB.
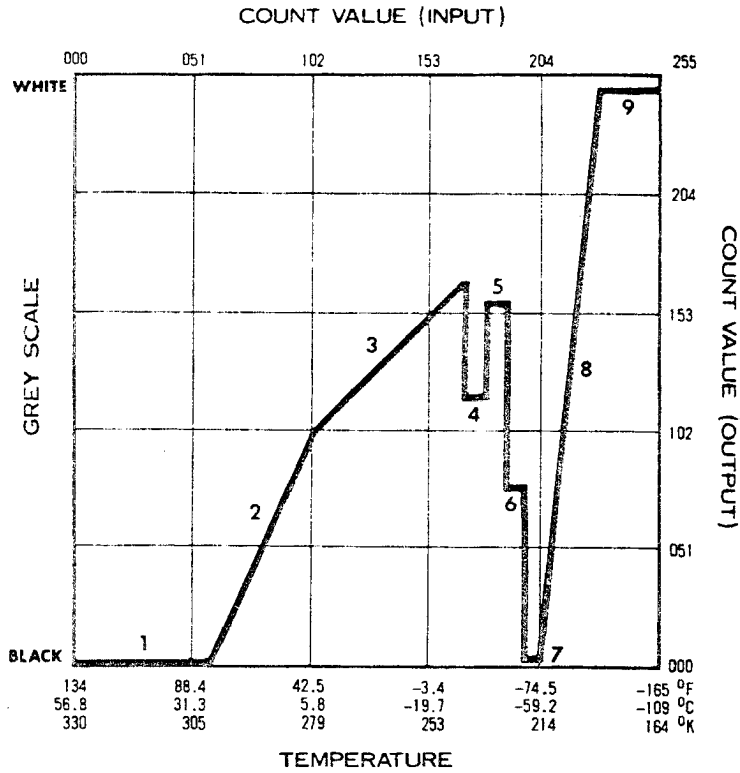
SEGMENT NUMBER	°C TEMPERATURE	COMMENTS
1	58.8 to 29.3	Little or no useful Met Data (Black)
2	28.8 to 6.8	Low Level/Sea Surface Difference
3	6.3 to -31.2	Middle Level - No Enhancement
4	-32.2 to -42.2	First Level Contour (Med Gray)
5	-43.2 to -53.2	(Light Gray)
6	-54.2 to -59.2	Thunderstorm (Dark Gray)
7	-60.2 to -63.2	Enhancement (Black)
8	-64.2 to -80.2	Overshooting Tops Enhancement
9	-81.2 to -110.2	(White)

visible and infrared imagery and as a result, the intensity level for each classified storm could be determined. Storms that persisted longer than one classification time period were classified according to their measured intensity for the next time period, however, their generation mechanism was not allowed to be altered. Thus a storm that developed in the -20°C to -42°C range due to local forcing might interact with an arc cloud line and for the next classification period be in the -42°C to -58°C range: such a storm would be classified as local forcing in the -42°C to -58°C category. In retrospect, it seems that another category to accommodate such storms may have been in order. However, as will be seen in the section to follow, the importance of arc cloud line interactions in new storm generation is clearly evident without the accommodation of such invigorated storms.

4.3. Results

4.3.1. Convective generation mechanisms and storm intensity

9865 storms were classified for 70 of the possible 92 days from June 1 through August 31. This included 23 days each for June and July, and 24 days for August. The reasons for the 22 unclassified days were: a) four days due to missing data; b) six days due to no convection reaching the -20°C threshold; c) six days due to tropical storms over the study area; and, d) six days due to extensive cirrus overcast masking convection over the study area.

Of the 9865 storms, 2490 occurred in June, 3179 in July and 4196 in August. 3830 of the storms fell in the intensity category -20°C to -41°C, 3308 were in the intensity category -42°C to -58°C, and the remaining 2727 were colder than -58°C. Figure 4.7 shows the distribution of the total number of storms for each hour of the
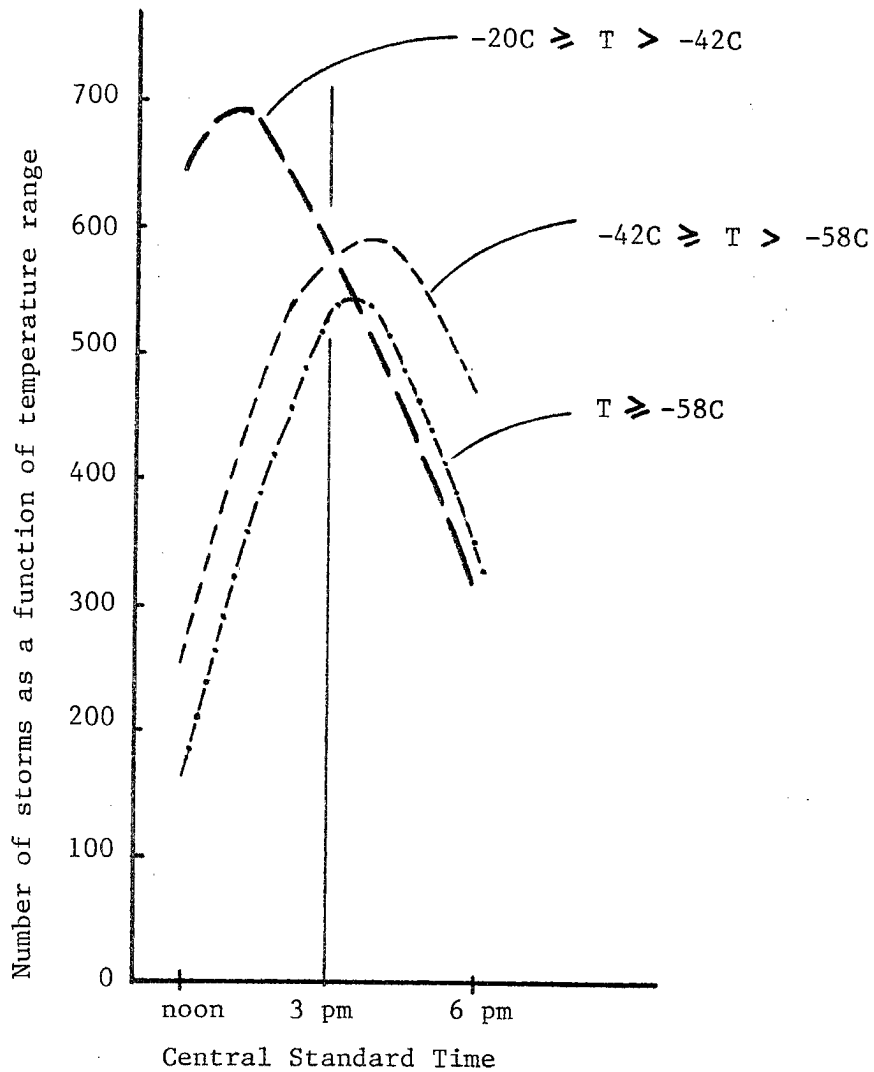
Figure 4.7. Number of storms for each hour of the classification period as a function of temperature range.

classification period as a function of temperature range. The peak

activity for storm tops colder than -42°C occurs in the 2100 to 2200

GMT (3 p.m. - 4 p.m. CST) time frame; this is in good agreement with

the results of Wallace (1975) shown in figure 4.3. Storms in the -21°C

to -41°C cloud top temperature range appear to peak much earlier, in

the 1900 to 2000 GMT (1 p.m. -2 p.m. CST) time period. One possible

reason for the apparent earlier peak in the weaker convection is that

as the stronger convection (colder than -42°C) increases, anvil debris

may spread out and mask the warmer top convection.

Figures 4.8a and 4.8b show the distribution of all storms due to

convective generation mechanism (merger, intersection, local forcing or

indeterminable) by total number each for hour (4.8a) and percentage for

each hour (4.8b). Notice that while early in the day local forcing

dominates as the main convective generation mechanism, later in the day

when the most intense convection has developed, the dominant storm

generation mechanisms are due to arc cloud line interactions. Figure

4.9 shows the percentage of storms in the three intensity ranges due to

arc cloud line interactions as a function of time of day (noon to 6 pm

local). It is significant to note that the more intense the

convection, as shown in figure 4.9, the more important the arc cloud

line interaction mechanism becomes.

These results show quantitatively that convective scale

interaction, transmitted through arc cloud merger and intersection is

the dominant mechanism responsible for the generation of deep

cumulonimbus convection over the southeast United States in summertime.

The development of the very early convection which produces the initial

outflow arcs is a function of the strong diurnal heating (leading to
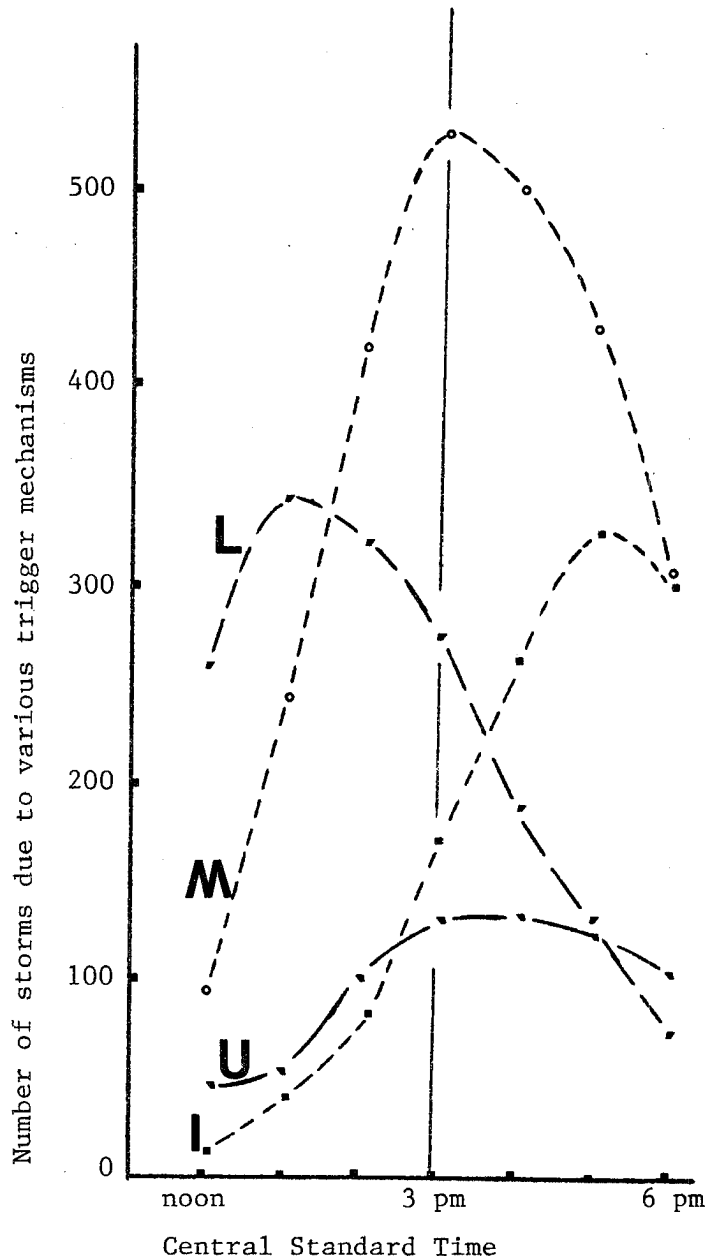
Figure 4.8a. Distribution of number of storms for each hour by generation mechanism. L = Local Forcing, M = Merger, I = Intersection, U = Indeterminable.
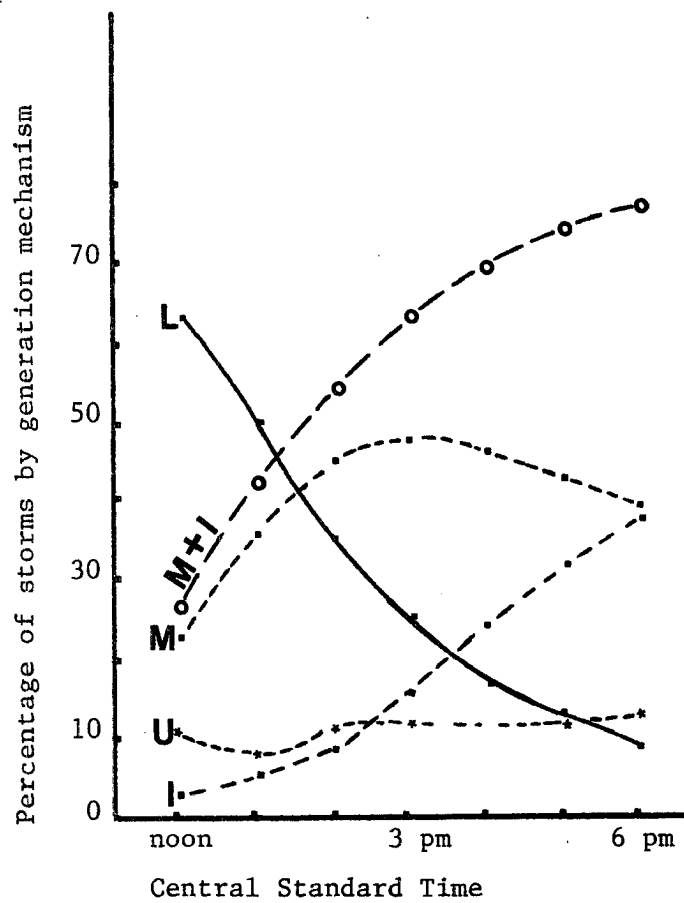
Figure 4.8b. Distribution of percentage of storms for each hour by generation mechanism. For explanation of L, M, I, and U see 4.8a.
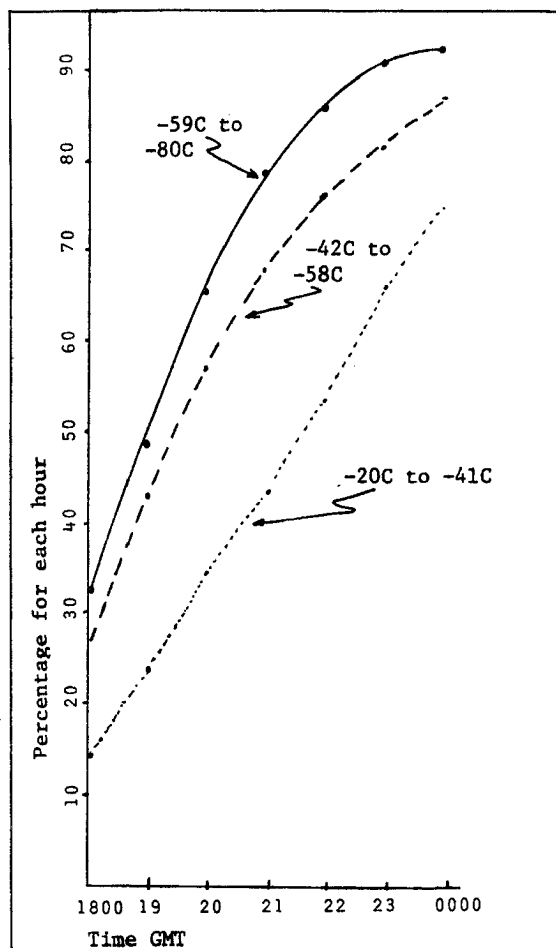
Figure 4.9. Percentage of storms in various temperature ranges due to intersections and mergers for a given hour, assuming indeterminable storms in figure 4.8 are equally distributed. Subtract 6 hours to convert GMT to CST.

preferred storm formation regions due to differential heating) and instability of the airmass characteristic of that region in summertime. However, by the time of the maximum thunderstorm activity as depicted by Wallace in figure 4.3, the majority of the thunderstorms present have been produced by convective scale interaction, figure 4.9.

Storms were observed to form on arc clouds that were relatively young and close to their parent storm as well as on older arcs that were far from their source region. This varying radius of interaction, time and distance between arc cloud line genesis and new storm formation, will be addressed in chapter 6.

4.3.2. Relationship to rainfall

In this section, hourly rainfall data corresponding to the classification results presented in the previous section are examined. The purpose of this examination is to illustrate the strong correlation between storm intensity classification based on temperature and observed hourly rainfall, and to show that the majority of the rainfall that occurs over the southeast United States in summertime is due to convective scale interaction.

Figure 4.10 shows the total measured rainfall over the study area for each hour for the days included in the study period. These data were assembled using hourly rainfall reporting data from NOAA's National Climatic Center. The rainfall amounts are divided into the following categories: a) all rainfall; b) all rainfall of .3 inches/hour or greater; c) all rainfall of .5 inches/hour or greater; d) all rainfall of .7 inches/hour or greater; and e) all rainfall of 1 inch/hour or greater. Notice how the rainfall maximum amounts for each category peak in the 3 p.m. to 4 p.m. time frame. This is the same
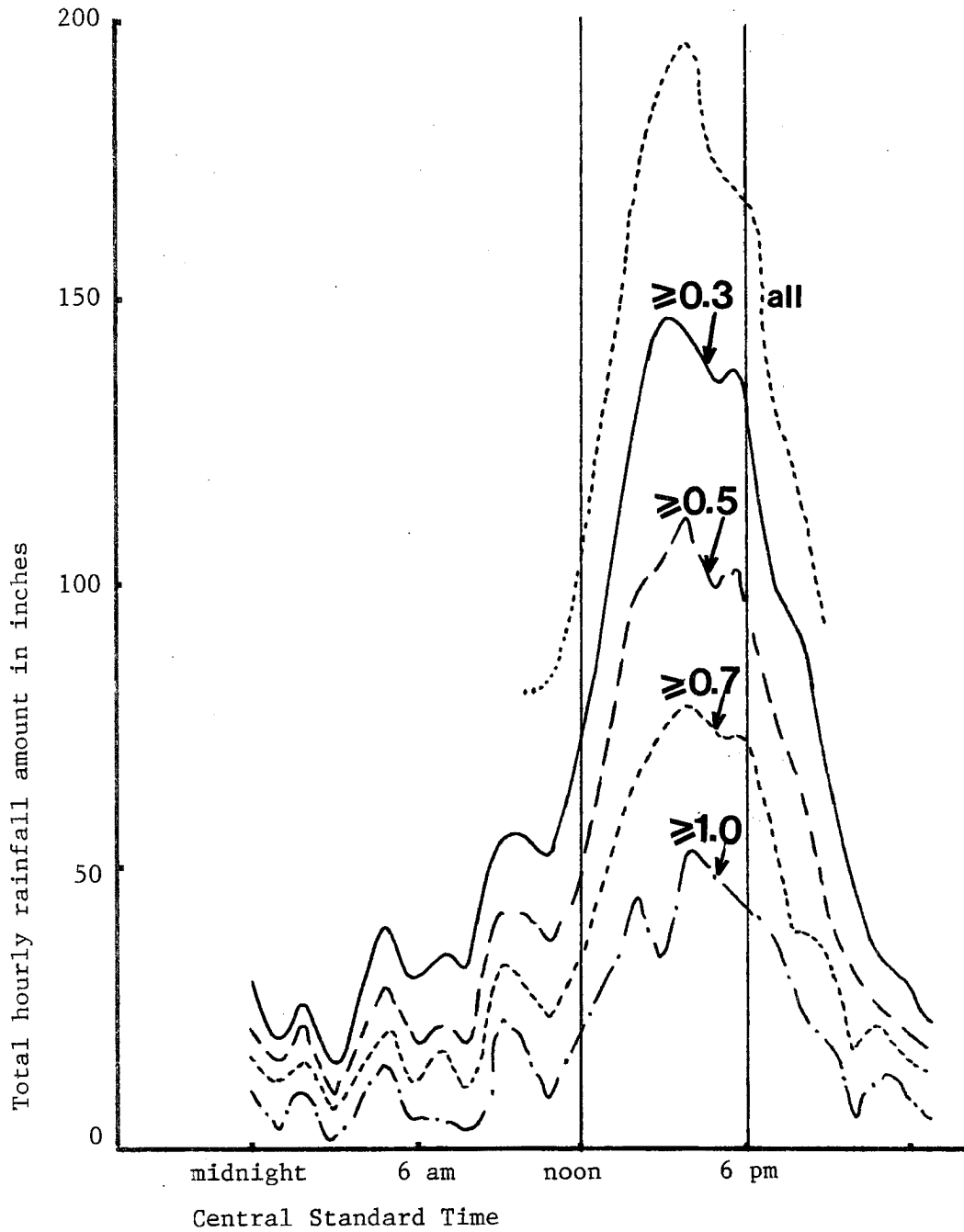
Figure 4.10. Total hourly rainfall measured over the study area for the days included in the study period.

time frame in which storms colder than -42°C were observed to peak, as is shown in figure 4.7, and when the convective scale interaction generation was becoming strongly dominant, as is shown in figure 4.9.

The top portion of figures 4.11a, b and c show the amount of rainfall measured in three intensity categories for each hour during June (4.11a), July (4.11b) and August (4.11c). Those three intensity categories are: 1) all rainfall intensities; 2) all rainfall with an intensity of 0.3 inches per hour or greater; and 3) all rainfall with an intensity of 1.0 inches per hour or greater. The bottom portion of figures 4.11a, b and c show the number of storms from 1800 GMT to 0000 GMT in the three satellite intensity categories for June (4.11a), July (4.11b) and August (4.11c). Referring to the top portion of figures 4.11, it is apparent that the amount of rainfall for July in each of the intensity categories is much greater than the amount of rainfall for either June or August. This observation is supported by monthly rainfall amounts from the National Climatic Center - figures 4.4a, b and c. With July being a much heavier rainfall month, one should expect it to have much stronger convection - this is supported by the satellite intensities for each month shown as the bottom portion of figures 4.11a, b and c. Table 4.2 presents the information in figure 4.11 in tabular form. Notice that in July there are many more storms with an infrared cloud top intensity level colder than -58°C than storms in the same range for June and August.

Table 4.2 shows that the intense rainfall is well related with storms in the colder than 58°C intensity category. Assuming a linear relationship between rainfall intensity amounts and storm intensity, for the category $\geq$.3 inches/hour ($\geq$ 1.0 inches/hour) the majority of
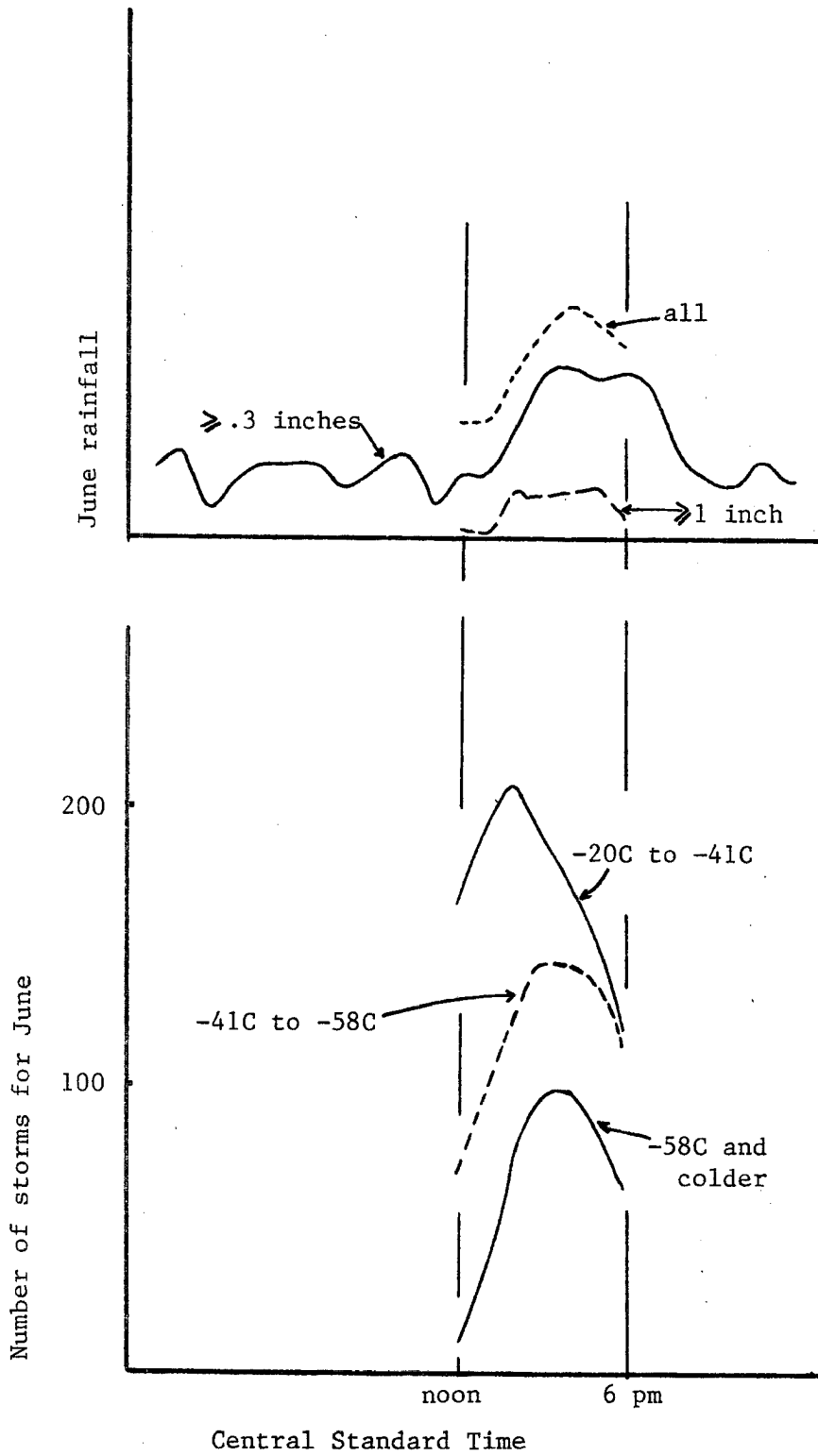
Figure 4.11a. Hourly rainfall by intensity for June (top). Hourly Satellite IR convective intensity for June (bottom).
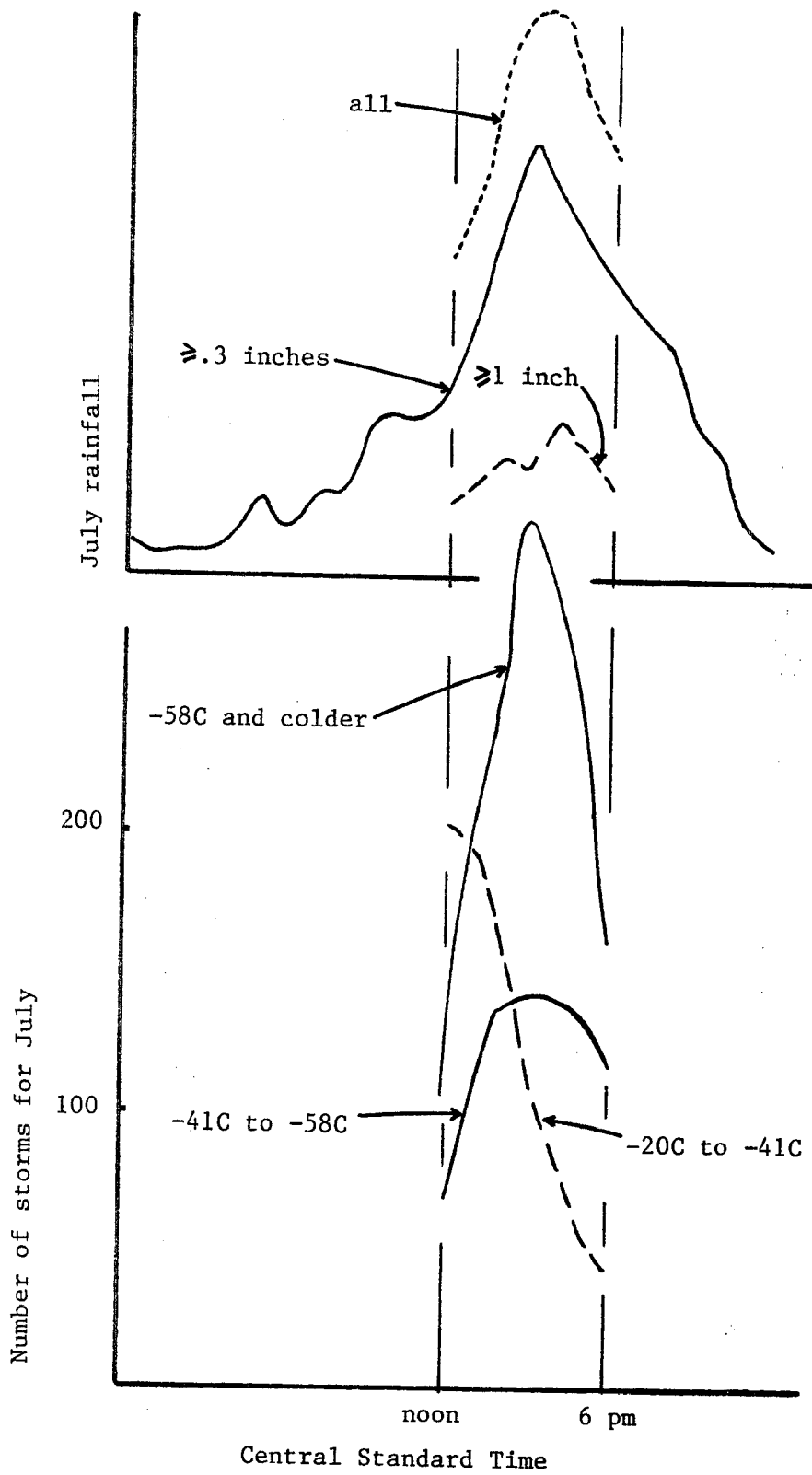
Figure 4.11b. Hourly rainfall by intensity for July (top). Hourly Satellite IR convective intensity for July (bottom).
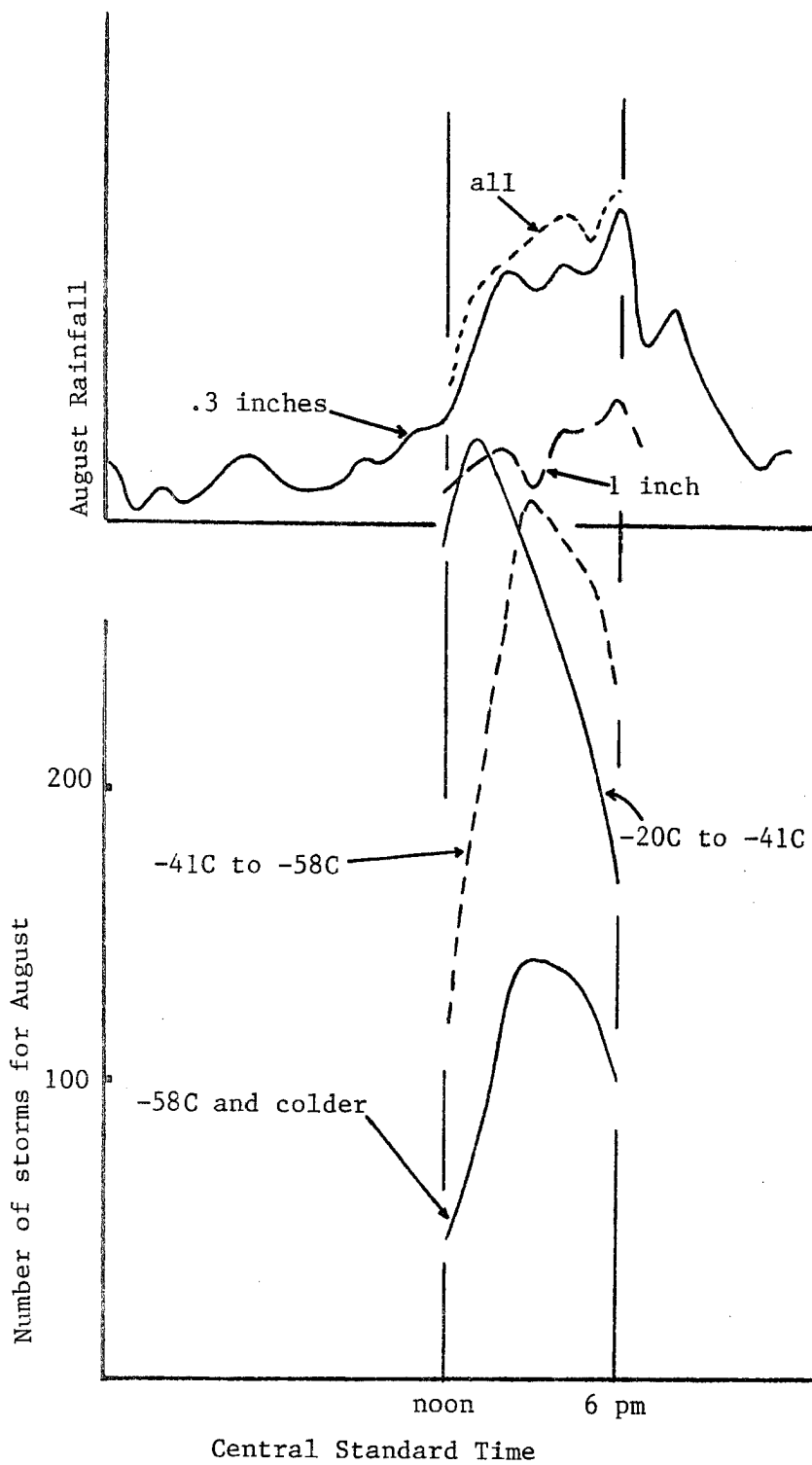
Figure 4.11c. Hourly rainfall by intensity for August (top). Hourly Satellite IR convective intensity for August (bottom).

Table 4.2

Storms and Rainfall for the Summer of 1979
Over the Study Area on Study Days

Month	IR Intensity Level			Rainfall Amount to Nearest Inch for various rainfall rates (inches/hours)		
	−20°to −41°	−41°to −58°	≤−58°	All	≥.3	≥1.0
June	1182	840	468	227	160	43
July	843	829	1507	588	417	144
August	1805	1639	752	317	279	89

the rainfall is explained if storms in the colder than −58°C category

produce about four (ten) times the amount of precipitation as those in

the −41° to −58°C category. Storms warmer than −41°C were not found to

correlate with rainfall $\geq$.3 inches/hour. In fact, storms warmer than −

41°C were not found to correlate well with rainfall at all − this is

felt to be in part due to the cirrus masking problem.

The information presented in this section and the previous

sections may now be combined to illustrate the importance of convective

scale interaction in rainfall generation. Figure 4.12 is a cumulative

rainfall graph with rainfall distributed according to storm generation

mechanism. Notice the dominance of rainfall produced by convective

scale interaction. It is because of convective scale interaction that

the majority of the summertime rainfall occurs over the southeast

United States. IN ORDER TO SUSTAIN DEEP CONVECTION IN A WEAKLY FORCED

ATMOSPHERE, THE CONVECTION THAT RESULTS FROM NORMAL DIURNAL HEATING

MUST BE AUGMENTED BY STORMS PRODUCED THROUGH CONVECTIVE SCALE

INTERACTION.

As has been shown in this chapter the majority of the summertime

thunderstorm activity observed over the southeast United States is due

to convective scale interaction transmitted through arc cloud lines.

Because arc cloud lines are so important to the production of deep

convection and its ensuing rainfall, a series of focused field research

programs were undertaken in which research aircraft data were taken to

study the arc cloud line. Selected examples from those field research

programs are presented in the next chapter.
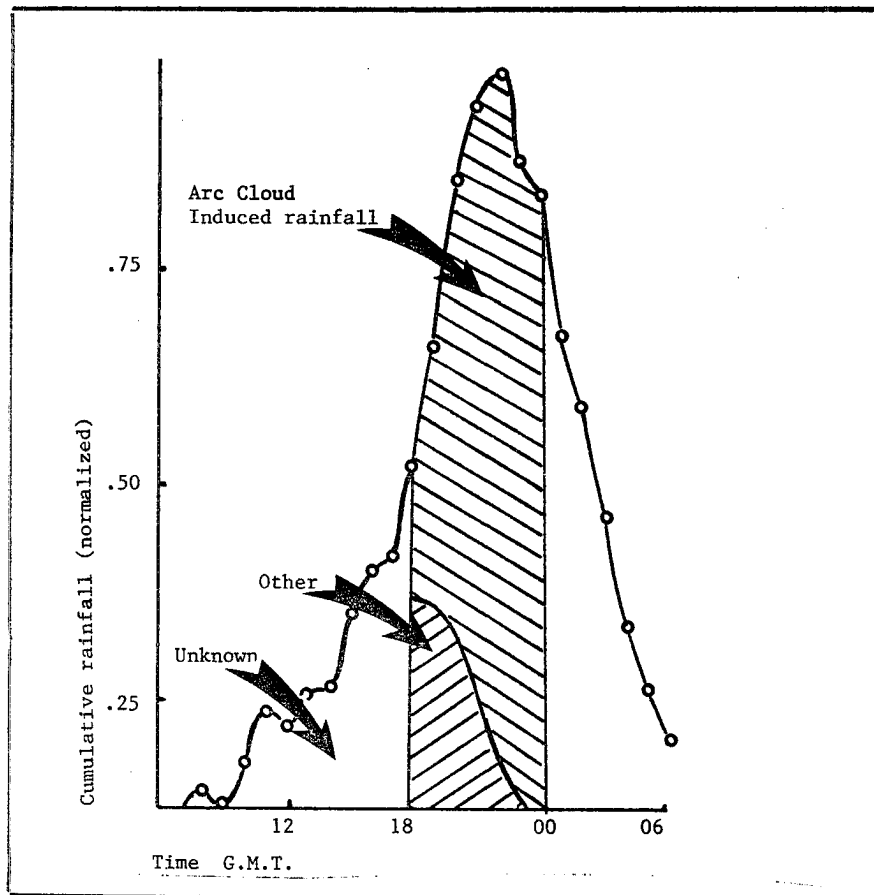
Figure 4.12. Rainfall distributed by mechanism for the study period. Subtract 6 hours to convert GMT to CST.

5.0.   AIRCRAFT OBSERVATIONS OF ARC CLOUD LINES

Because of the basic importance of arc cloud lines and convective

scale interaction and, a series of research aircraft flights

specifically designed to investigate arc cloud lines were undertaken.

Results shown in this chapter are from those flights, (Sinclair and

Purdom, 1983, 1984). In chapter 6, those results are combined with

information from the previous chapters to present a physical model of

the arc cloud line and the process of convective scale interaction.

During the summers of 1980, 1982 and 1983, NOAA and NASA co-

sponsored a research field program in the Colorado high plains* (1982)

and in Florida** (1980, 1983) designed to combine results from research

aircraft flights with rapid scan (3 minutes interval) GOES imagery.

The main purpose of the program was to provide a deeper understanding

of the physical characteristics of arc cloud lines as they relate to

future convective development. P.C. Sinclair operated the aircraft as

pilot/scientist, while J.F.W. Purdom operated the atmospheric data

system as observer/scientist.

5.1.   Observation Systems

5.1.1   Aircraft observational system

The Colorado State University Atmospheric Research Flight Facility

(ARFF) has developed a number of Airborne Atmospheric Data Systems

(AADS) for direct measurement of temperature, dew point, pressure,

atmospheric constituents and the atmosphere's three dimensional velocity field. These systems have been specially designed for a variety of aircraft for measurements in atmospheric systems ranging in size from mesoscale systems and severe thunderstorms to waterspouts and dust devils (Sinclair, 1973, 1974; Leverson, Sinclair and Golden, 1975). A miniaturization of the AADS system was designed and constructed by the ARFF for the Cessna Turbo 207 aircraft used in this experiment, (see figure 5.1). It is believed that this is the first installation of this type on a light single engine aircraft.

Relatively fine structure of the velocity field (u', v', w') is obtained using a gust probe and gyro reference system that is designed to be independent of the aircraft's sensitivity to atmospheric motions and/or pilot induced motions. Temperature and dew point are continuously recorded using a standard Rosemount fast response total temperature sensor and a Cambridge dew point sensor. In addition to the above measurements, a Doppler wind system provides accurate measurements of ground speed and aircraft drift angle. These data, along with aircraft heading and true airspeed provide mean horizontal wind components ($\bar{u}$, $\bar{v}$). Aircraft position data is obtained from VOR/DME and LORAN-C stations along with pressure and radar altimeter instrumentation. Accuracy for measurements of the various parameters is given in table 5.1, while a more complete description of the Cessna Turbo 206 instrumentation system may be found in Sinclair and Purdom, 1984.

5.1.2. GOES Data

Nominal 3 minute interval GOES visible and infrared imagery were taken during the flight periods: the scheduling was the same as the
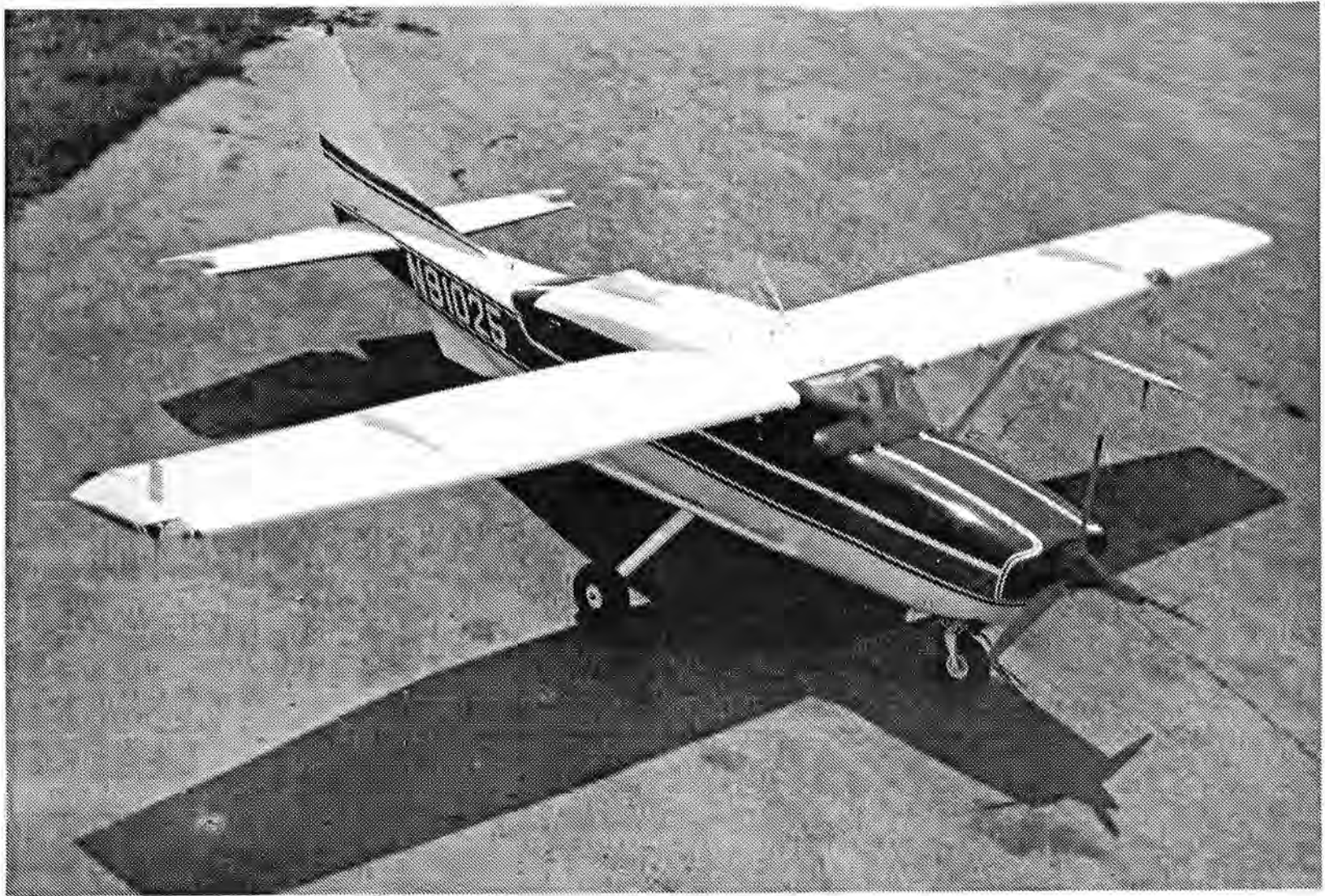
Figure 5.1. Cessna Turbo 207 Atmospheric Research Aircraft, from Sinclair and Purdom, 1983.

Table 5.1

T-207 Instrumentation Measurement Accuracy

Parameter	Relative Accuracy	Absolute Accuracy
Temperature	0.05°C	0.2°C
Dew Point Temperature	0.2°C	0.5°C
u', v'	0.1 msec^{-1}	0.5 msec^{-1}
w'	0.1 msec^{-1}	0.5 msec^{-1}
$\bar{u}$, $\bar{v}$	0.5 msec^{-1}	1.0 msec^{-1}
a/c location	n/a	± 0.3 km

one used in SESAME Operations (Barnes, 1979). The three minute imagery

was taken by the GOES-East satellite, which was located over 75°W at

the equator. The three minute interval images covered the study area

very well, and in all cases, sufficient landmarks were available to

insure aircraft and satellite cloud locations to within the resolution

of the GOES image. Inspection of the satellite data versus aircraft

locations leaves no doubt that the aircraft measurements represent

continuous data sets through the arc cloud lines in the sub-cloud

region.

5.2. Specific Flight Objectives

The major experimental goal was to document with aircraft

observations the dynamic and thermodynamic characteristics of three

critically important regions affecting arc-line cloud development and

evolution. As shown in figure 5.2, those three regions are: (A)

Region 1, the cool thunderstorm outflow; (B) Region 2, the interface

region between the outflow and the environmental atmosphere; and,

(C) Region 3, the arc-line cloud base region. The advantages of this

atmospheric approach over the laboratory tank experiments seems

obvious. In addition, this approach has numerous advantages over the

fixed tower measurements, since it can follow (in time and space) the

three regions of interest as well as extend the vertical measurements

to levels above the maximum tower height.

The flights were designed so that cross-sections and quasi-

horizontal surface presentation of the flight profile data from the

research aircraft might permit the following analyses to be

accomplished:
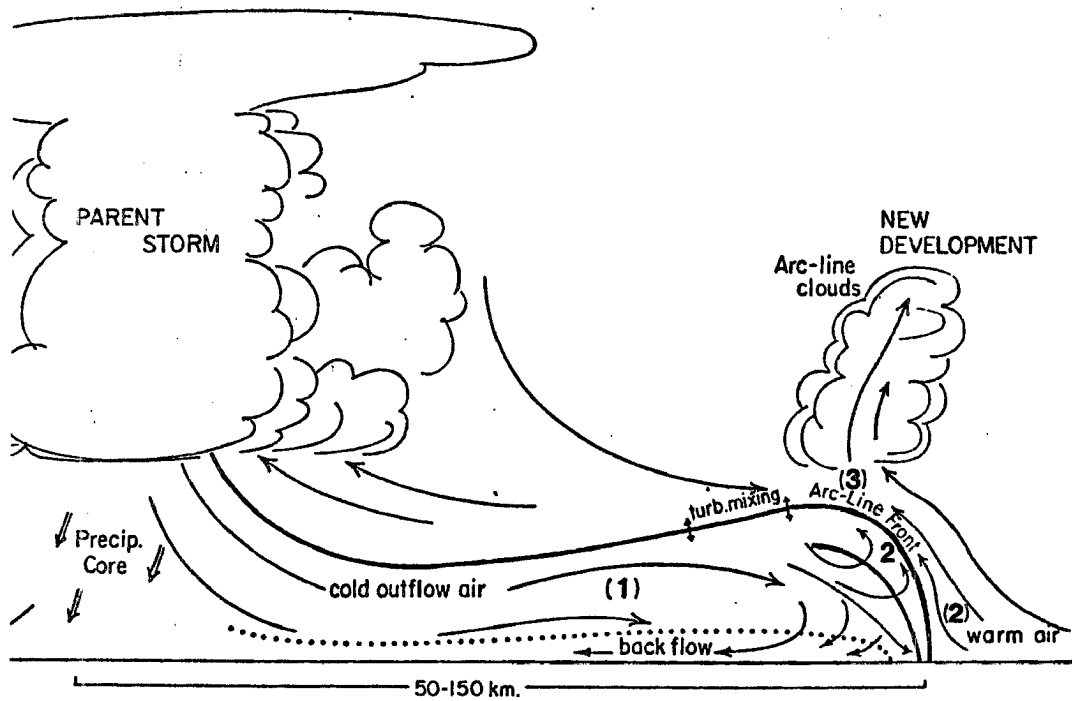
Figure 5.2. Schematic illustration of the arc cloud line showing the three regions for aircraft investigation: 1) Region 1 - cold outflow region; 2) Region 2 - interface region between the cool outflow and warm environment and extending well into the warm environmental air ahead of the outflow; 3) Region 3 - the subcloud layer between arc cloud base and top of the cool outflow air. Based on Sinclair and Purdom, 1983, 1984.

A) Region 1

    a. determine the height and shape of the cold outflow air; and,

    b. verify that subsidence above and within the cold outflow air mass leads to the absence of clouds in this region as observed from rapid scan satellite data.

B) Region 2

    a. investigate the possibility of solenoidal circulations associated with the outflow;

    b. determine if there is lifting of the warm environmental air by the cold outflow air; and,

    c. investigate the buoyancy developed in the pre-gust front and sub-cloud warm air ahead of the arc cloud line.

C) Region 3

    a. investigate the connection between convective element initiation in Region 2 and cumulus cloud development in Region 3.

5.3. Observations

5.3.1. Florida 1980

The research aircraft flights were made between July 15 and July 22, 1980 in the northern to central portions of Florida. Three days of successful arc cloud penetrations were made: July 17 (near Tampa), July 21 (near Sarasota) and July 22 (near Gainesville), see figure 5.3. Times given in the figures are in GMT; to convert to EST subtract 5 hours.

General areas for penetration were chosen using expert advice from NESS (now NESDIS) units that had access to real time GOES data. Once the aircraft reached an area where arc activity had been detected, decisions concerning penetration points were made visually. Penetrations of the arc cloud region were made in clear air generally
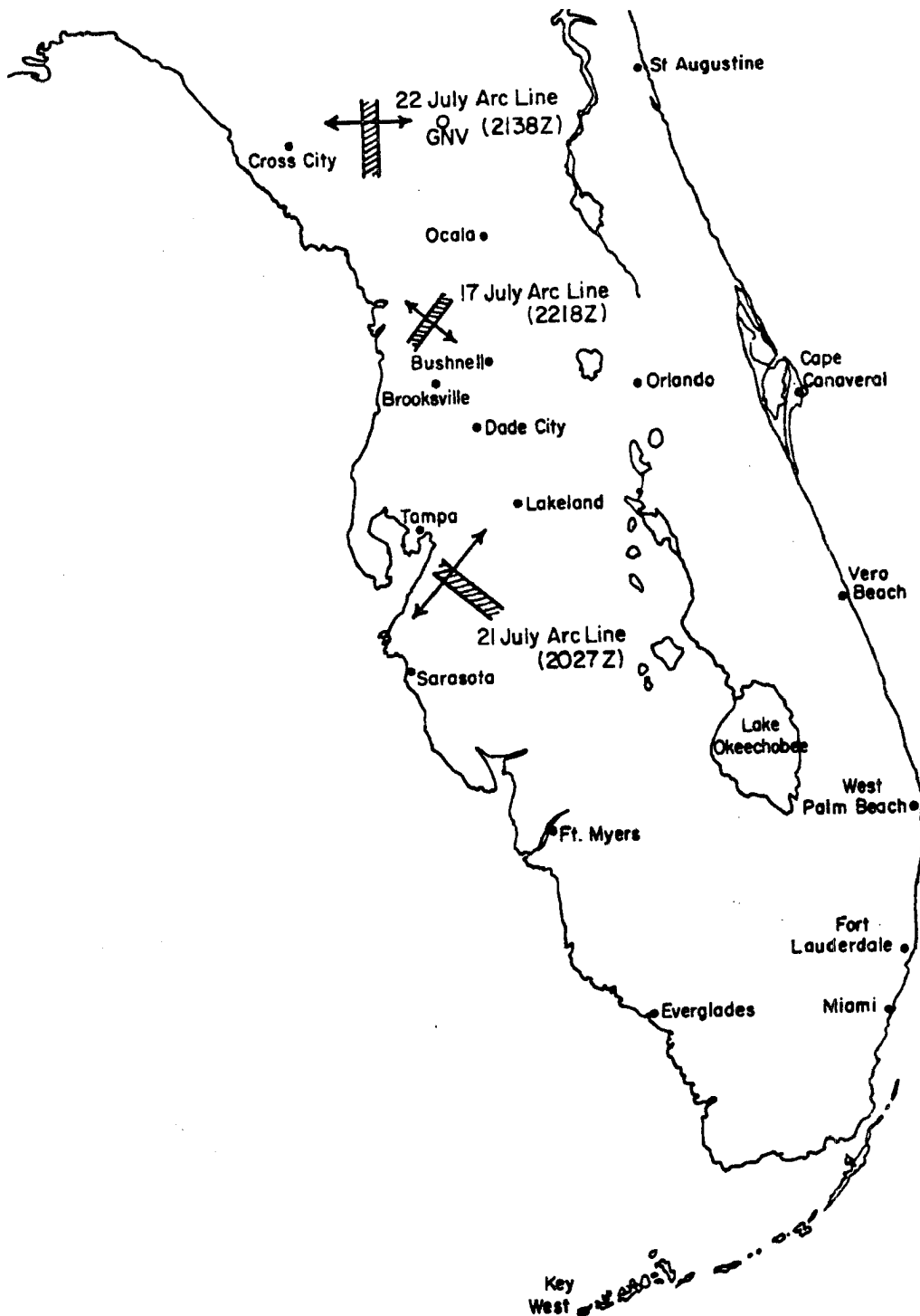
Figure 5.3. Arc cloud line locations. The arc cloud lines are
depicted by the hatched-line areas. The aircraft penetration
directions and the ground tracks are shown by the arrows through the
hatched areas. The mean penetration times are shown below the
penetration dates. From Sinclair and Purdom, 1983.

from 300 to 1000 feet below cloud base. The areas investigated were

Region 3 and the warm air portions of Region 2 as shown in figure 5.2.

5.3.1.1. 21 July 1980, Sarasota area penetrations

The main penetration region of the arc cloud line was located

approximately 46 km northeast of Sarasota, Florida. The width of the

arc line, about 14 km, is shown by the hatched line region in figure

5.3, with the arrow depicting the aircraft path for the 2027 GMT

penetration. Multiple transverses were made of the arc cloud line

region on this day at an altitude of 1037 msl (1000 AGL), which was

approximately 150 m below cloud base.

Figures 5.4a and 5.4b are GOES-East, 1 km resolution visible

images taken near the beginning and ending times of the penetrations

that were made on 21 July. On this day, early shower activity in

central Florida, to the east of Sarasota, produced an arc cloud line

region that moved westward over the area of interest by midday. The

considerable westward displacement of the arc region is due in part to

the strong low-level easterly flow across Florida: notice for example

the long downstream clear area to the west of Lake Okeechobee.

Figure 5.4c* is a mesoscale analysis based on the cloud patterns

shown in figure 5.4a. In figure 5.4c, notice that two areas of

stronger convection are evident along the arc at points A and B.

Additionally a smaller arc, due to earlier convection that had

dissipated, is apparent along the arc between the stronger convection

---

*Nephanalyses of this type are included to show arc locations. Arc
identification from a single photograph is often extremely difficult
and requires movie loop analysis for positive identification. This
nephanalysis, and those that follow, were based on movie loop
interpretations of the 3 minute interval imagery.
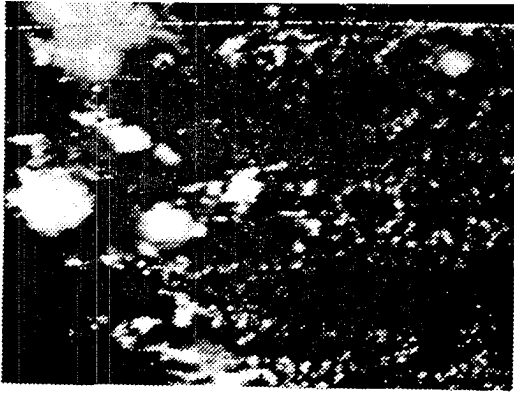
Figure 5.4a. 21 July 1980 at
2030 GMT. GOES-East 1 km
resolution visible image.
Analysis in fig. 5.4c below.
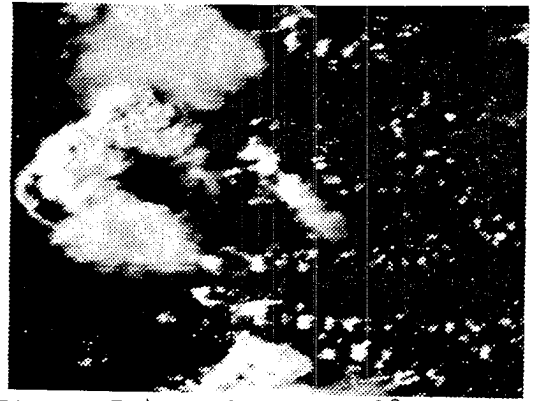
Figure 5.4b. 21 July 1980 at
2144 GMT. GOES-East 1 km
resolution visible image.
Analysis in fig. 5.4d below.
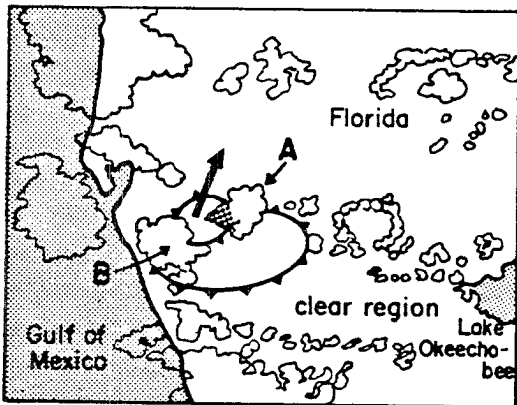
Figure 5.4c. Nephanalysis of
fig. 5.4a. Arrow shows flight
path, shaded area gives view
for fig. 5.4e below.
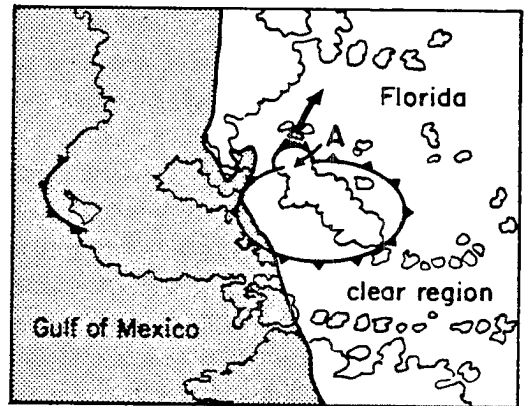
Figure 5.4d. Nephanalysis of
fig. 5.4b. Arrow shows flight
path, shaded area gives view
for fig. 5.4f below.

Figure 5.4e. Photograph of cloud
A (fig. 5.4c) at 2021 GMT prior
to penetration of arc.
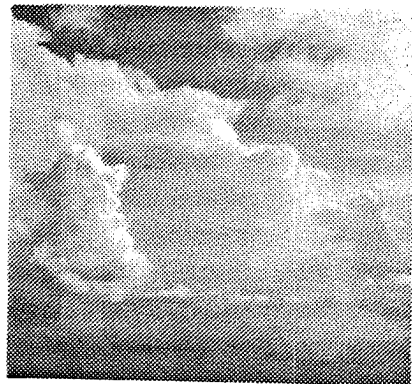
Figure 5.4f. Photograph of cloud
A (fig. 5.4d) taken at 2151 after
final arc penetration.

Plate from Sinclair and Purdom 1983.
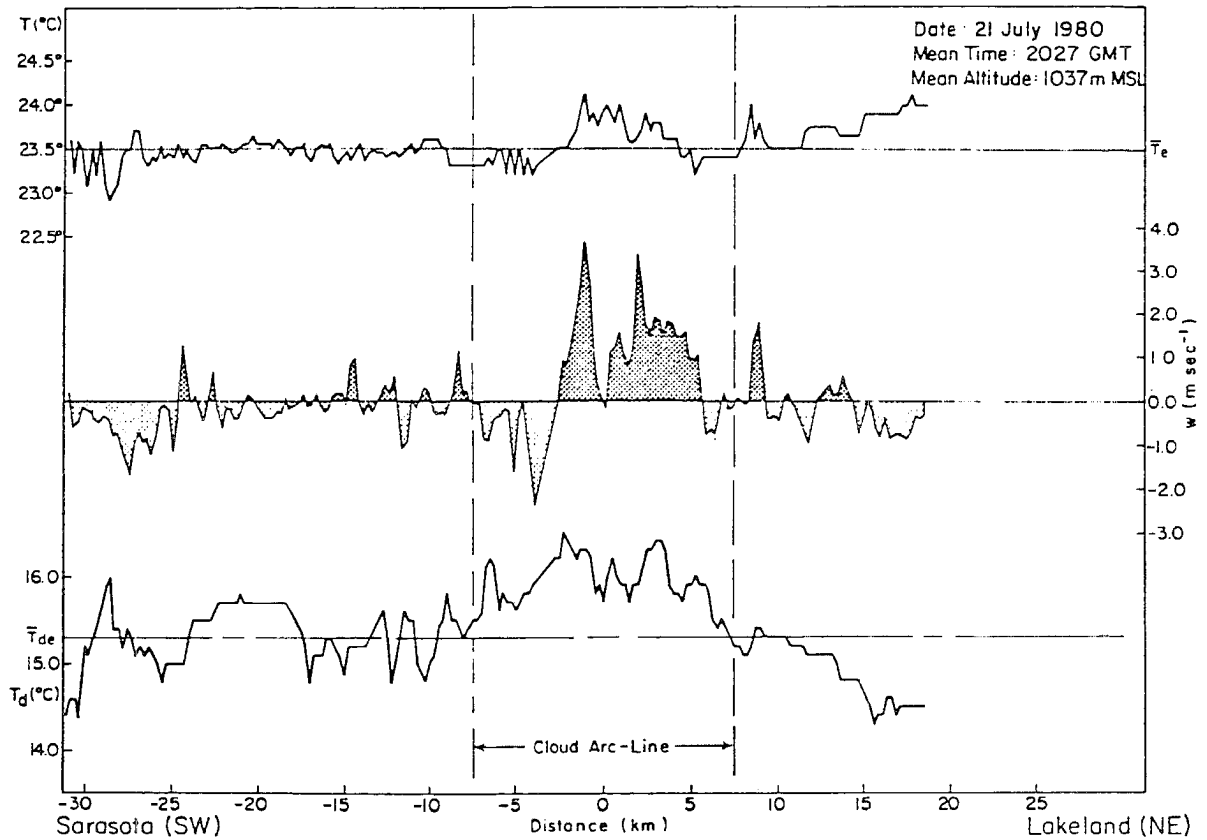
Figure 5.5 Aircraft Data of Arc Line Penetration for 21 July 1980, GMT. The distribution of temperature (T), dew point (T_d), and vertical motion (w) are shown with respect to their mean environmental values: $\bar{T}_e$, $\bar{T}_{de}$, and w = o. The lateral boundaries of the cloud arc line are indicated by the dashed vertical lines at ± 7 km from the arc centerline. From Sinclair and Purdom, 1983.

at A and B. The cloud photograph shown in figure 5.4e is of cloud A in figure 5.4a: notice the rain shower evident beneath that cloud. The replenishment of negatively buoyant air into the boundary layer by showers along the arc cloud line, such as the ones at A and B, as well as the one that produced the small arc between A and B, may be one of the important factors that enables some arc cloud lines to maintain their identity for periods of up to several hours. This point will be addressed in more detail in chapter 6.

Figure 5.4d is a mesoscale analysis based on the cloud patterns shown in figure 5.4b.* This GOES-East image was taken approximately 12 minutes after the final penetration of the day, as was the aircraft photograph shown in figure 5.4f, which was taken looking back to the south at the arc cloud line. An interesting observation, based on analysis of three minute interval GOES images, shows that storm A continued to regenerate along the northern portion of the arc cloud line during the study period. Note the shower activity evident in figure 5.4f. As well as the small line of non-precipitating cumulus ahead of the main shower at A along this northern portion of the arc cloud line. This again suggests the importance of the precipitation/evaporation process to the continuous regeneration of convective clouds along arc cloud lines.

Aircraft measurements from a penetration centered on 2027 GMT, shown in figure 5.5, are typical of those taken on this day. In figure 5.5, the distribution of temperature (T), moisture in the form of dew

---

*An interesting feature shown in this GOES image is the strong thunderstorm activity and the arc cloud line to the west of Sarasota over the Gulf of Mexico. This is not related to storm B, but rather with the thunderstorm that moved off-shore as seen in figure 5.4a.

point temperature (T_d), and vertical motion (w) are shown with respect

to their mean environmental values during the arc cloud line traverse.

The maximum variations of T, T_d and w from their mean environmental

values ($\bar{T}_e$, $\bar{T}_{de}$, $\bar{w}$ = 0) are shown in table 5.2.

The warm, moist core of the updraft region is typical of most arc

cloud line penetrations above the outflow frontal zone (see figure 5.2

for schematic of outflow frontal zone). That air has its origin in the

surface boundary layer ahead of the advancing arc cloud line frontal

zone. Notice that the vertical motion field below cloud base is

strongly positive, while descending motion is also evident on either

side of the main updraft. This descending motion, a type of return

flow circulation, is also a prominent feature along the boundaries of

dry thermals, cumulus clouds, and severe storms (Sinclair, 1973). This

descending sheath of air has its maximum downward values in close

proximity to the updraft core with lower values at larger radii in the

environment. The sharp decrease in updraft vertical motion at the zero

kilometers locations along with a decrease in dewpoint temperature,

points to the possibility of mixing of air from within the DSL with the

warm and unstable air ahead of it. This type mixing is discussed in

more detail in section 5.3.1.2.

In this case, the descending sheath of air around the updraft

appears slightly cooler than the mean environmental temperature ($\bar{T}_e$).

As previously shown, some of the clouds along the arc cloud line had

progressed to the precipitation stage. By the time of the 2027 GMT

penetration, light rain showers were encountered before exiting to the

Table 5.2

Maximum Variations of T, T_d and w for the Arc
Penetrations of 21 July 1980

$$\Delta T_{max} \quad = \quad \pm.6°C$$

$$\Delta T_{d_{max}} \quad = \quad +1.2°C \text{ to } -0.9°C$$

$$\Delta w_{max} \quad = \quad +3.6 \text{ m sec}^{-1} \text{ to } -2.4 \text{ m sec}^{-1}$$

clear zone on the north east side of the arc line. In the precipitation areas the vertical motion was both positive and negative, with evaporative cooling causing the temperature to be slightly below ambient along with an increase in moisture.

5.3.1.2. 22 July 1980 Gainesville region penetration

On this day, shower and thunderstorm activity along Florida's west coast sea breeze front produced an array of arc cloud lines, some of which are detectable in figures 5.6a and 5.6b. The main area of penetration was located approximately 38 km to the west of Gainesville, figure 5.3, with the arc cloud line region shown by the hatched region and the arrow depicting the aircraft path for the penetrations. In order to obtain data at different levels along the arc cloud line, sub-cloud penetrations were made at altitudes of 480 m, 800 m, and 1067 m MSL (terrain elevation in this area is approximately 15-30 m).

Figure 5.6a is a GOES-East, 1 km resolution visible image centered near the time of the arc cloud line penetrations. Figures 5.6c and 5.6d are mesoscale analyses based on the cloud patterns shown in figures 5.6a and b, as well as the evolution of those cloud patterns as revealed in rapid scan GOES imagery. Note the large thunderstorms at A, B and C in figure 5.6b. Those storms developed where arc cloud line #2 intersected three nearby discontinuities, i.e.: (1) arc cloud line #3 producing thunderstorm A; (2) arc cloud line #1 producing thunderstorm C; and, (3) the convective region to its north producing thunderstorm B. Penetration activity was confined to the eastern portion of arc cloud line #2. This arc cloud line was the youngest and most vigorous of those penetrated during the 1980 experimental days.
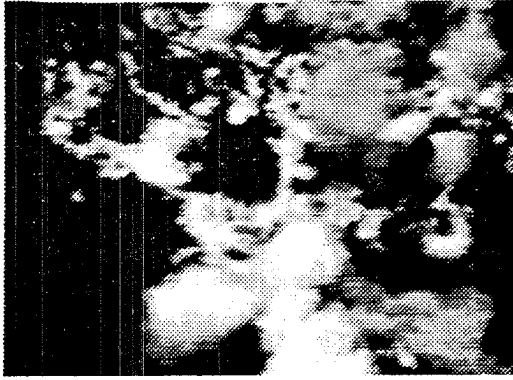
Figure 5.6a. 22 July 1980
at 2030 GMT. GOES-East 1 km
resolution visible image.
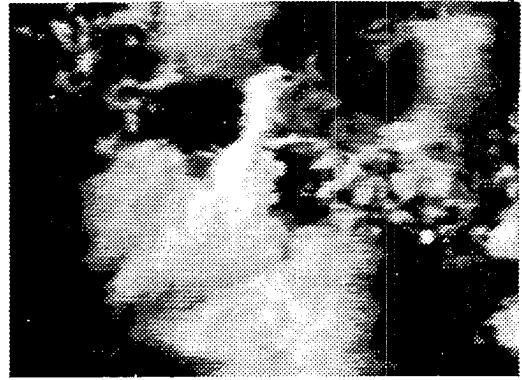
Figure 5.6b. 22 July 1980 at
2144 GMT. GOES-East 1 km
resolution visible image.
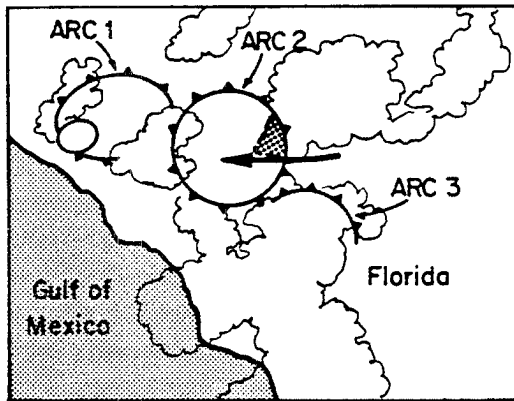
Figure 5.6c. Nephanalysis of
fig. 5.6a. Arrow shows flight
path, shaded area gives field
of view for montage in fig. 5.6e.
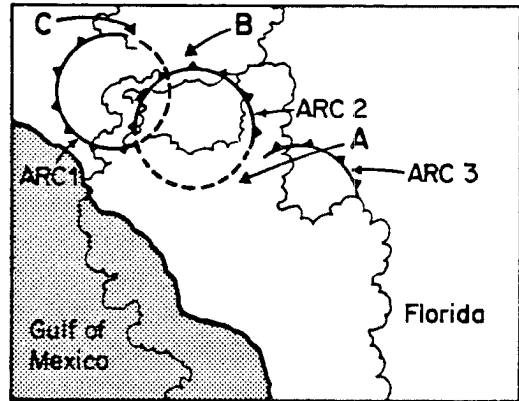
Figure 5.6d. Nephanalysis of
fig. 5.6b. Note the large thunder-
storms that have formed due to
arc 2's various interactions
(see text).
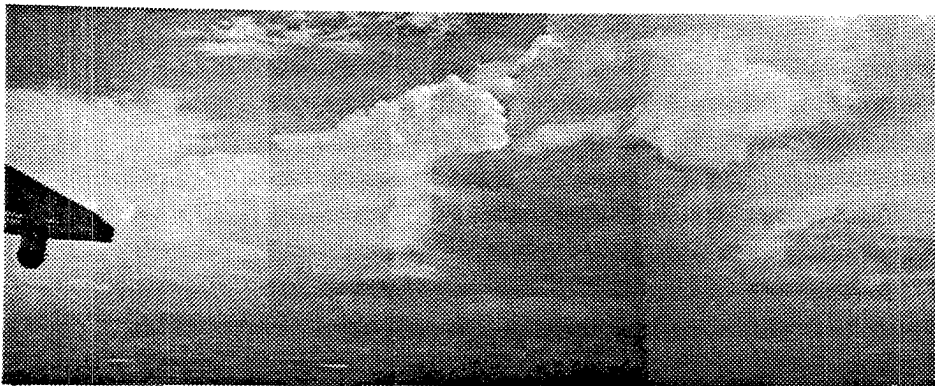
Figure 5.6e. Montage of arc cloud region, taken from its interior
after the initial penetration. See figure. 5.6c.

Plate from Sinclair and Purdom, 1983.

The montage in figure 5.6e shows the congestus along the eastern side of the arc cloud line: notice the clearer skies above as well as the shower activity along the arc cloud line. The importance of shower activity in the production of negatively buoyant air in the sub-cloud region was mentioned in the discussion of the previous case (21 July).

At all three levels of penetration, the region above the surface outflow boundary was characterized by a warm updraft core extending to cloud base at 1250 m. The measurement profiles of T, T_d and w are shown in figure 5.7. Within the updraft region, the maximum variations of T, T_d and w were similar to those for the 21 July case. Important features of these multiple level, arc line penetrations are summarized below (refer to figure 5.7 and table 5.3).

(1) A pronounced warm updraft region is evident below the arc cloud line at all levels (480-1067 m MSL). Both $\overline{\Delta T}$ and ΔT_{max} indicate a temperature excess range of approximately 0.5°C to 2.0°C. Mixing of cooler neutrally stable environmental air into the arc line updraft region (which in this case appears to originate from a superadiabatic surface layer) is in part responsible for the $\gamma_p > \gamma_{dry}$ and the decrease of $\overline{\Delta T}$ and ΔT_{max} with height. The ratio of environmental air to updraft air (by mass percent) involved in this mixing varies from approximately 12% (480 m - 800 m) to 67% (800 m - 1067 m). Greater mixing in the 800 m - 1067 m layer is required to account for the close approach of the updraft mean mixture temperature ($\overline{T}_m$) to the mean temperature of the environment ($\overline{T}_e$). The mixing calculation is based
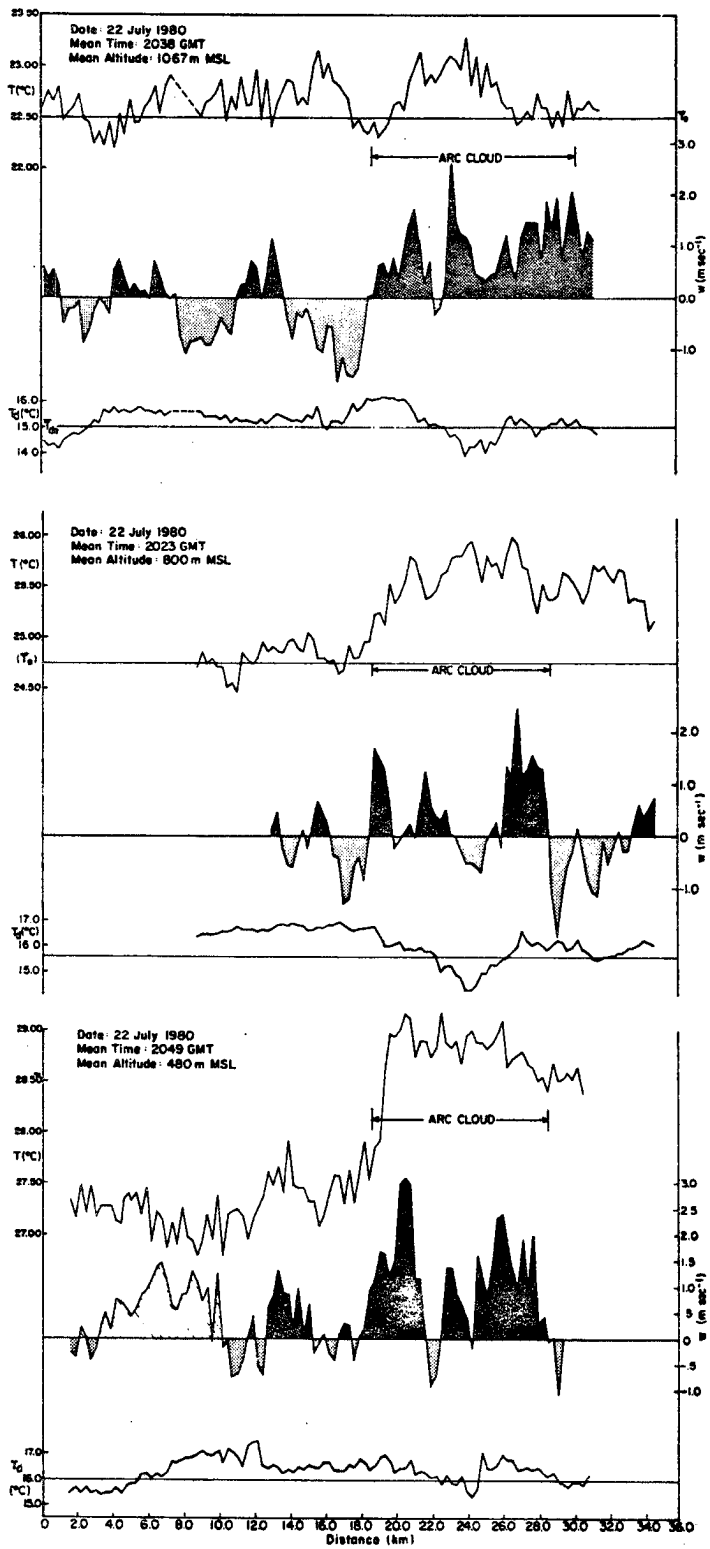
Figure 5.7. Aircraft data of arc line penetrations for 22 July 1980, 2023-2049 GMT. See figure 5.5 for further explanation.

Table 5.3

Arc-line Penetration Parameter Values for the Arc of 22 July 1980
From Sinclair and Purdom, 1983.

z (m)	$\bar{T}$ (°C)	$\bar{\Delta T}$ (°C)	ΔT_{max} (°C)	γ_p °C/100m	$\bar{T}_d$ (°C)	$\bar{\Delta T}_d$ (°C)	$\Delta T_{d_{max}}$ (°C)	Δw (msec^{-1})
480	28.8	1.6	1.9		16.4	0.4	-0.7	3.1
				1.00				
800	25.6	0.9	1.3		15.8	0.2	-1.3	2.4
				1.05				
1067	22.8	0.3	0.6		15.3	0.3	-1.1	2.6

In table 5.3 the various parameters have the following meanings:

z   altitude (MSL)

$\bar{T}$ updraft mean temperature

$\bar{\Delta T}$ $\bar{T} - \bar{T}_e$ ($\bar{T}_e$ = mean environmental temperature)

ΔT_{max} $T_{max} - \bar{T}_e$ (T_{max} = maximum updraft temperature)

γ_p process lapse rate

$\bar{T}_d$ updraft mean dew point

$\bar{\Delta T}_d$ $\bar{T}_d - \bar{T}_{de}$ (T_{de} = mean environmental dew point)

$\Delta T_{d_{max}}$ $T_{d_{min}} - \bar{T}_{de}$ ($\bar{T}_{d_{min}}$ = updraft minimum dew point)

Δw updraft maximum velocity excess.

on a calorimetric mixture of the (mean) updraft and environmental air

for a "sawtooth" approximation* to the process lapse rate (γ_p), the

mean heat content of the mixture ($M_m Cp_m \bar{T}_m$) is equal to the mean heat

content of the updraft air below the mixing level ($M_u CP_u \bar{T}_u$) and the

environmental air ($M_e Cp_e \bar{T}_e$) mixed into the updraft air:

$$M_m Cp_m \bar{T}_m = M_e Cp_e \bar{T}_e + M_u Cp_u \bar{T}_u, \qquad (5.0)$$

where $\bar{T}_e$ = mean environmental temperature, $\bar{T}_u$ = mean updraft

temperature and M_m, M_e and M_u are the mean mixture, environmental and

updraft air masses respectively. Since specific heats (Cp_m, Cp_e, Cp_u)

are essentially equivalent here, the mean mixing ratio of the

environmental air to the updraft air is given by:

$$\frac{M_e}{M_u} = \frac{T_u - \bar{T}_m}{\bar{T}_m - \bar{T}_e} \qquad (5.1)$$

(2) The peak updraft velocity, like the temperature excess, shows a

general decrease in magnitude with height. Thus as the buoyancy

driving force decreases with altitude, the vertical motion field

follows in step.

---

*A sawtooth approximation involves a dry adiabatic ascent of the
updraft air over a small vertical distance such that the mixing of mean
updraft quantities with its environment takes place at the end of each
adiabitic increment. The end points of a series of these sawtooth
approximations describe the process lapse rate (γ_p).

(3) Descending motion around the main updraft region is apparent only at the upper penetration level, approximately 150 m below cloud base. Here a somewhat warmer recirculating downward flow near the cloud lateral boundaries is apparent at the forward edge of the arc cloud line where the vertical velocities decrease to $w = -1.5$ msec^{-1}. At the lower levels, this recirculating flow is not so apparent.

(4) At the 480 m penetration level, the vertical motion, temperature and moisture measurements suggest negatively buoyant thermals in the interval 14 to 21 km ahead of the arc cloud line main updraft (cross-hatched w profile). These cool ($\Delta T = -0.5$°C), moist upward thrusts of surface boundary layer air represent the tops of overshooting thermals that because of their size and organization have been sufficiently mixed with the environment to reach a density equilibrium level below 480 m.

(5) An intriguing feature of these arc line measurements is shown by the moisture distribution in the updraft region at all three levels. In all cases, the dew points decrease dramatically as the center of the updraft is approached. The maximum dew point deficiencies

$(\Delta T_{d_{max}} = \bar{T}_{de_{min}} - \bar{T}_d)$ for each penetration are shown in table 5.3.

This somewhat drier air is flanked by moist air that has risen from lower levels in the marine boundary layer ahead of the arc line outflow. The most plausible source of the drier air is the relatively cool, dry outflow air with the warm, moist marine air ahead of the outflow DSL. Such mixing has been observed in laboratory tank experiments of gravity currents (Simpson, 1969), see figure 5.15.

5.3.1.3. 17 July 1980 - Bushnell region penetrations

In this particular case, the arc cloud line investigated was nearly 6 hours old and had a weak, rather ill-defined high cloud base on its northern boundary. The arc line was penetrated at an altitude of 1070 m in a northwest to southeast direction north of Tampa, near the Town of Bushnell, Florida (see figure 5.3).

Figures 5.8a and 5.8b are GOES-East, 1 km resolution visible images taken 1 1/2 hours apart. The arc cloud line shown in those figures moved slowly northward from thunderstorm activity near the Tampa Bay area. The region of the arc cloud line penetrated by the aircraft is shown in figure 5.8d, which is a mesoanalysis based on the cloud field shown in figure 5.8b. Notice how the amount of convection decreases along the arc during the 1 1/2 hour period and that no thunderstorms formed along the arc as it moved northward, although shower activity was observed during the penetration close to the location where the arc cloud line intersected the sea breeze front.

In figure 5.9, the vertical velocity (w) and dew point (T_d) measurements show the typical moist updraft region below cloud (arc line) base. The maximum updraft variations $[\Delta(\ )_{max}]$ of T, T_d, w are shown in table 5.4. The typical descending motion on either side of the main updraft is generally warmer and drier than the updraft air which itself is actually cooler and more moist than the environmental air at least 20 km from the updraft core. The relatively cool updraft core is interpreted as air that has overshot its equilibrium level and as a consequence appears cooler than its environment. This phenomena should take place when either the outflow weakens, the density surge
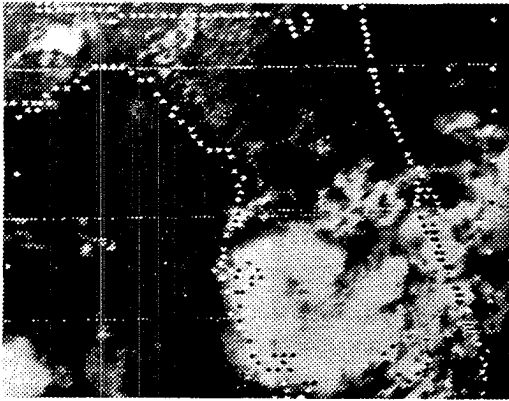
Figure 5.8a. 17 July 1980 at 2100 GMT. GOES-East 1 km resolution visible image.
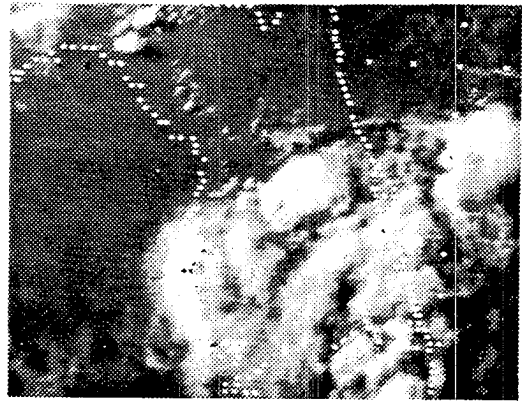
Figure 5.8b. 17 July 1980 at 2230 GMT. GOES-East 1 km resolution visible image.
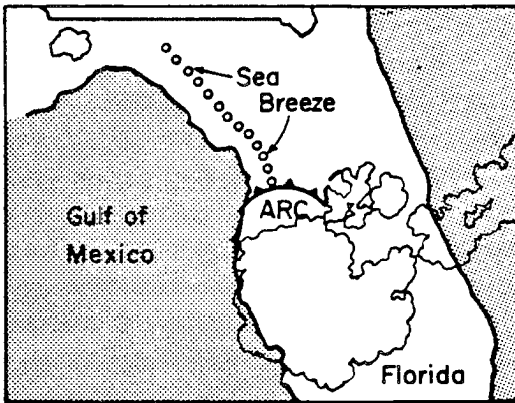
Figure 5.8c. Nephanalysis of fig. 5.8a.
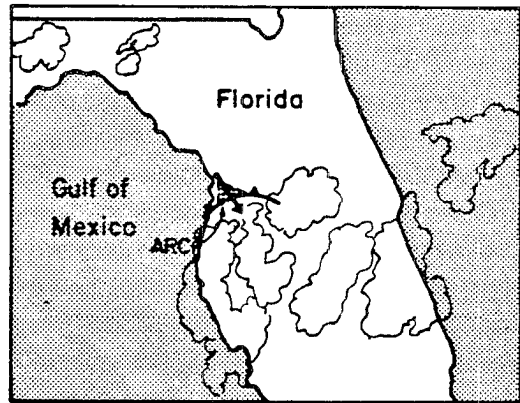
Figure 5.8d. Nephanalysis of fig. 5.8b. Arrow shows flight path, shaded area gives field of view for montage in fig. 5.8e.
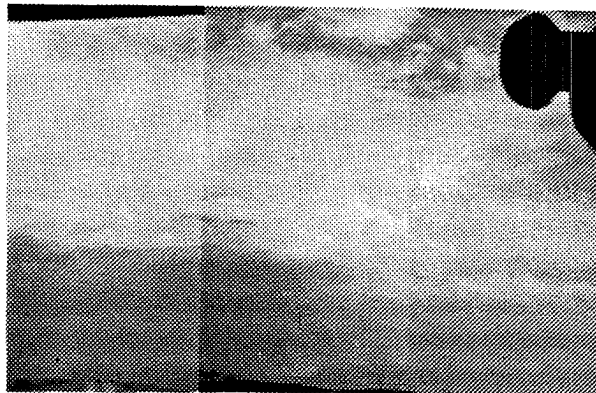
Figure 5.8e. Montage of arc cloud region prior to penetration; note weak cumulus development.

Plate from Sinclair and Purdom, 1983.
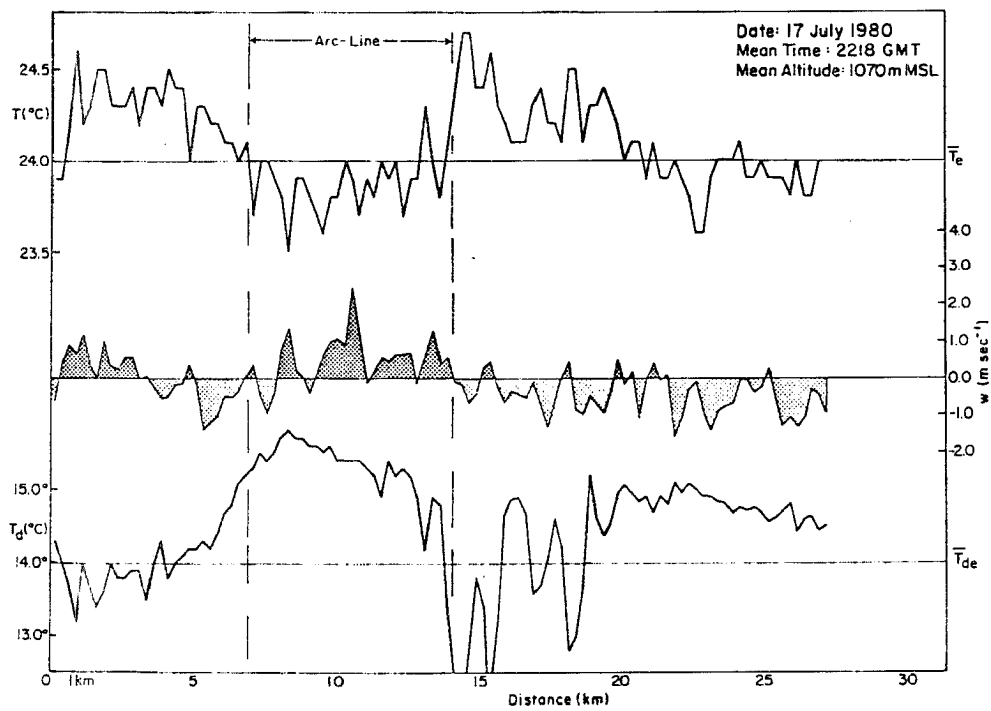
Figure 5.9 Aircraft data of arc line penetration for 17 July 1980, 2218 GMT. See figure 5.5 for further explanation. From Sinclair and Purdom, 1983.

Table 5.4

Maximum Variations of T, T_d and w for the Arc
Penetrations of 17 July 1980

ΔT_{max} = +0.7°C to -5°C

$\Delta T_{d_{max}}$ = ±2.0°C

Δw_{max} = +2.5 m sec⁻¹ to -1.5 m sec⁻¹

line becomes stationary and well-mixed, and/or as the outflow advances into an airmass with marginal instability.

5.3.2. Colorado (Summer 1982)

The arc cloud line investigations in the Colorado high plains were carried out in late July and early August of 1982. The main purpose of those investigations was to establish similarities and differences between arc cloud lines in the more moist southeast United States and those that are generated over the more arid high plains.

General areas for penetrations were chosen using near real time GOES satellite data from the CSU IRIS system (Green and Kruidenier, 1982). Once the aircraft reached an area for investigation, decisions concerning penetration points were made visually. Five research flights were accomplished on five separate days during July-August, 1982. Cloud arc-lines were apparent on each of these flight days, although most were of insufficient strength to warrant detailed aircraft measurements. On 12 August, however, a strong thunderstorm developed near Akron, Colorado between 2300-2400 GMT. Multiple transverses were made of the developing arc region above the density surge line on this day. Penetration altitudes varied from 10,500 ft MSL (6500 ft AGL) down to 8500 ft MSL (4000 ft AGL). Cloud base of the arc-line was at approximately 12,000 ft MSL. The areas investigated were Region 3 and the warm air portions of Region 2 as shown in figure 5.2.

5.3.2.1. 12 August 1982

In the 1980 Florida arc cloud line penetrations, the Density Surge Line (DSL) was relatively far removed from the parent storm cell. In this particular case, the aircraft measurements were made during the

early development stage of the arc cloud line - a part of the life

cycle not documented previously. Specifically, the arc cloud line was

developing very close to the storm downwind outflow boundary. As a

result, the developing arc cloud line was obscured from satellite

viewing by a large cirrus anvil overhang.

The aircraft measurements along various penetration tracks

centered in essentially two locations. The first two penetrations were

made only a few miles (nm) north of the surface outflow core. Two

representative penetrations are shown in figure 5.10. The distribution

of temperature (T), moisture in the form of dew point temperature (T_d),

and vertical motion (w) are shown with respect to their mean

environmental values during the transverse just below the arc cloud

line. Several important features of these penetrations are worth

noting:

1) A very weak updraft (UD) is present just below the arc cloud
line: $w \approx +0.1$ to 1.0 m sec^{-1}.

2) The relatively warm updraft (referenced to the environment out
ahead of the arc cloud line) indicates ΔT's $\approx 0.1°C$ to $0.7°C$.
Note, these ΔT,s may be positive or negative with respect to the
Cloud Gap (CG) region (figure 5.12).

3) The UD region is always more moist than its surroundings.

4) The CG air is as warm or warmer than the UD air,
$\Delta T \approx +0.1°C$ to $+0.3°C$.

5) The CG air is generally descending, $w \approx -0.1$ to -0.7 m sec^{-1},
with respect to the updraft and the downwind environment.

6) The CG air is generally drier than the UD, $\Delta T_d \approx -0.1°C$ to
$0.8°C$.

Because of the weak updraft features (T, T_d, w) encountered on

these first penetrations and the intensification (visual) of the storm
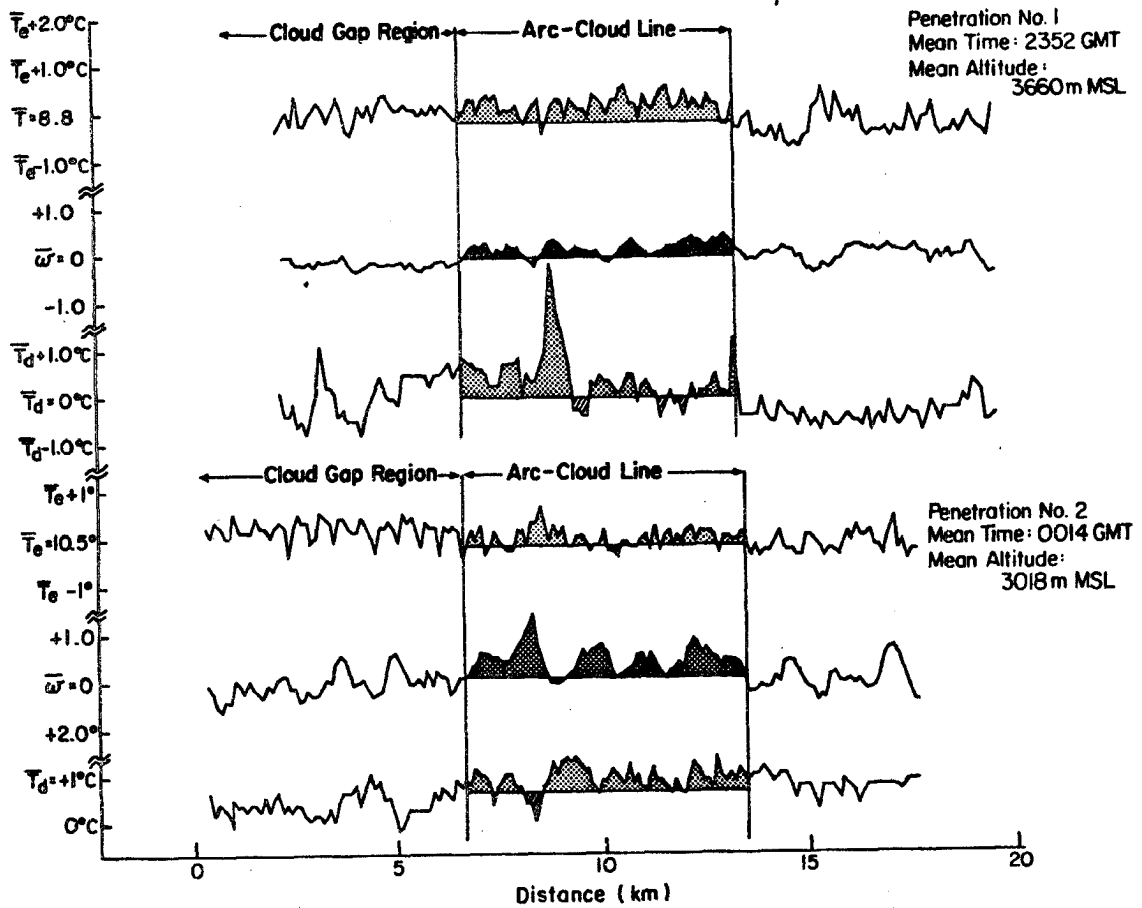
Figure 5.10. Aircraft data of arc cloud line penetrations #1 and #2
for 12 August 1982. The distribution of temperature (T), dewpoint
(T_d), and vertical motion (w) are shown with respect to their mean
environmental values (Note reference lines). The lateral boundaries of
the arc cloud line are indicated by the solid vertical lines. From
Sinclair and Purdom, 1984. Values of T and T_d are in °C, and values
for w are in m sec^{-1}. To convert time to CST, subtract 6 hours from
GMT.

outflow boundaries, the aircraft penetrations were displaced southward

approximately 8 nm in order to be more aligned with the outflow

boundaries at the surface. The results of two penetrations below the

arc cloud line in this area are shown in figure 5.11. In that figure,

penetration #4 was nearly aligned with the outflow core near the

surface, while penetration #3 is several km to its north. Several

features of these measurements differ from those of penetrations #1 and

#2.

1) The UD vertical motion field is much more distinct and larger
   in value, w_{max} = +10.1 m sec^{-1} (Pent. #4).

2) In general, descending motion is found along the updraft
   flanks, $\bar{w}$ ≈ -0.5 to -1.5 m sec^{-1}.

3) The CG air is descending and is both much cooler (ΔT ≈ -1.8°C)
   and more moist (ΔT_d ≈ 0.1°C to 1.2°C) than the UD air.

4) All penetrations indicate that the thermal buoyancy is
   relatively low and not distinct, ΔT ≈ 0.1°C TO 0.7°C.

5) In both penetrations #3 and #4 there is a significant cool,
   moist downdraft of CG air along the updraft flank.

6) In both penetrations #3 and #4, there is significant
   negatively buoyant air within the rear portion of the updraft.

These later points (5) and (6) indicate that the cool, moist descending

air of the CG region is either due to dynamic recirculation along the

updraft flanks (sheath flow) and/or driven by cooling of the CG air by

cloud water evaporation from both the arc cloud line and the parent

storm. Furthermore, the cool, moist air in the rear of the main

updraft appears to lead to a decrease of the updraft's intensity. This

feature and the fact that the thermal buoyancy is in general weak and

not distinct, suggests that the UD (in this early stage) is driven and

maintained primarily by the initial momentum generated near the surface
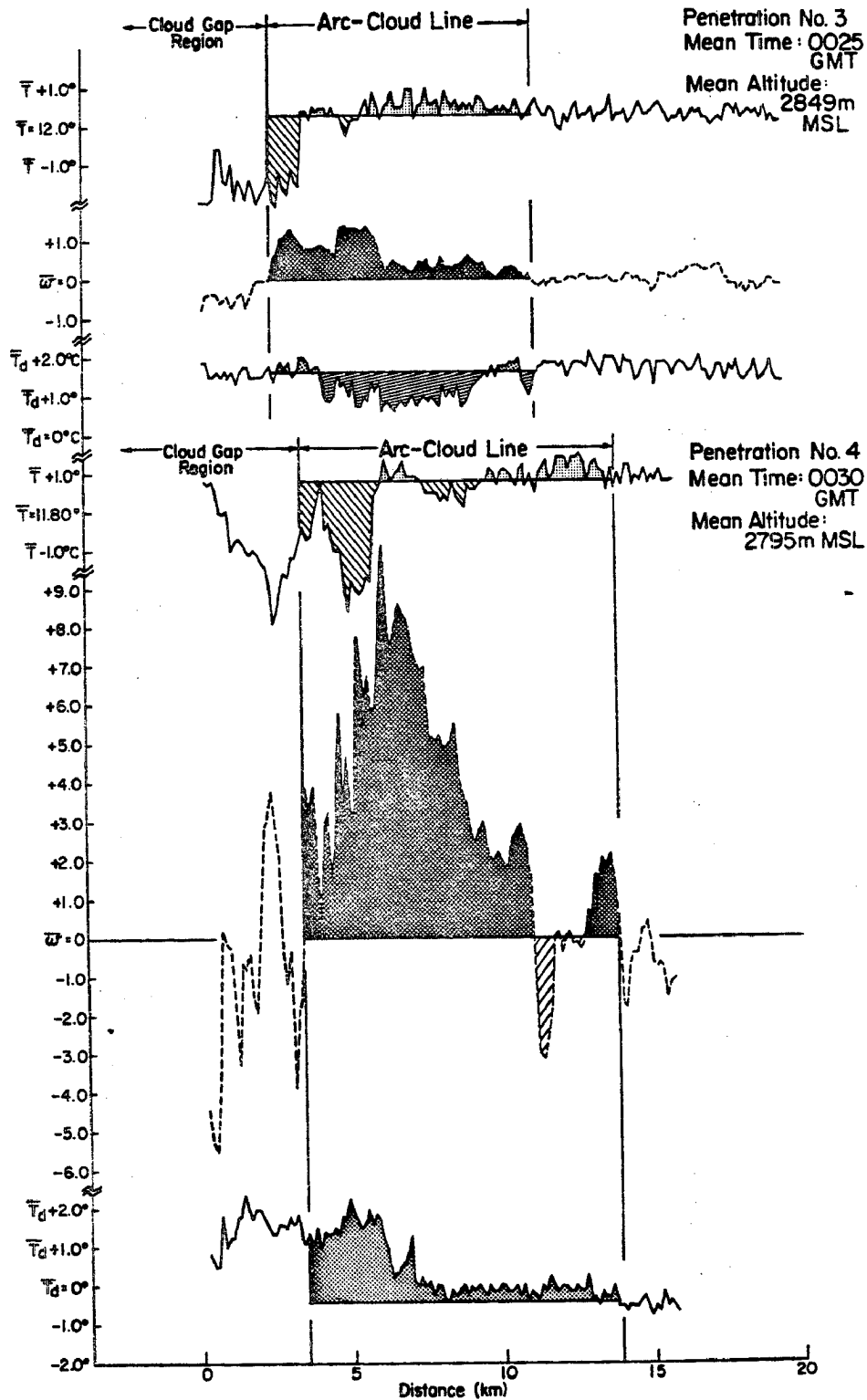
Figure 5.11. Aircraft data of arc cloud line penetrations #3 and #4 for 12 August 1982. From Sinclair and Purdom, 1984. Values of T and T_d are in °C, and values for w are in m sec^{-1}. To convert time to CST, subtract 6 hours from GMT.

interface of the DSL and that there is strong mixing of DSL and cloud

gap air into the rear portion of the arc cloud line updraft region.

These measurements along with visual observations are illustrated

schematically in figure 5.12 to depict the early development of the arc

cloud line above the storm outflow boundary (DSL). The initial

horizontal momentum of the inflow air as it is lifted over the DSL

interface provides the main driving force for the development of a

continuous updraft to cloud base. It appears that strong mixing zones

exists on the UD flank near the cool, moist descending air of the CG

and along the DSL interface. The mixing of environmental air (air

downstream of the arc cloud line) into the UD does not produce the same

kind of modification of the UD as that experienced adjacent to and

below the CG region. This may be due to the well-mixed character of

the PBL and surface layer ahead of the arc cloud line, as well as

mixing of DSL air into the rear portion of the arc cloud line's UD.

5.3.3. Florida (Summer 1983)

The arc cloud line investigations in Florida were carried out

during the last two weeks of August, 1983. The main purpose of those

investigations was to determine the dynamic and thermodynamic

characteristics of the DSL region; region 1 and region 2 of figure 5.2.

Arc cloud lines of varying intensity were investigated on each of the

five flight days. Penetrations were made in the clear air, well below

cloud base and in the DSL. Generally, multiple traverses were made

through the DSL at altitudes ranging from 120 m to 650 m.

General areas of penetration were chosen using near real time GOES

satellite data that were transmitted over closed circuit TV from

Cape Canaveral AFS to Patrick AFB Operations. Once the aircraft
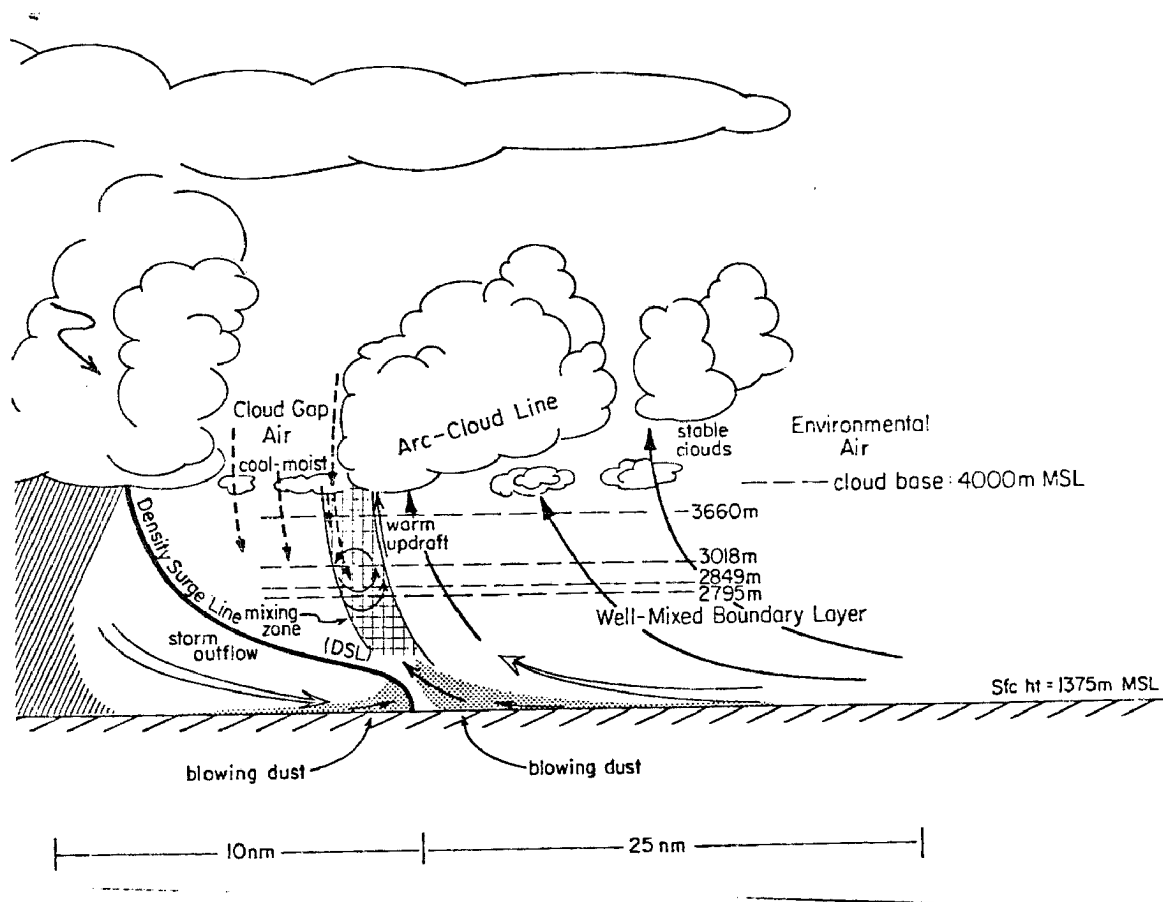
Figure 5.12. Schematic illustration of arc cloud line features during early development. From Sinclair and Purdom, 1984.

reached in area where arc activity had been detected, decisions concerning penetration points were made visually.

5.3.3.1. August 1983

In Florida, several research flights were made on five flight days, with arc cloud line' DSL's of varying intensity encountered on each day. Among the more interesting of the research days was the last flight in August when an arc cloud line region was studied near the northwest coast of Florida, approximately 45 nm SE of Tallahassee. The storm outflow penetrated into the moist boundary layer environment formed by the easterly onshore flow of the sea-breeze front. The circulations encountered on this day are representative of those active arcs penetrated on other flight days; consequently only this case will be discussed. Penetrations within the DSL were made between approximately 180 m and 500 m (AGL). The drawing shown in figure 5.13 summarizes the results of the penetrations, which are presented in a coordinate system relative to the DSL boundary. At different levels, the wind shift between the DSL and the warm unstable airmass into which it was moving was between 9 and 15 m sec^{-1}. Ahead of the DSL, vertical motion was weak and somewhat unorganized. However, it became organized into an upward moving current of warm moist air as it moved into the region of the DSL. At, and on both sides of the DSL interface, vertical motions increased sharply and the air became turbulent. Solid upward motion, with peaks as high as 5-10 m sec^{-1} were found in this interface region. In the outflow air, between approximately 2-3 km behind the DSL interface a sharp transition zone was found between upward moving air and sharply descending air. Vertical motions in the

sinking air ranged from -1 to -3 m sec⁻¹. This downward motion

gradually diminished with deeper penetration into the cool air. The

entire flight within the DSL and rain cooled air was turbulent. When

flying in the rain-cooled air toward the DSL interface, an effective

tail wind of 12 to 18 m sec⁻¹ was present. During the entire time of

the penetrations there was little nearby precipitation or virga.

Estimates placed the storm visible precipitation shaft at least 5-10 km

away from the turn point (cool air side).

The most important feature of this outflow case is the

documentation of the previously suspected solenoidal circulation just

inside the DSL interface. The solenoidal circulation is the result of

the baroclinicity that exists across the arc-line front and may

provide a significant part of the energy for the updraft region within

the cold air just behind the frontal surface. Similar arguments have

been used Goff, 1976; and Mitchell and Hovermale (1977) to explain

solenoidal circulations along the leading edges of severe gust fronts.

5.4. Summary of Aircraft Observations

Based on the aircraft observations, the following information

concerning the three regions of the arc line shown in figure 5.2 may be

surmised:

A) Region 1 (cool outflow, refer to figure 5.13):

1. Subsidence was found at all levels below cloud base, once

penetrations were a few kilometers within the DSL or the

region above it. Subsidence is stronger in the DSL than the

air above it. This suggests that while the cooler air within
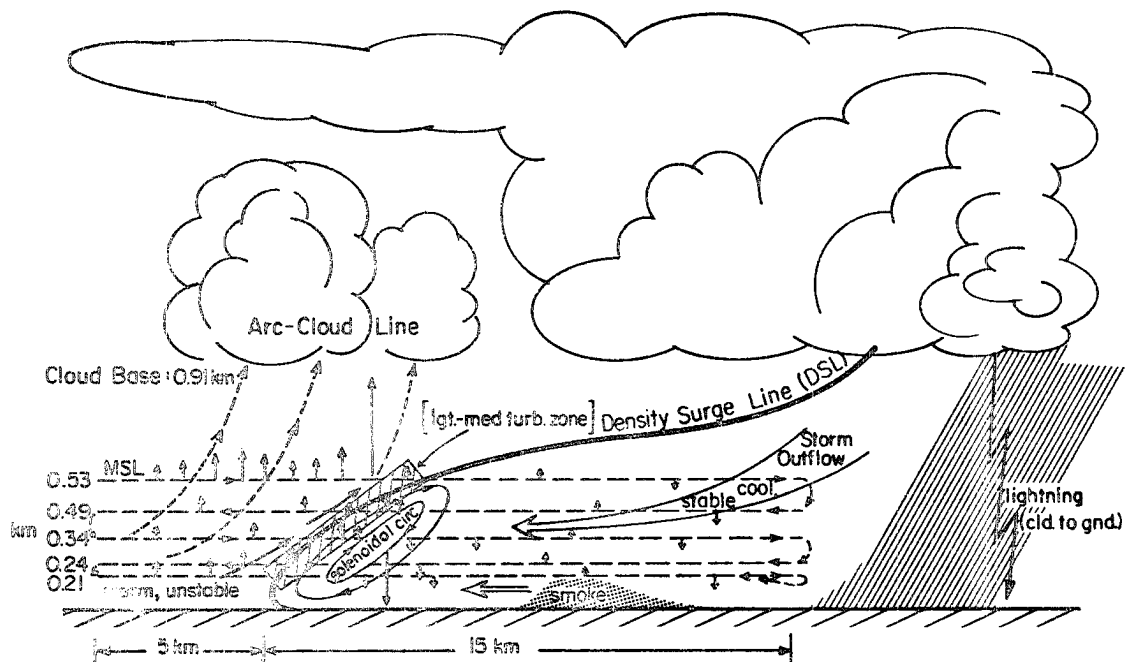
Figure 5.13. Schematic illustration of arc cloud line solenoidal circulation. The arc cloud line is formed above the leading edge of the density surge line (DSL). The vertical velocity arrows represent actual measurements with an absolute value of 2 m sec^{-1} for an arrow length of (ϕ). From Sinclair and Purdom, 1984.

the DSL is sinking in an attempt to restore hydrostatic equilibrium with the surrounding environment, the air above the DSL descends due to continuity consideration. This leads to a more stable cloud form (debris) above the DSL, and if sinking is sufficiently vigorous the result above the DSL is a clearing of the skies.

2. The strong tailwind within the cold outflow air was only experienced within the vertical extent of the DSL and not above it. This cold outflow leads to strong convergence at the DSL and undisturbed environment interface.

3. Precipitation along the outflow arc contributes to negatively buoyant air within the outflow boundary. This precipitation from relatively small convective elements may be one of the important factors that allows the arc to maintain its identity for several hours in the absence of strong thunderstorm activity.

B) Region 2 (interface region, refer to figure 5.14):

1. A solenoidal circulation exists within the DSL. This result is due to the baroclinicity across the arc-line front, accounting for the updraft region within the cold air just behind the frontal DSL surface.

2. The lifting of the warm environmental air by the cold outflow air gives rise to a significant vertical motion field just ahead of the arc-line gust front.
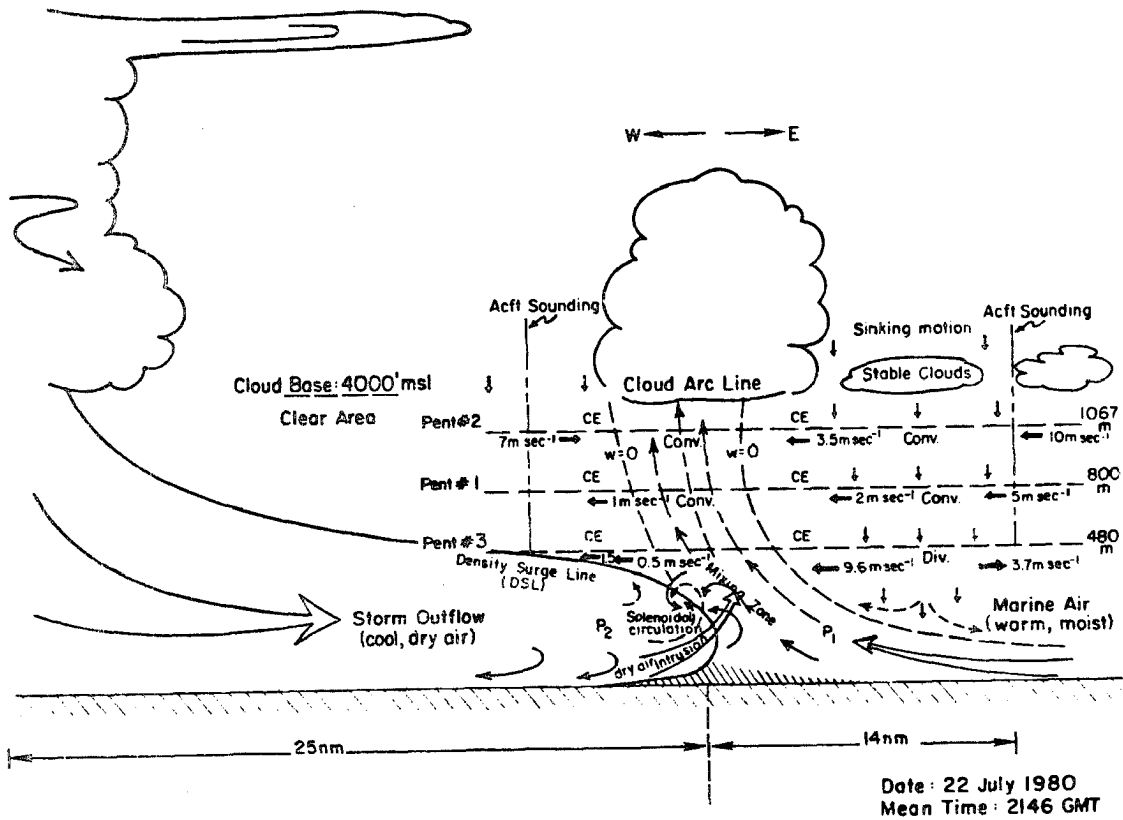
Figure 5.14. Schematic illustration of the cloud arc line features. The cloud arc line is formed above the leading edge of the density surge line (DSL). The environmental flow field provides a net convergence around the main updraft region. From Sinclair and Purdom, 1983.

3. There were cases where both positively and negatively

buoyant thermals were encountered in the air ahead of the arc

cloud line. In addition to the lifting of the environment by

the arc line front, there is also the interaction of the

vertical motion field from buoyancy forces ahead of the

outflow front that lead to organized convective development.

C) Region 3 (arc line cloud base region, refer to figure 5.14:

1. Except in the late stages of the DSL's life, a strong warm

moist updraft core exists beneath the arc cloud line.

Descending motion is evident around the main updraft region.

2. The strong turbulence and shear in the vertical wind

across the DSL interface is due to mixing of air from within

the DSL with the warm unstable air ahead of it. This

contributes to a modified updraft structure that feeds the

cumulus clouds of the arc cloud line. This type mixing has

also been observed using laboratory tank models of density

flows, see figure 5.15a and 5.15b.

3. Ahead of the DSL, mixing of environmental air into the

updraft region also contributes to a modified updraft

structure feeding the cumulus clouds along the arc cloud line.

Other important differences exist between the air and flow fields

in the DSL and in the sub-cloud layer above the DSL. Comparison of

figure 5.14 with figure 5.13 gives some indication of the differences

in the kinematic-dynamic characteristics of air within and above the
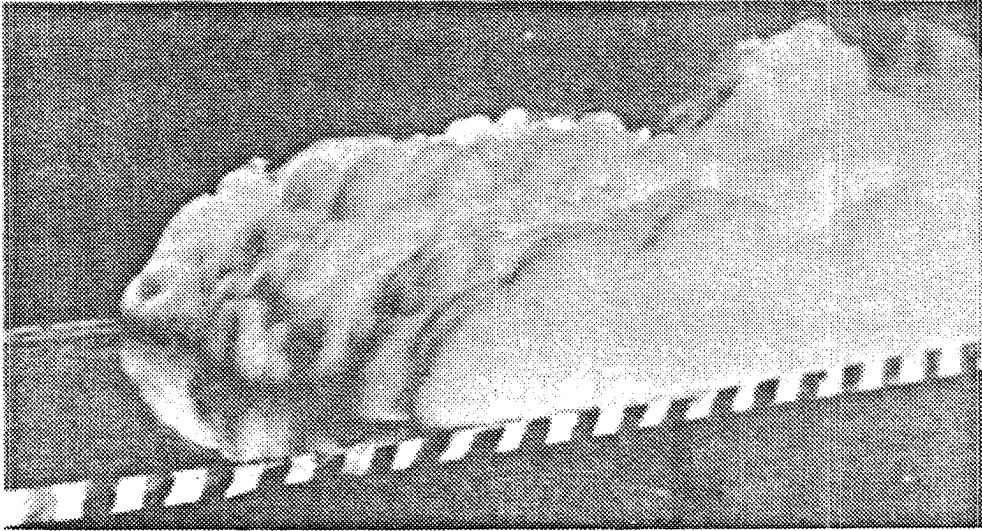
Figure 5.15a. A saline solution (moving right to left) of a laboratory tank experiment (Simpson 1969) shows the similar cleft and lobe structure observed in several gravity type current flows in the atmosphere.
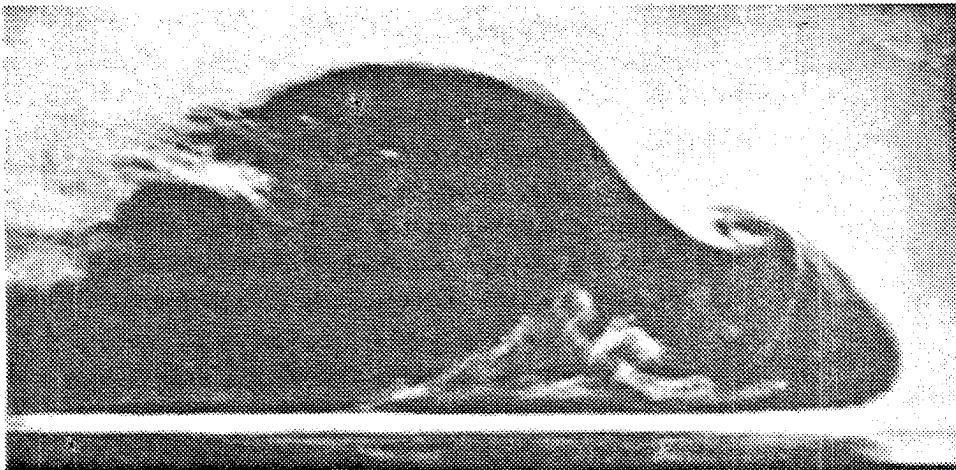
Figure 5.15b. Patches of lighter fluid trapped below the dark, advancing laboratory gravity current are mixed into the base of the head then swept toward the nose of the outflow (moving to the right) (Simpson, 1972).

DSL. Air motions within the DSL appear to be much more turbulent, as well as being stronger in both upward and downward motions, than those encountered in the sub-cloud layer ahead of and above the DSL.

The lateral extent of the vertical motion field compared to the cloud scale indicates that the main driving force for the initial cloud development along the arc cloud line is controlled by the thunderstorm outflow(s) interacting with the convectively unstable air of the environment. The individual cumulus cloud scale motions along the arc-arc cloud line can then be visualized as being superimposed on this somewhat larger-scale, initiating process. Furthermore, this initiating process appears to be sufficient in nature to control the maintenance of the updraft region above the DSL to cloud base strictly on the initial momentum field generated near the outflow interface. That is, the buoyancy field appears to act as a secondary energy source for the initiation of the updraft region below the arc cloud line. This conclusion is probably more valid during the formative stages of the outflow's development than during the later stages of the arc cloud line's life cycle.

In the next chapter, a physical model of the arc cloud line and the process of convective scale interaction will be presented. This physical model will rely on the aircraft and satellite observations of this and the previous chapters.

6.0 ARC CLOUD LINES AND CONVECTIVE SCALE INTERACTION

In the previous chapters, high resolution satellite imagery along
with other types of meteorological data have been used to define and
illustrate the arc cloud line phenomena and the concept of convective
scale interaction. It has been shown that, in a convective atmosphere
typified by weak synoptic scale forcing, that convective scale
interaction is of fundamental importance in controlling the development
and evolution of deep convection, and therefore subsequent rainfall.
In the previous chapter, the dynamic and thermodynamic characteristics
of arc cloud lines were presented using data from a series of research
aircraft flights specifically undertaken to study arc cloud lines. In
this chapter, a physical model will be presented to describe the
behavior of arc cloud lines and the process of convective scale
interaction.

This chapter is divided into three sections. The first section
will use observational data to describe the life cycle of the arc cloud
line: its development, the driving forces that sustain it and its
ultimate decay. The second section investigates differences between
the cumulus convective regions and clear regions in the air in advance
of an arc cloud line. In that section, it will be shown why those
differences lead to a different convective response upon interaction
with an arc cloud line. In the final section a discussion of the
convective scale interaction process will be presented.

6.1 Arc Cloud Line Life Cycle

In this section, various features of the arc cloud line and its time evolution will be explored. Based on aircraft and satellite observations of arc cloud lines, the life cycle of the arc cloud line may be categorized into three general stages. Those stages are: 1) the formative stage; 2) the mature stage; and 3) the dissipation stage. In considering the arc cloud line's life cycle, one must realize that arc cloud lines are evolving phenomena and exactly when one stage ends and the next begins is not distinct. The three stages transition one to the other, and along an arc cloud line all three may be in existence at the same time. Furthermore, no two arc cloud lines are exactly alike. This is due to differences in the character of their generation mechanisms (parent storm's intensity and life cycle) as well as convective scale interactions that occur along the arc cloud line as it evolves. A similar observation concerning mature thunderstorm gust fronts was noted by Goff (1976), "each outflow is affected by the behavior and character of the parent thunderstorm ... [t]his produces much variation from case to case and makes difficult the description of a representative outflow model." While Goff's observation of "representativeness" may be true, the distinguishing characteristics and features of arc cloud lines are driven by physical processes, and it is those processes that will be explored in the sub-sections to follow.

As mentioned above, the arc cloud line's life cycle may be classified into three general stages. The three stages are most readily distinguished from one another by their link to their source. In the formative stage the arc cloud line is intimately connected to

the parent storm and may be thought of in terms of that storm's gust front. In the mature stage the arc cloud line has moved sufficiently far away from the storm's downdraft that it may be treated as a density current. In the arc cloud line's dissipating stage, the parent storm has dissipated and new cold air production has ceased.

6.1.1 Arc Cloud Line Formative Stage

In its formative stage the arc cloud line is an extension of the gust frontal boundary produced by active convection. In this early portion of the arc cloud line's life, the movement of the storm and its gust front is essentially as described by Newton (1966): "This downdraft air, reaching the lower layers with excessive momentum, plays an important role in mechanically lifting the warm air at the intense convergence zone on its forward side, and thus continually regenerating the updraft." As was inferred by Newton (1966), during this early stage of the arc cloud line's development the outflow is highly focused. That this is the case may be seen by comparing the aircraft penetrations shown in figures 5.10 and 5.11. For those penetrations, the aircraft's flight track was adjusted from penetrations #1 and #2 (figure 5.10) to be directly in line with the outflow's intense convergence zone, as shown by penetration #4 in figure 5.11. While both precipitation drag and evaporative cooling are important in the initiation of a storm's downdraft, it is the evaporation of raindrops that is responsible for the excess pressure within the cold dome of a mesosystem. Fujita (1959), showed that the excess mass in a cold dome was a function of the evaporation of rain inside the boundary, with the total excess mass being greater the higher the cloud base. This was later confirmed by Betts (1976) when he found that the mean evaporation

in the downdraft increased with the depth of the subcloud layer. This excess pressure plays an important role in the life cycle of an arc cloud line as well as the convective scale interaction process.

As the formative stage of the arc cloud line evolves, the storm's gust front begins to advance outward from the parent storm, and a decoupling of the storm's downdraft driven gust front and its updraft has begun. As this stage transitions to the mature stage, the arc cloud line takes on the characteristics of a density current. It is here that most previous research (Goff, 1976, Wakimoto 1982) concerning thunderstorm gust fronts (outflows) has ceased. For example, Wakimoto (1982) refers to this stage as the gust fronts dissipating stage. In the aircraft investigations of arc cloud lines described in the previous chapter, the Colorado penetration of 12 August 1982 (section 5.3.2) was the only time an arc cloud line was investigated during its formative stage. For that flight, penetrations were confined to the subcloud layer above the density surge line. A schematic of this stage of an arc cloud line's development is shown in figure 6.1 which combines the results of the research aircraft flight with results from the Doppler radar observations of Wakimoto (1982) from Project NIMROD (Northern Illinois Meteorological Research on Downburst (Fujita, 1978)).

Within a relatively deep DSL, a strong cold outflow jet exists several hundred meters above the surface. During this stage, a precipitation roll may exist in the cool air near the leading edge of the DSL. A relatively rapidly moving DSL pushes out into an undisturbed environment causing both strong convergence and intense mixing along the DSL interface. This strong mixing results in the
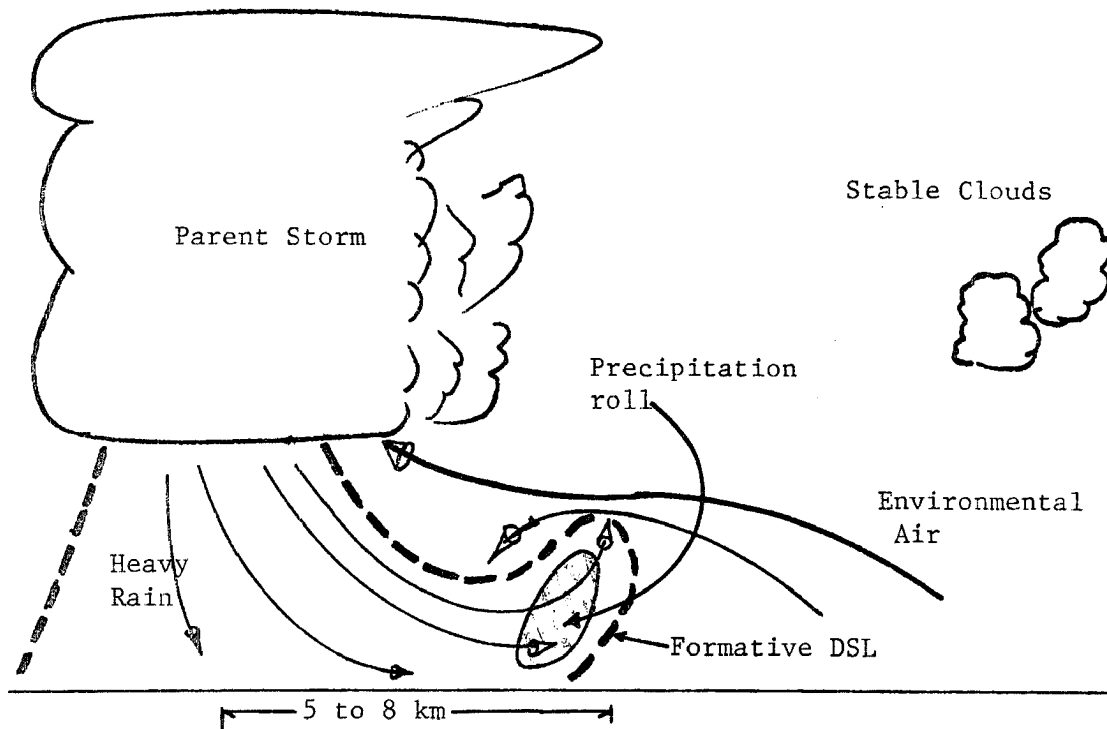
Figure 6.1a. Early formative stage, adapted from Wakimoto (1982). Rain advances ahead of storm at low levels and precipitation roll begins to form.
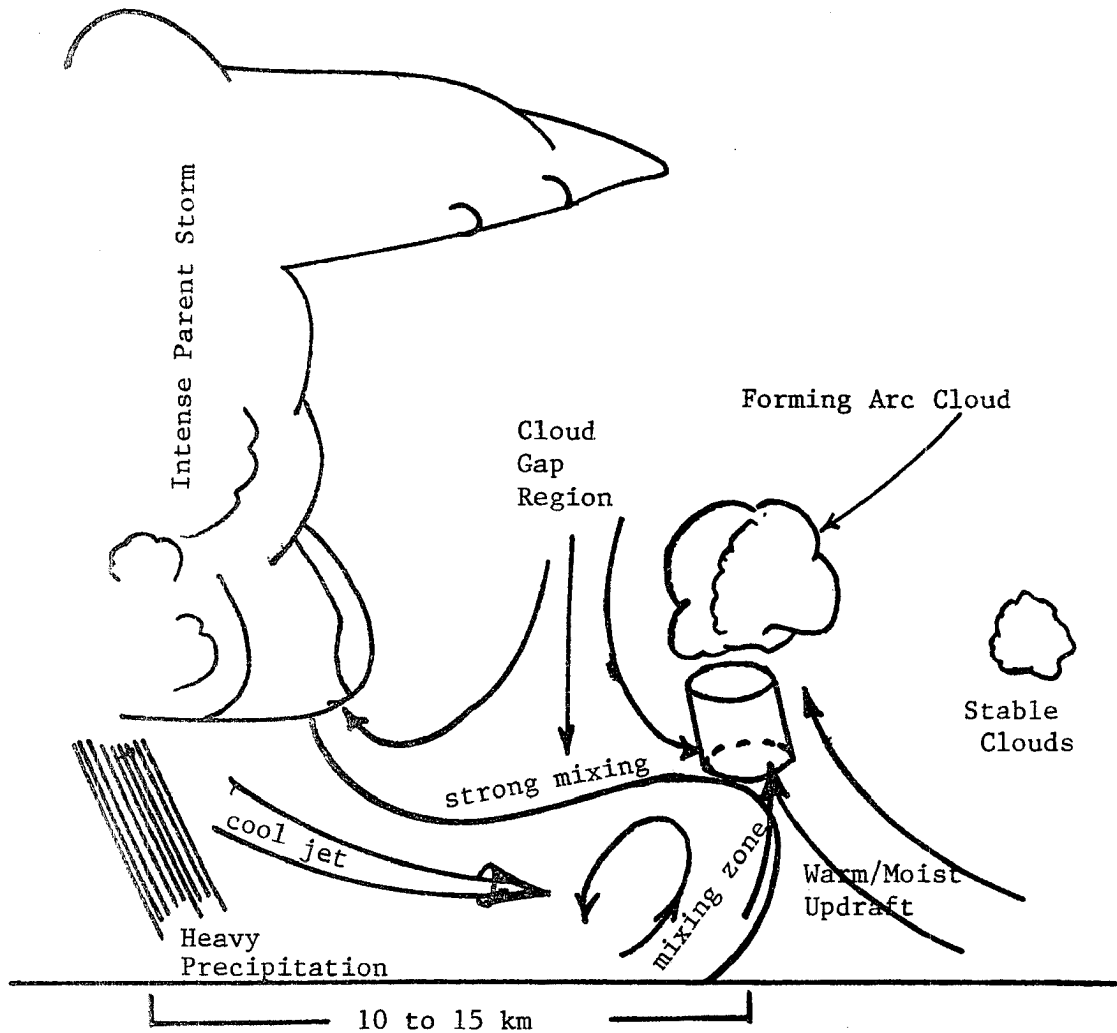
Figure 6.1b. Late formative stage, precipitation roll in dissipation stage. Dark line is boundary of density surge line. The schematic above the DSL is based on aircraft observations of Sinclair and Purdom (1984), while the DSL interface and cool air portion is from Wakimoto's Stage III (1984) and laboratory tank models (figure 5.15). See figure 6.2 for more detail.

entrainment of outflow air into the warmer environmental air that is thrust upward by the forward motion of the DSL. Similar turbulent mixing features are exhibited by laboratory gravity currents and low-level atmospheric observations of haboobs, squall lines and cold fronts. This mixing results in a mixed updraft region beneath the arc cloud line. Relative to the DSL interface, horizontal air motions in both the cool outflow air and environmental air decrease as they approach the interface, and strong upward vertical motions exist in both those regions.

The air between the DSL interface and arc cloud line base is a reflection of the strong dynamics in those regions. A distinct updraft vertical motion field exists beneath the arc cloud line, with downward motion along the updraft flanks. In the region between the thunderstorm and arc cloud line, the cloud gap region, there is cool and moist descending air. There is a sharp decrease in vertical motion in the updraft region, between the updraft maxima and cloud gap downdraft air: the air in that portion of the updraft is also cooler and more moist than other parts of the updraft air beneath the arc cloud. The most likely reason for this difference in updraft structure is the mixing of environmental air with that in the DSL interface region and the cloud gap region. Because of the turbulent nature of the flow and intense mixing that is occurring along the DSL interface at this stage of an arc cloud line's development, it is not possible to determine the various source regions for the air parcels at flight level. While a number of possibilities exist (see figure 6.2), some insight into this early stage of the arc cloud line's evolution may be gained by determining possible mechanisms leading to an updraft
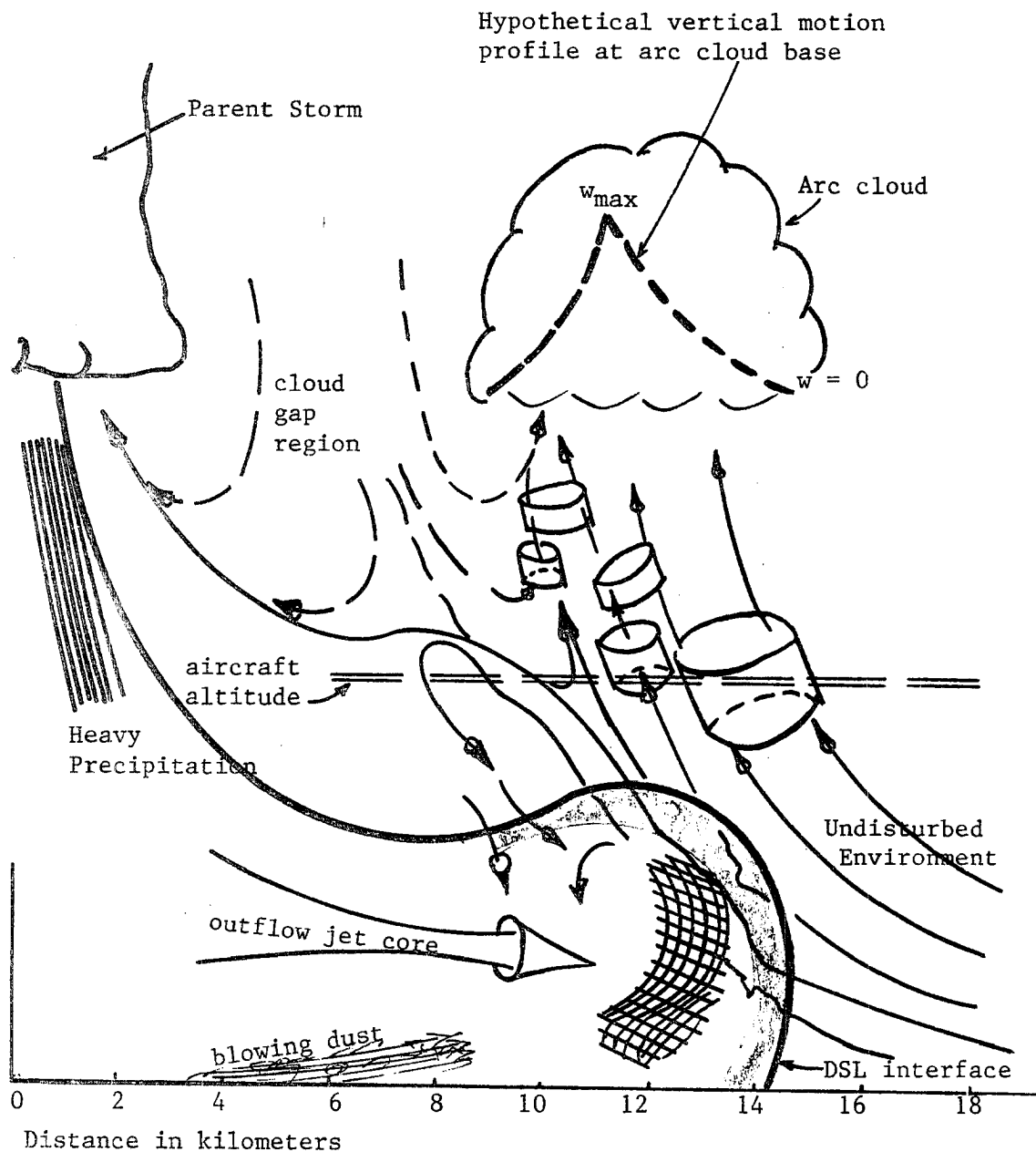
Figure 6.2. Several of a number of possible trajectories for air entering updraft region of arc cloud during formative stage. Shaded region is area of intense mixing along DSL interface, while hatched region is possible area of precipitation roll. Convergence in the warm air due to the advancing DSL interface is on the order of 10^{-2} sec^{-1}. Based on aircraft observations of Sinclair and Purdom (1984).

structure as was measured on August 12. This will be done after a

short discussion of the arc cloud line's late formative stage.

In the late formative stage of the arc cloud line's development,

it has begun to move away from the parent storm, and at this time its

motion may be treated as that of a density current. Density currents

have been studied theoretically (von Karmen, 1940; Benjamin, 1968), in

laboratories (Middleton, 1966; Simpson, 1969), and related to the

atmospheric arc cloud line outflow phenomena using numerical models

(Seiter, 1983). A number of scientists involved in field studies have

related the speed of motion of thunderstorm gust fronts and outflows to

that of a density current (Charba (1974), Goff (1976), Wakimoto

(1982)). The speed of motion of the density surge line (DSL)

interface, which is due to the density difference between the cold and

warm air and the depth of the cold air, is given by the relationship,

$$V = k\left(gh\ \frac{\bar{\rho}-\bar{\rho}_e}{\bar{\rho}_e}\right)^{1/2} .$$ (6.1)

In equation (6.1):

V is the speed of the leading edge of the density current;

g is the acceleration of gravity;

h is the depth of the outflow;

$\bar{\rho}$ is the mean density of the cold air;

$\bar{\rho}_e$ is the mean density of the warm air; and
k is the internal Froude number which is the ratio of inertial to
gravitational force.

Equation 6.1 was first derived by von Karmen (1940). In that

derivation, von Karmen assumed a perfect-fluid gravity current was

moving horizontally in steady state at the bottom of an infinitely deep

fluid that was of lesser density than that of the density current. By

applying Bernoulli's equation for a steady, frictionless,

incompressible and irrotational flow, von Karmen arrived at the

relationship given by equation 6.1, where the value of k would be the

square root of 2. Because of frictional effects and mixing, both

laboratory and atmospheric scientists have found that real density

currents move at a velocity less than predicted by 6.1 when k is set to

1.414. This difference in velocity has historically been accounted for

by adjusting the value of k: for example Keulegan (1958) used k=0.78,

Charba (1974) found k to be 1.08 and Wakimoto (1982) found k to vary

between 0.71 and 0.87 with an average value of 0.77.

While the leading edge of the arc cloud line's associated DSL may

be moving with the speed of a density current in the late formative

stage, the horizontal winds in the cold air behind the DSL are flowing

into the DSL interface region at a greater velocity than is exhibited

by the motion of the DSL interface. This was shown in the Doppler

radar measurements of Wakimoto (1982), and may be inferred from the

work of Gurka (1976) in which he showed that with active deep

convection along (or very close to) an arc cloud, that the velocity of

reported surface winds could be as high as twice the speed of motion of

the arc cloud line. This strong relative flow in the cold air behind

the DSL leads to low level convergence and upward vertical motion in

the cold air at the rear of the DSL interface. The largest values of

divergence found during Project NIMROD were on the order of 10^{-2} sec^{-1},

from which Wakimoto (1982) calculated vertical motions of +8 m sec^{-1}
for the forced updraft at the gust frontal boundary.

It was shown by Wakimoto (1982) that, relative to the leading edge
of the DSL, winds in both the cold and warm air decrease in velocity as
they advance into the interface region. This decrease in wind speed is
a maximum near the surface and appears to decrease to near zero at the
top of the DSL interface. Such a decrease in the wind speed can be
shown to lead to the development of a dynamic pressure force whose
value is given by 6.2:

$$P_{dy} = 1/2 \; \rho \left(V^2_{c \; w} - V^2_s \right), \qquad (6.2)$$

where P_{dy} is the dynamic pressure,
ρ is the density of the air,

$V_{c,w}$ is the windspeed in the cold air or warm air,
and V_s is the velocity at the stagnation point.

Equation 6.2 is valid for steady and incompressible flow when applied
along the stagnation point streamline at the stagnation point, where
the velocity, V_s, is assumed to be zero. Although such a flow is
highly idealized for outflow applications, this decrease of dynamic
pressure with height might help sustain vertical motion in the air on
both the cold and warm air sides of the DSL. Table 6.1, adapted from
Wakimoto (1982), presents nonhydrostatic pressures on both the warm and
cold air sides of three Project NIMROD gust front cases. If such
nonhydrostatic pressures exist and can be sustained while air parcels
are under their influence they can effect arc cloud line development.

Table 6.1

Nonhydrostatic pressure calculations

	Case A	Case B	Case C
ρ_c (density of cold air) X 10⁻³ (g cm-³)	1.189	1.171	1.165
ρ_w (density of war air) X 10⁻³ (g cm-³)	1.183	1.163	----
P_{nhc} (nonhydrostatic pressure in the cold air) (mb)	1.34	0.15	0.58
P_{nhw} (nonhydrostatic pressure in the warm air) (mb)	1.00	0.33	---
P_t (total nonhydrostatic pressure) (mb)	2.34	0.48	0.58
P_o (nonhydrostatic pressure increase estimated from surface (mb) pressure traces)	2.50	0.50	0.65
Cold air depth (m)	3953	2236	1340

A pertubation equation for vertical motion which accounts for nonhydrostatic pressure forces is given by 6.3:

$$\frac{dw'}{dt} = - g \frac{\Delta T}{T} - \frac{1}{\rho} \frac{\partial \rho'}{\partial z} + F_z,$$

(6.3)

where $\frac{dw'}{dt}$ is the vertical acceleration a parcel will experience due to bouyancy, $- g \frac{\Delta T}{T}$, to the vertical variation of nonhydrostatic pressure, $\frac{1}{\rho} \frac{\partial \rho'}{\partial z}$, and to frictional effects, F_z. Table 6.2 shows the accelerations due to nonhydrostatic forces in table 6.1 (this assumes a zero nonhydrostatic pressure force at the top of the cold dome) and the mean acceleration due to parcel negative bouyancy deep within the cold dome (where ΔT and $\overline{T}$ were estimated based on parcels lifted from near the surface to the top of the cold dome).

While the negative buoyancy shown in table 6.2 may be applicable deep within the cold dome, it is not representative of buoyancy values expected to be encountered in the cold air near the leading edge of the outflow; the region where the dynamic pressure forces may be operative. Figure 6.3, from Mitchell and Hovermale (1977), indicates that the air within the interface region is neutrally buoyant, with the outflow frontal interface being almost vertical at the leading edge of the cold outflow. Referring again to table 6.2, it is evident that weak negative buoyancy within the cold air near the interface can be overcome by dynamic pressure forces if such dynamic pressure forces are able to be sustained.

Table 6.2

Vertical Accelerations due to nonhydrostatic
pressure (P_{nh}) and buoyancy (B)

	Case A	Case B	Case C
P_{nh} generated vertical accelerations in cold air (cm sec^{-2})	2.85	0.57	3.72
P_{nh} generated vertical accelerations in warm air (cm sec^{-2})	2.13	1.26	0.00
Resulting B vertical accelerations deep within cold dome (cm sec^{-2})	-10.21	-5.39	-6.67
ΔT capable of being overcome within the cold dome by P_{nh} assuming T of 290°k	0.84°	0.17°	1.10°
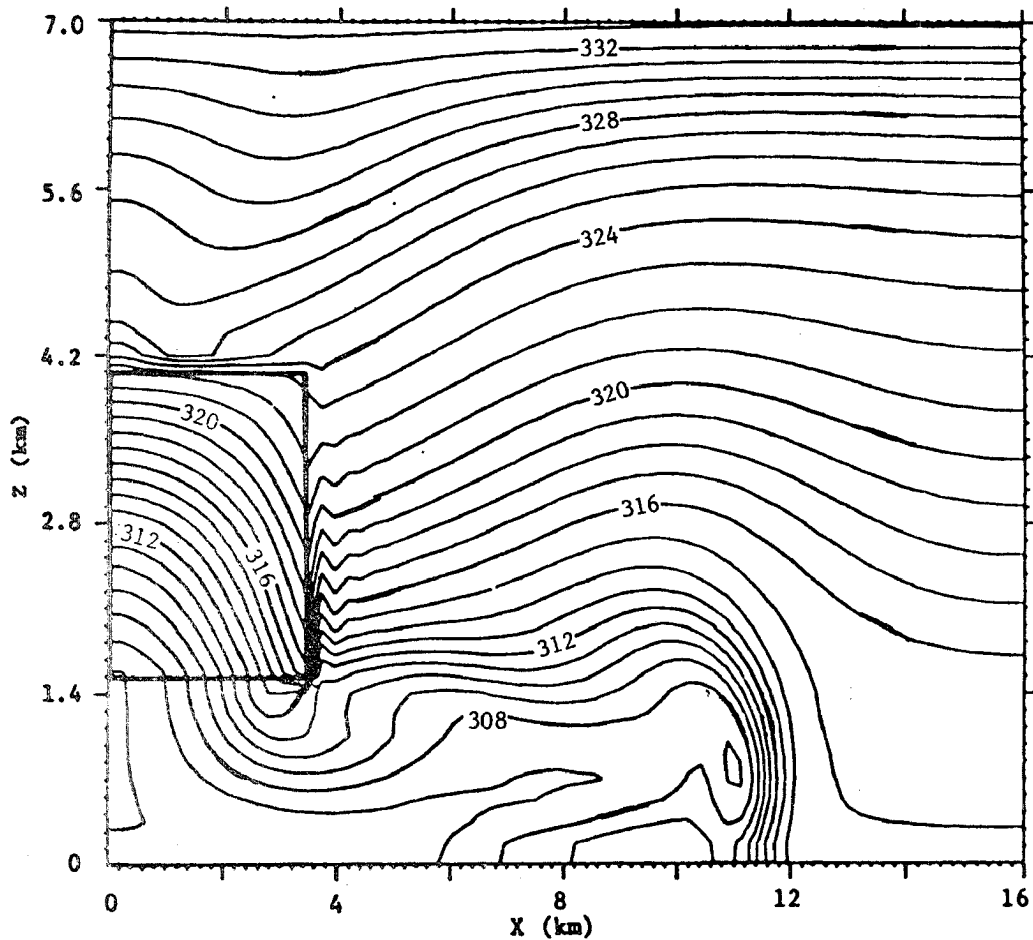
Figure 6.3. Potential temperature field at t = 12.00 min. from
Mitchell and Hovermale (1977). The heavy line corresponds to
the DSL interface.

The strong baroclinicity that exists across the arc-line front also provides a significant part of the energy for the updraft region within the cold air just behind the frontal surface. Similar arguments have been used, Goff (1976), and Mitchell and Hovermale (1977), to explain solenoidal circulations in severe gust front leading edges. Based on the work of Sinclair and Purdom (1983), an estimate of the mean solenoidal velocities for this later situation can be deduced from the circulation theorem ($C = \oint \vec{v} \cdot \vec{dr}$) in the following form:

$$\frac{dC}{dt} = - \oint \frac{dp}{\rho} = - \int_A (\nabla\alpha \times \nabla p) \cdot \vec{dA} = -R \int_A T(\nabla \ln\Theta \times \nabla \ln P) \cdot \vec{dA} \qquad (6.4)$$

where $\vec{v}$ is the velocity vector in the vertical plane, $\vec{dr}$ is the radius vector increment, α the specific volume, R the gas constant for dry air, ∇p the pressure gradient which may be due to both the hydrostatic pressure rise in the cold dome and other non-hydrostatic components (such as the dynamic pressure previously addressed), T the temperature, Θ the potential temperature, and $\vec{dA}$ is the incremental vector area around which the circulation is to be determined. Note Coriolis and frictional forces have been neglected and the line integral ($\oint$) has been changed to an area integral by Stoke's theorem. The circulation (C) or time rate of change of circulation is dependent on the number of α, -P solenoids in the highly baroclinic zone formed by differential advection at the leading edge of the gust front.

Evaluating the integral in Equation 6.4 for the severe gust front case of Mitchell and Hovermale (1977) reveals that the time rate of change of the circulation is approximately:

$$\frac{dC}{dt} = 3.22 \times 10^6 \text{ cm}^2\text{sec}^{-2}, \qquad (6.5)$$

with the corresponding mean acceleration of

$$\frac{d\bar{V}}{dt} = 6.88 \text{ cm sec}^{-2}. \tag{6.6}$$

Assuming that the baroclinicity remains constant with time, the mean vertical velocities can reach 13.8 m sec^{-1} in a time increment of only 200 sec. This result is consistent with the positive vertical motions observed and modeled behind the gust front in the cold air. Consequently, to preclude run-away velocities developing in the gust frontal boundary by solenoidal forces, the frictional forces must play an important and decisive role. These frictional forces may be either in the form of turbulent mixing or surface drag components.

Inspection of figure 5.11 (and figure 6.2) illustrates how in the formative stage of the arc cloud line mixing and vertical forcing may be very strong. For example, those figures show that in the rear of the updraft, air which is experiencing downward acceleration on the order of -5 to -7 cm sec $^{-2}$ due to buoyancy considerations is moving upward with velocities between 2 and 7 m sec^{-1}! Although penetrations for this particular case were confined to the subcloud layer above the DSL interface and below the convection along the arc cloud line, it is possible to estimate the magnitude of the vertical forcing required to support the observations. The data for the penetration shown in figure 5.11 was taken with the aircraft at an altitude approximately 1400 m AGL and 1500 m below cloud base. Based on previous studies (see table 3.1) it is very likely that this penetration was between 100 m and 700 m above the DSL interface. The negatively buoyant air within the arc cloud line updraft region covers a horizontal distance of approximately 2.5 km. Assuming that the air from within the center of the negatively

buoyant portion of the updraft core has been forced undiluted through
the top of the DSL interface to penetration altitude allows calculation
of various combinations of vertical forcing in the cold air at the DSL
interface, DSL interface height and mean negative buoyancy experienced
during the ascent. Results shown in figure 6.4 are for cases where $\bar{T}$
was assumed to be 288° K, and w at the penetration level was set to 4 m
sec^{-1}. For example, assuming that the aircraft penetration was 300 m
above an 1100 m deep DSL, and the undiluted negative temperature
pertubation was -3°C gives a value of 8.8 m sec^{-1} forced vertical
motion at the top of the DSL interface.

Laboratory tank models have shown that strong mixing occurs in the
DSL interface region, this was verified by the aircraft flights
discussed in section 5.3.3.1. Evidence of mixing into the updraft of
outflow air with air from both the cloud gap region and the warmer
environment is apparent in figure 5.11. While the maximum vertical
motion found in the environmental air portion of the updraft approaches
eight to ten meters per second, that peak drops off sharply as cooler
and more moist air appears in the updraft. Figure 6.5 show vertical
motion profiles calculated for mixed parcels, with mixing as in section
5.3.1.2, using equation (6.3) in the form

$$d\left(\frac{w^2}{2}\right) = \left(-g\,\frac{\Delta T}{\bar{T}}\right)dz. \tag{6.7}$$

The calculations were done for parcels originating from the top of a
DSL with a -2°C negative temperature anomaly and initial vertical
motions (at the DSL interface) of 8.4 m sec^{-1} for a DSL 400 meters
below the aircraft. Inward mixing of adjacent air parcels was set at
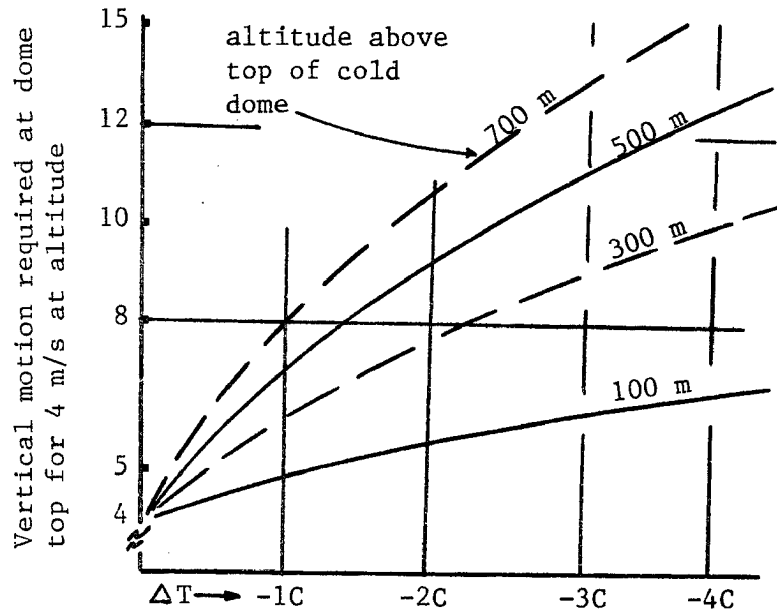
Figure 6.4. Vertical motion required at the top of a cold dome to overcome a given negative buoyancy for a parcel and have a vertical motion of 4 m sec^{-1} at the altitude indicated in the graph (see text for details)
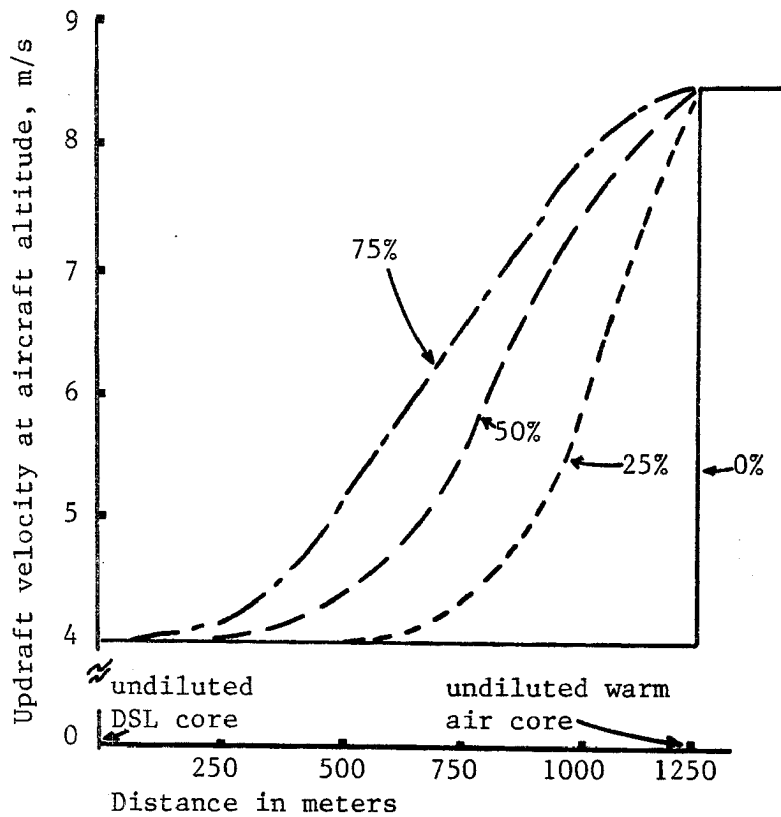
Figure 6.5. Vertical motion fields at 400 meters above DSL which result from inward mixing of environmental air with negatively buoyant air from within the DSL (see text for details).

0%, 25%, 50% and 75% over 50 meter vertical intervals. These mixing values (except 0%) represent a reasonable range of estimates based on the aircraft observations and mixing values (16% to 67%) presented in section 5.3.1.2 of the previous chapter. The core of the DSL parcel located 1250 meters from the updraft maximum was assumed to rise undiluted to aircraft penetration altitude. Such an assumption seems reasonable based on previous investigations of moist thermals (Sinclair 1973, Davies-Jones 1974). An initial vertical motion of 8.4 m sec^{-1} at the DSL interface was chosen to be consistent with the observed 8 to 9 m sec^{-1} updraft maxima measured in the war air (assumed to be dry adiabatic), and so that an undiluted negatively buoyant parcel would reach penetration altitude with a vertical motion of approximately 4 m sec^{-1}. Figure 6.5 shows the results obtained for the above situation. Notice that 0% mixing occurs only for undiluted parcel ascents: obviously, when compared with the aircraft measurements in the previous chapter no mixing across the entire updraft region is an unreasonable assumption.

As can be seen in figure 6.5, the effect of mixing of environmental air with air that which has penetrated through the DSL interface is to modify the buoyancy of the updraft air, thus accounting for an updraft structure similar to that shown in figure 5.11. It should be noted that the information shown in figures 6.4 and 6.5 are not meant to exactly replicate that shown in figure 5.11, but rather to show that the vertical forcing required within the DSL is not unreasonable and is substantiated by the aircraft measurements.

Thus, the formative stage of the arc cloud line's life cycle is characterized by a highly channeled storm outflow. Within the cold

outflow air, convergence of high momentum air into the rear of the DSL

interface along with the development of a solenoidal circulation and

dynamic pressure forces lead to strong vertical motions within that

negatively buoyant air. The lifting of warm environmental air by the

cold outflow air, as well as possible dynamic pressure forces, gives

rise to a significant vertical motion field just ahead of the arc-line

gust front. Mixing of air from within the DSL with the warm and more

instable air ahead of it contributes to a modified updraft structure

that feeds the cumulus clouds along the arc cloud lines. Figure 5.11

is representative of the type updraft one should expect to encounter

during the late formative stage of an arc cloud lines life cycle.

6.1.2 Arc Cloud Line Mature and Dissipating Stages

As was pointed out in the previous section, in the formative stage

of the arc cloud line's development the parent storm's outflow is

highly channeled. As the formative stage evolves to the mature stage,

the DSL becomes well established and moves out from the parent storm at

a more uniform velocity than that exhibited during the formative stage.

At this time in the arc cloud line's life cycle, the beginning of the

mature stage, the DSL takes on the characteristics of a density

current, with its velocity closely approximated by equation 6.1.

Wakimoto (1982) showed that the "pressure rise behind the gust front is

solely a function of the cold outflow." Because that pressure rise is

largely hydrostatic, equation 6.1 may be reduced to,

$$V = k*\left(\frac{\Delta P}{\rho_e}\right)^{1/2}, \qquad\qquad (6.8)$$

where ΔP is the pressure difference between the warm and cold air, and k^* is a modified Froude number. Based on a series of two dimensional numerical model simulations, Seiter (1983) found an appropriate value for the constant k^* of 0.79.

As the arc cloud line matures, and its parent storm begins to weaken, the speed of motion of the arc cloud line decreases. Since the density difference between the cool air within the arc cloud line and the warmer environmental air plays a major role in determining arc cloud line velocity, it is important to understand how their changes in time would affect outflow behavior. Fujita (1959) showed that the total excess pressure within a cold dome, integrated over the area covered by the dome, remained virtually unchanged by subsidence. Thus if A_i and ΔP_i represent initial values for area and excess pressure within a cold dome whose cold air source has dissipated, then,

$$A_i \ \Delta P_i = A_f \ \Delta P_f, \qquad (6.9)$$

where A_f and $\Delta \rho_f$ are final area and excess pressure for the expanding cold dome. Therefore as the cold dome sinks and spreads out seeking equilibrium with its surrounding environment (refer to figure 3.14) the excess pressure driving the density current decreases in proportion to the increase in the area it covers,

$$\Delta P_f = \frac{A_i}{A_f} \Delta P_i. \qquad (6.10)$$

If the area covered by a cold dome (arc cloud line boundary) doubles, the pressure driving the density current will decrease by a factor of two, which results in a velocity decrease by a factor of approximately 0.71. Figure 6.6, shows the relationship between excess
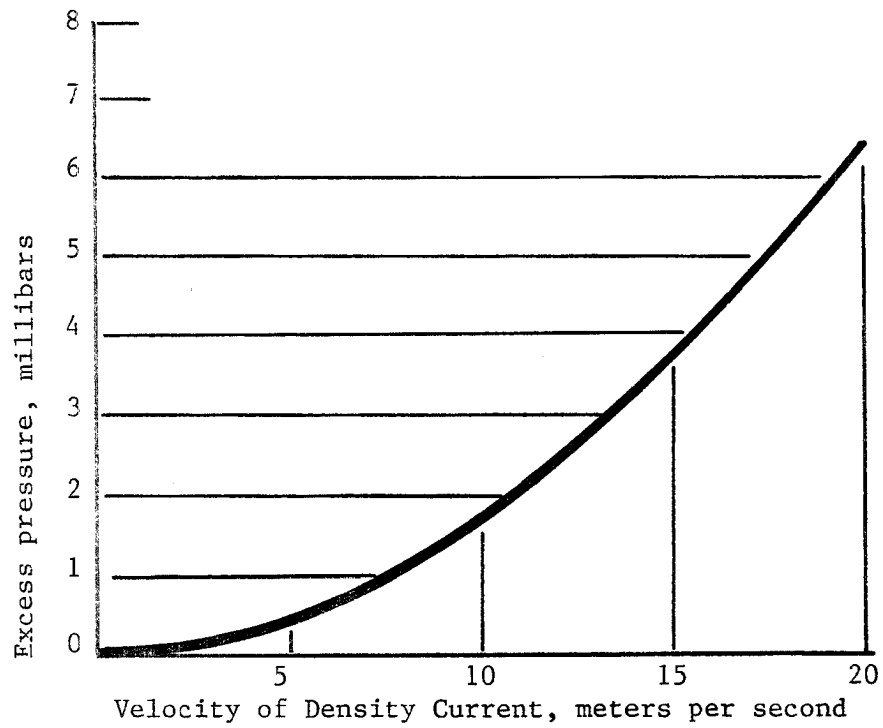
Figure 6.6. Velocity of density current as function of pressure difference between warm and cold air, assuming $\bar{\rho}_e = 10^{-3}$ gm/cm^3, and k* = 0.79.

pressure in a cold dome and the velocity of a density surge line.

During the first half of July for the study discussed in chapter 4,

measurements were made of the distance an arc cloud line moved between

the time of its initial detection to when it caused new storm

development colder than -20°C. Results for this radius of interaction

are shown in figures 6.7a and 6.7b. In interpreting those figures it

must be realized that the velocity ranges for the various arc cloud

lines in question included only those portions of an arc upon which new

convection (colder than -20°C) developed. Figures 6.7a and 6.7b will

be referred to again later in this chapter, however, for this section

it is important to note that the most active portions of the arcs were

moving between 15 m sec^{-1} and 7 m sec^{-1} with an average velocity of

approximately 11 m sec^{-1}. The above velocity values correspond to

pressure pertubations in the cold dome of approximately 3.75 mb(15 m

sec^{-1}), 0.75 mb(7 m sec^{-1}), and 1.9 mb*(11 m sec^{-1}) respectively. That

these values are reasonable may be seen by inspecting figure 1.1 where

pressure pertubations vary from 2.3 to 3.3 mb in Arkansas, to 2.0 mb in

Mississippi, and from 0.9 mb to 1.1 mb in Alabama, to 2.2. mb in

Georgia. Based on 15 minute interval satellite imagery, measurements

of the speed of motion of the arcs in those regions were found to be in

good agreement with estimations using relationship 6.8.

Table 6.3 shows how under calm conditions, excess pressure

pertubations of various sizes would behave as a function of time for

cold a source that has dissipated at the initial time. For example in

Case B, an initial cold source with an excess pressure of 4.1 mb exists

over a circular area of 50 km in radius and 1.5 km in depth. With no
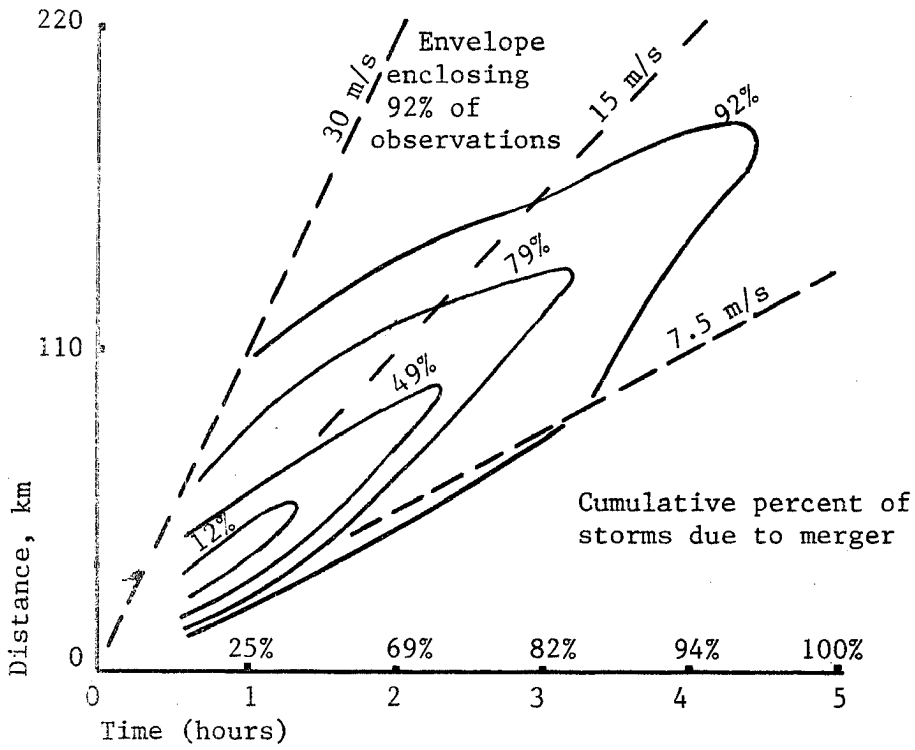
Figure 6.7a. Radius of interaction for mergers.
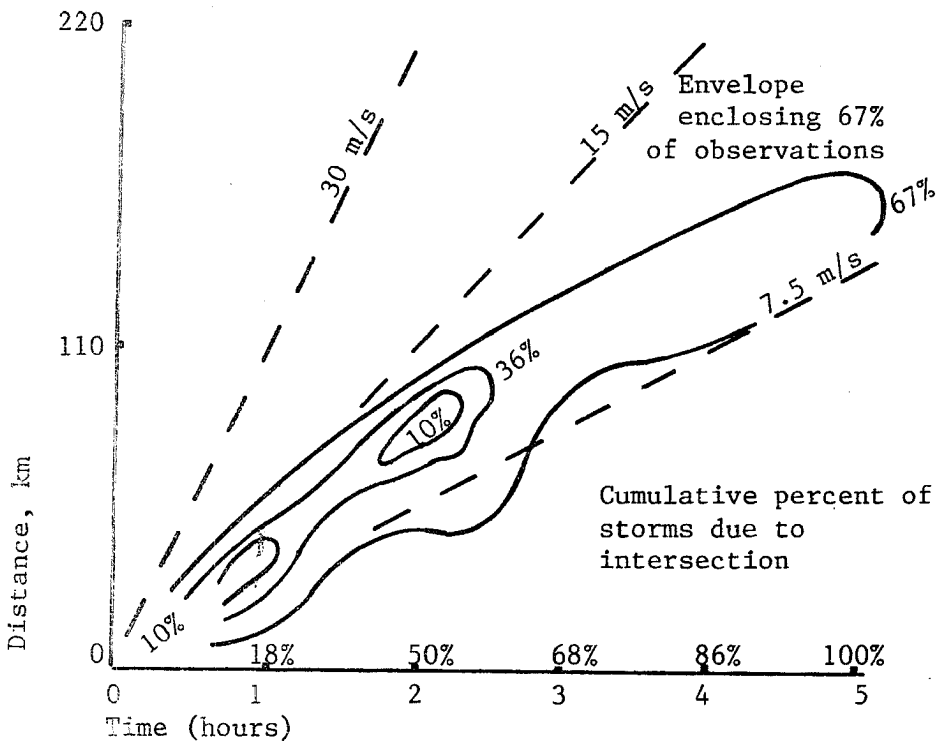
Figure 6.7b. Radius of interaction for intersections.

142

Table 6.3

Size and velocity of pressure pertubation as a function of time
for a situation where the cold air source has dissipated

	Δρ(mb)	Boundary Velocity (m sec⁻¹)	Dome Radius (km)	DSL Depth (km)	Time to Double in Size	Elapsed Time min.
Case A	4.10	16.0	100	1.50	50.5	initial
A	2.05	11.3	141	0.75	101.1	50.5
	1.03	8.0	200	0.38	202.1	151.6
	0.51	5.7	2821	0.19	404.3	353.8
Case B	4.10	16.0	50	1.50	25.3	initial
	2.05	11.3	70	0.75	50.5	25.3
	1.03	8.0	100	0.38	101.1	75.8
	0.51	5.7	141	0.19		176.9
Case C	2.05	11.3	100	1.50	71.5	initial
	1.03	8.0	141	0.75	142.9	71.5
	0.51	5.7	200	0.38	285.9	214.4
	0.25	4.0	282	0.19		500.3
Case D	2.05	11.3	50	1.50	35.7	initial
	1.03	8.0	70	0.75	71.5	35.7
	0.51	5.7	100	0.38	142.9	107.2
	0.25	4.0	141	0.19		250.1

new air being provided by an active cold air source (i.e. the parent
storm has dissipated), initially the boundary will move outward at 16
m sec^{-1}. When the dome area has doubled, the excess pressure and dome
depth will have decreased by a factor of 2 (i.e. Δp (mb) = 2.05 and
DSL depth = 0.75 km), and the velocity of the boundary will be 11.3 m
sec^{-1}. This gives an average velocity of 13.65 m sec^{-1} which means for
the domes radius to spread from 50 km to 70.7 km requires an elapsed
time of 25.3 minutes. As case B evolves in time, note that the
velocity of the boundary has a value of approximately 35% its initial
value after almost three hours. Thus, table 6.3 shows that after the
active cold air source has dissipated, the arc cloud line will maintain
a substantial velocity for a considerable period of time. However,
note that the depth of the DSL will decrease in time as the arc cloud
line spreads out.

When considering the velocity of an arc cloud line during its
mature stage, it should be remembered that this stage is one in which
the arc cloud line's cold air source is still active. Furthermore as
was shown in the previous chapter, precipitating clouds are often found
along the outflow arc. Both of those factors will contribute to a
larger pressure pertubation within the cold air than for a similar
situation in which the cold air source has totally dissipated.
Therefore, the values given in table 6.3 will be lower than should be
expected for arc cloud line characteristics during the mature stage,
however they represent appropriate estimates for the dissipating stage.
Table 6.4, developed for comparison with table 6.3, presents the
behavior of excess pressure pertubations of various sizes that
gradually decrease in intensity as the cold dome spreads out. Note

Table 6.4

Size and velocity of pressure pertubation as a function of time, but
with dome pressure excess gradually decreasing by a constant percent
for each doubling of dome area.

Case I: ΔP = 4.10 mb, Radius = 50
Case II: ΔP = 2.05 mb, Radius = 50

	ΔP(mb)	Boundary Velocity (m sec^{-1})	Dome Radius (km)	DSL Depth (km)	Time to Double in Size	Elapsed Time min.
Case I 10%	4.10	16.0	50	1.50	21.4	initial
	3.69	15.2	70	1.35	33.8	21.4
	3.32	14.4	100	1.21	48.6	55.2
	2.99	13.7	141	1.09	0	103.8
Case I 20%	4.10	16.0	50	1.50	22.0	initial
	3.28	14.3	70	1.20	36.9	22.0
	2.62	12.8	100	0.96	56.6	58.9
	2.10	11.4	141	0.77	0	115.4
Case I 30%	4.10	16.0	50	1.50	22.7	initial
	2.87	13.4	70	1.05	40.7	22.7
	2.01	11.2	100	0.74	65.7	63.4
	1.41	9.4	141	0.52	0	129.1
Case I 40%	4.10	16.0	50	1.50	23.5	initial
	2.46	12.4	70	0.90	45.5	23.5
	1.48	9.6	100	0.54	80.4	69.0
	0.89	7.4	141	0.32	0	149.4
Case II 10%	2.05	11.3	50	1.50	30.3	initial
	1.85	10.7	70	1.35	46.5	30.3
	1.67	10.2	100	1.21	68.7	76.8
	1.50	9.7	141	1.09	0	145.5
Case II 20%	2.05	11.3	50	1.50	31.5	initial
	1.64	10.1	70	1.20	52.4	31.5
	1.31	9.0	100	0.96	79.9	83.9
	1.05	8.1	141	0.77	0	163.8
Case II 30%	2.05	11.3	50	1.50	32.1	initial
	1.44	9.5	70	1.05	57.5	32.1
	1.01	7.9	100	0.74	94.3	89.6
	0.71	6.6	141	0.52	0	183.9
Case II 40%	2.05	11.3	50	1.50	33.2	initial
	1.23	8.8	70	0.90	65.1	33.2
	0.74	6.8	100	0.54	113.0	97.3
	0.44	6.3	141	0.32	0	210.3

that a decrease in dome excess pressure of 50% for each doubling of dome area is the situation in which no new cold air is being added to the dome (i.e. table 6.3). For example in Case I (20%), an initial cold source with an excess pressure of 4.1 mb exists over a circular area 50 km in radius and 1.5 km in depth. Rather than have the source totally dissipate at the initial time (as in table 6.3), let the excess pressure in the cold dome uniformly decrease by 20% (thus it is 80% of its initial value) by the time the dome area has doubled in size. This corresponds to a decrease in cold air production by the parent source of 40% from the initial time to the doubling time. By the time the cold dome has doubled in area both its excess pressure and depth have a value that is 80% of their initial value (i.e. Δp(mb) = 3.28 and DSL depth = 1.2 km), and the velocity of the boundary will be 15.2 m sec^{-1}. Thus, the time for the dome radius to spread from 50 km to 70.7 km requires an elapsed time of 21.4 minutes. As Case I (20%) evolves in time, note that the velocity of the boundary has a value of approximately 71% its initial value after almost two hours.

For comparison purposes, take for example Case I in which the dome's excess pressure decreases by 20% each time it doubles in size compared with Case B in table 6.3. Both attain a radius of 100 km in approximately one hour, however, Case I (20%) has a velocity 1.6 time as great as Case B, and its dome is 2.53 times as deep as Initial (B). Such a marked differences, due to a cold source staying active, have a profound influence on the vertical motions capable of being generated at the leading edge of the DSL due to forced convergence.

The impact of cold air source dissipates on the vertical motion forced in the warm air by the outflow boundary can be seen by

inspecting table 6.5 and figure 6.8. The values for vertical motion in the warm air were determined, based on the values in table 6.3 and 6.4, using a two dimensional incompressible continuity equation for an outflow moving as a density current into a still environment.

The use of a simple two-dimensional incompressible continuity equation may be justified by inspecting the results obtained from integrating the anelastic form of the continuity equation (Pielke, 1984) from ground level $(w(0), z(0), \alpha_o(0))$ to the top of the DSL $(w(D), z(D), \alpha_o(D))$ as in equation 6.11:

$$\int_{w(0)}^{w(D)} \delta w = - \int_{z(0)}^{z(D)} \left(\frac{\partial u}{\partial x} + \frac{\partial u}{\partial y}\right) \delta z + \int_{\alpha_o(0)}^{\alpha_o(D)} \bar{w}\delta(\ln\alpha_o) \qquad (6.11)$$

For typical outflow DSL's, with depths between 1.5 km and 0.5 km and vertical motions at the top of the DSL between 2 m $\sec^{-1}$ and 6 m $\sec^{-1}$, it is obvious that the major contribution to that vertical motion is due to the divergence in the subcloud layer since the last term in 6.11 will typically have values around 0.1 to 0.2 m $\sec^{-1}$.

For table 6.5 and figure 6.8, the values of vertical motion given are those which would occur in the warm air due to convergence over a horizontal distance of 4.5 kilometers for a vertical depth equal to the height of the DSL. The 4.5 kilometer distance was chosen based on aircraft observations from the previous chapter. From table 6.5 and figure 6.8 it can be seen how a decrease in both depth and velocity of the DSL can have a considerable impact on the vertical motion field generated in the warm air along the arc cloud line as it spreads out.

Table 6.5

Subsidence of top of DSL interface and vertical motion in the warm air at the height of the DSL interface due to convergence over a distance of 4.5 km. Values for this table are from tables 6.3 and 6.4.

	ΔP(mb)	DSL Depth (km)	Elapsed Time (min.)	Mean Subsidence (cm sec^{-1})	Vertical Motion (m Sec^{-1})
Case I 10%	4.10	1.50	0		5.33
				11.4	
	3.69	1.35	21.4		4.56
				8.2	
	3.32	1.21	55.2		3.87
				4.1	
	2.99	1.09	103.8		3.32
Case I 20%	4.10	1.50	0		5.33
				22.7	
	3.28	1.20	22.0		3.81
				10.8	
	2.62	0.96	58.9		2.73
				5.6	
	2.10	0.77	115.4		1.95
Case I 30%	4.10	1.50	0		5.33
				33.0	
	2.87	1.05	22.7		3.13
				12.7	
	2.01	0.74	63.4		1.84
				5.6	
	1.41	0.52	129.1		1.09
Case I 40%	4.10	1.50	0		5.3
				42.6	
	2.46	0.90	23.5		2.48
				13.2	
	1.48	0.54	69.0		1.15
				4.6	
	0.89	0.32	149.4		0.53
Case B	4.10	1.50	0		5.38
				49.4	
	2.05	0.75	25.3		1.88
				12.4	
	1.03	0.38	75.8		0.68
				3.1	
	0.51	0.19	176.9		0.24

Table 6.5 (continued)

	ΔP(mb)	DSL Depth (km)	Elapsed Time (min.)	Mean Subsidence (cm sec^{-1})	Vertical Motion (m Sec^{-1})
Case II	2.05	1.50	0		3.77
10%				8.3	
	1.85	1.35	30.3		3.21
				5.0	
	1.67	1.21	76.8		2.74
				2.9	
	1.50	1.09	145.5		2.35
Case II	2.05	1.50	0		3.77
20%				15.9	
	1.64	1.20	31.5		2.69
				7.6	
	1.31	0.96	83.9		1.92
				4.0	
	1.05	0.77	163.8		1.39
Case II	2.05	1.50	0		3.77
30%				23.4	
	1.44	1.05	32.1		2.22
				9.0	
	1.01	0.74	89.6		1.30
				3.9	
	0.71	0.52	183.9		0.76
Case II	2.05	1.50	0		3.77
40%				30.1	
	1.23	0.90	33.2		1.76
				9.2	
	0.74	0.54	97.3		0.82
				3.2	
	0.44	0.32	210.3		0.37
Case D	2.05	1.50			3.77
				35.0	
	1.03	0.75	35.7		1.33
				8.7	
	0.51	0.38	107.2		0.4
				2.2	
	0.25	0.19	250.1		0.17

Figure 6.8. Illustration of local forcing in the warm air due to a DSL moving out into a quiescent environment. The top figure shows the DSL storm, while the bottom two figures can be used along the DSL for two different situations.

Furthermore, as the DSL sinks as it spreads out considerable subsidence occurs which accounts for the marked clearing observed to occur within arc cloud lines.

In the formative stage of the arc cloud line's development, strong vertical motions within the cold air led to a mixed updraft in the region between the updraft maxima and cloud gap downdraft air. In the mature stage a strongly mixed updraft region was not observed, but rather the updraft above the DSL was characterized by a warm, moist and positively buoyant updraft core with only slight mixing evident: figure 5.5 is a good example of the type updraft encountered during the mature stage. To gain insight into differences exist in the updraft structure between the formative and mature stages, a hypothetical situation for the mature stage will be investigated. Consider the following situation:

1) a DSL 1500 meters deep;

2) a 2.05 mb pressure pertubation in the cold dome that decreases uniformly to zero at the top of the cold dome;

3) the speed of motion of the leading edge of the DSL is that of a density current, and the face of the DSL is assumed to be vertical;

4) the flow in the cold air may be calculated from Bernoulli's equation,and will be applied over 100 meter incremental steps;

5) frictional drag at the surface boundary decreases the velocity of the cold outflow air to equal the speed of the density current at the surface. The surface of frictional drag decreases linearly to zero at 400 meters height;

Figure 6.9 shows the horizontal velocity of the cool outflow air within the DSL and the resulting vertical motion field in the cool air due to convergence at the rear of the DSL for the above hypothetical situation. Although this situation is highly idealized, for example the same horizontal convergence occurring over a shorter distance will increase the vertical motion proportionally, it does give insight into why negatively buoyant DSL air was not encountered in the mature stage penetrations in the sub-cloud layer above the DSL. For example, based on equation 6.3, air that is negatively buoyant by 2°C (assuming $\bar{T}$ = 300°k) will only be forced above the DSL about one that 1 meter before its vertical motion is zero if its vertical motion is 31 cm sec^{-1} at the top of the DSL interface. If the vertical motion were an order of magnitude greater at the top of the DSL interface a nonmixing parcel would only reach a height of 74 meters above the DSL. In section 5.3.3 vertical motions in the cool outflow air were on the order of 5 m sec^{-1}: this would result in a DSL overshooting of 190 meters. Since most of the mature stage penetrations were within a few hundred meters of cloud base, it is understandable why strong negatively buoyant air was not encountered in the updraft, although some mixing along the DSL interface is required to account for the updraft structure shown in figures 5.5 and 5.7.

A composite picture of the arc cloud line's mature and dissipating stages may be developed based on the information in this subsection and from the research aircraft flights. These stages are depicted schematically in figure 6.10 for the mature stage and figure 6.11 for the dissipating stage.

velocity of cool
outflow air

$$\frac{V^2}{2} = \frac{\Delta P}{\rho}$$

velocity of DSL
interface

$$V^2 = \frac{k^* \Delta P}{\rho}$$

DSL depth, meters

Horizontal velocity, m sec^{-1}

DSL depth, meters

Vertical velocity, cm sec^{-1}
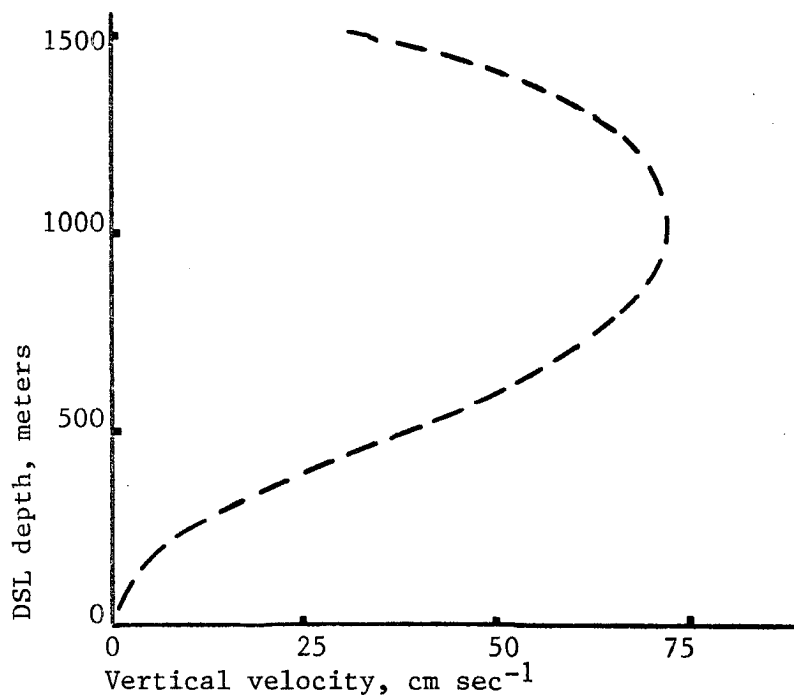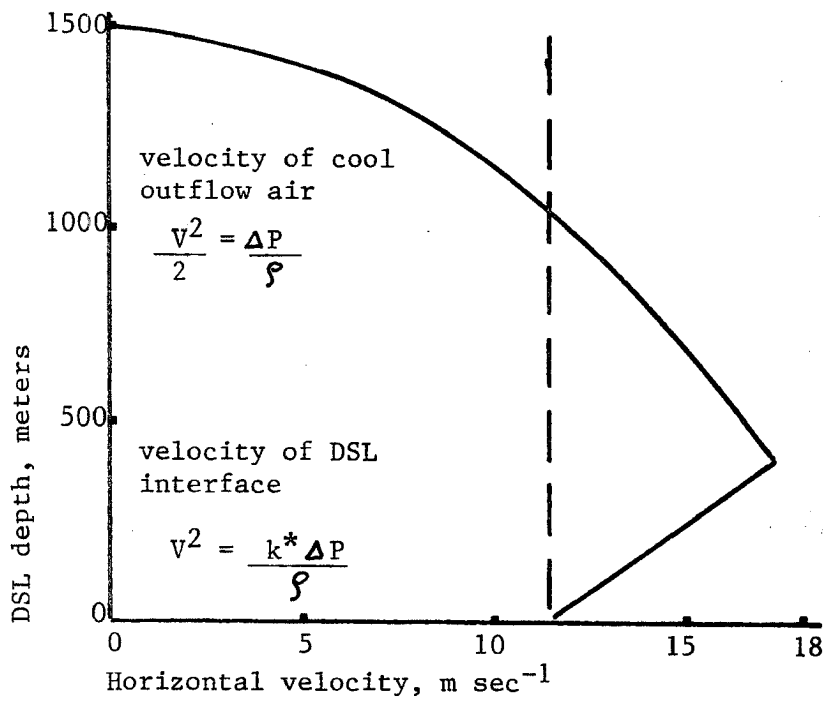
Figure 6.9. Idealized horizontal velocity and vertical motion profiles
in the mature stage of the DSL (See text for details).

In the mature stage, figure 6.10, the arc cloud line moves away from its parent source as a density current. As the arc cloud line matures and its parent storm begins to weaken the spe d of motion of the arc cloud line decreases as does the intensity of any solenoidal circulation present. Since the temperature gradient (approximately 1° to 2°C) across the DSL far from its parent storm is much less than one that is in close proximity to the storm, the corresponding mean velocities will also be less (approximately 2-3 m sec^{-1} in 200 sec). Thus, frictional forces must continue to play an important limiting role in the development of vertical motions within the DSL interface region. As the cold air source weakens the strength of the cold outflow jet decreases. This in turn decreases the convergence of cool outflow air into the rear of the DSL interface. With a decrease in convergence into the rear of the DSL, and a weakening of any solenoidal circulation present, the likelihood of vigorous mixing of negatively buoyant air from within the DSL interface into the arc cloud line updraft region decreases. Convergence in the warm environmental air due to the outwardly moving DSL results in the generation of a warm and moist positively buoyant updraft along the arc cloud line. Figure 5.5 is representative of the type updraft encountered during this stage of the arc cloud line's life cycle. The intensity and buoyant structure of this updraft region will be a function of the intensity of the arc cloud line and stability of the environment into which it is moving.

The dissipation stage and late mature stage of the arc cloud line's life cycle figure 6.11, are marked by a rapid continuation of its decrease in intensity. As the outflow's cold air source dissipates and the excess pressure in the cold dome decreases, the vertical motion
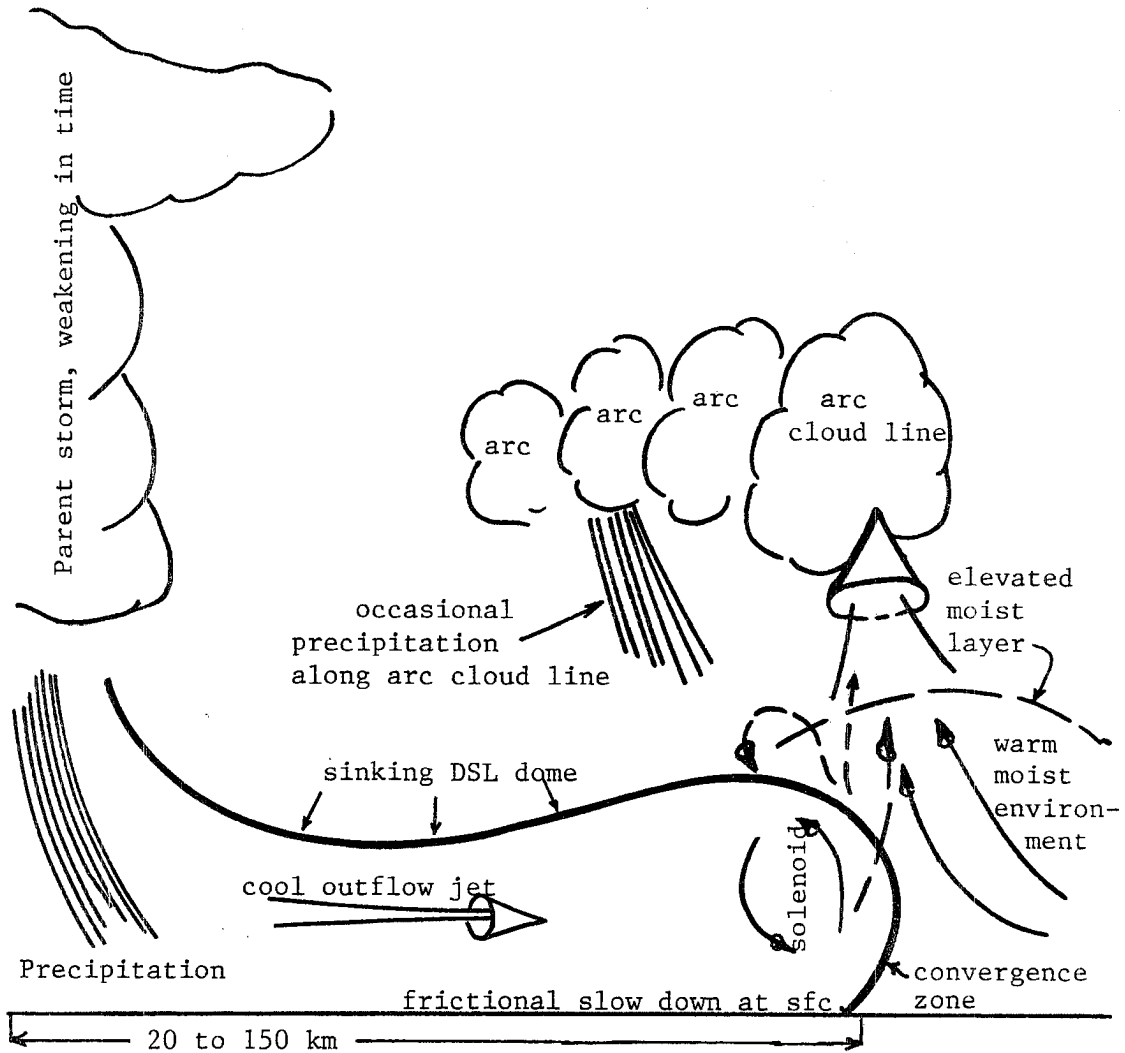
Figure 6.10. Schematic of mature stage. The arc cloud line is formed above the leading edge of the density surge line. The parent cold air source weakens as does the strength of the cool outflow jet. Occasional precipitation of moderate intensity falls from some of the convection along the DSL, locally strengthening the cold pool. The DSL is moving as a density current, forcing up the warm and potentially unstable environmental air along the DSL interface.

negatively buoyant
air overshoots its
equilibrium level

arc cloud line

Dissipated
Parent Storm

weakly
organized
updrafts

gradual subsidence
and clearing

Stationary
or slowly
moving DSL

gradually sinking air within
cool outflow, shallow DSL
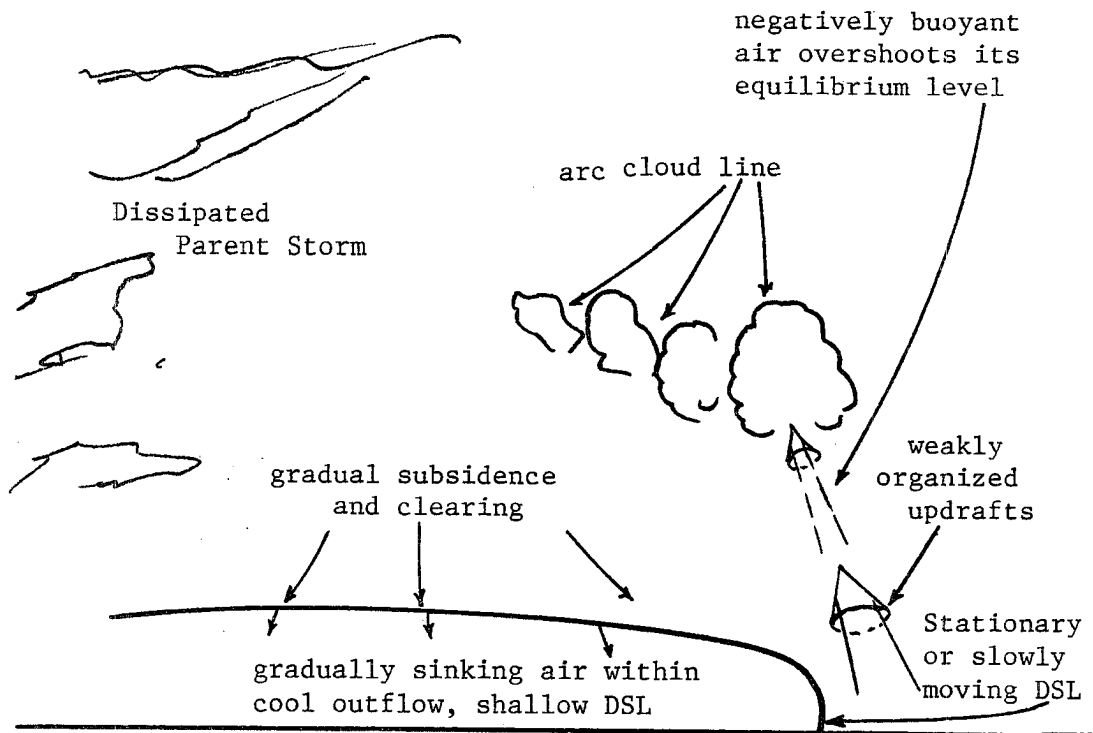
Figure 6.11. Schematic of dissipating stage. This stage is marked usually from above the DSL interface as negatively buoyant thermals overshoot their equilibrium level. This stage may regenerate depending on the stability of the airmass in which it is embedded.

field in the warm air forced by convergence along the DSL interface

will decrease. This may be seen by inspecting tables 6.3, 6.4 and 6.5

where it is apparent that once the DSL becomes shallow and slow

moving, only weak vertical motions are found in the convergence zone

along its leading edge. Figure 5.9 is representative of the type

updraft encountered during this final stage of the outflow's life

cycle. Along the arc cloud line relatively weak updraft cores exist

above the dissipating DSL. In some cases (as figure 5.9) these updraft

regions become negatively buoyant below cloud base. Although the

vertical forcing during this portion of the arc cloud line's life cycle

may be weak, if the environment is (or becomes) sufficiently unstable,

cumulus cloudiness or showers may still develop along the outflow arc.

In the next section, local scale differences in the air mass into

which an arc cloud lines advances will be investigated. By

understanding those differences, and the characteristics of the arc

cloud lines discussed in this section, it will be possible to explain

why convection is favored along an arc cloud line in one location and

not in another.

6.2   The Air in Advance of an Arc Cloud Line

Observations of convective scale interaction show that differences

in the cloud character of the air in advance of an arc cloud line are

of manifest importance to the development of new deep convective

activity. Thus, although there are a paucity of direct measurements

for cumulus versus clear regions, this section will investigate likely

differences in those regions.

There have been a variety of field research programs designed to study atmospheric variability on the mesoscale. Within the time frame of the geostationary satellite this includes programs such as NASA's Atmospheric Variability Experiment (AVE), the Severe Storm and Mesoscale Experiment (SESAME), the Cooperative Convective Precipitation Experiment (CCOPE) and the Kansas/Oklahoma PRE-STORM experiment. Those programs have been mainly concerned with the organization of the convective systems, mesoscale variability of the atmosphere on scales of tens of kilometers and a few hours, and the microphysics and structure of individual convective elements. There have been no large field research programs designed to study the difference between convective cloud and clear regions as detected in geostationary satellite imagery, although the aircraft observations of Sinclair and Purdom (1983, 1984) were designed to provide some insight into differences in those regions.

In visible satellite imagery, it is observed that over land in the afternoon, deep cumulus convection does not suddenly form, but rather develops in regions of pre-existing cumulus activity. This is in part due to the normal diurnal heating cycle that leads to stronger destabilization by mid-day than that which exists in the early morning hours. However, the development of cumulus over land depends on a variety of factors other than destabilization due to insolation. Low level moisture, terrain, surface characteristics, vertical wind shear and trajectory of the low level wind are but a few. In many instances, those mechanisms which are responsible for organized cumulus development, and eventual deep convection, are traceable to some type of differential heating mechanism. For example, with the land sea

breeze, the circulation causing the cumulus to form is well organized with vertical motions concentrated in the cumulus region, and sinking motion (with skies generally void of cumulus activity) concentrated in the area of the sea breeze's return circulation. It is of interest that mesoscale modeling results are showing that circulations that develop due to less well known differential heating catalysts, such as wet versus dry soil or cloudy versus clear skies, have an intensity comparable to that of the land sea breeze (Segal et al, 1986). Mechanisms other than those directly due to differential heating have been shown to lead to organized areas of upward motion and associated areas of sinking. For example, Kuettner (1959, 1971) showed that with the proper combinations of low level vertical wind shear and instability, roll vortices developed in which upward motions of a few meters per second were concentrated beneath cloud streets while sinking motion predominates in the clear region between the streets.

While direct observations of vertical motions with respect to cumulus versus clear distributions are few, LeMone and Pennell (1976) found vertical motions with deeper trade cumulus were generally greater than a meter per second at 80 meters below cloud base, while the corresponding clear regions generally had subsiding motions that were at times as great as 40 centimeters per second. The aircraft observations of Sinclair and Purdom (1983), which were taken over land, also showed upward motions on the order of a meter per second beneath cumulus cloudiness in the air ahead of the arc cloud line, and general disorganized sinking air in clear regions. Differences in the vertical motion fields associated with cumulus activity and corresponding clear

regions in the same local environment has also been demonstrated by Gray (1973). Gray showed, for the summertime tropical belt, that mass, moisture and energy balances required substantial vertical transports that had to be due to vertical circulations. He further showed that a substantial "up moist" and "down dry" circulation was accomplished by cumulus convection. The "up moist" portion of the circulation is accomplished directly by cumulus convection, while the "down dry" portion of the circulation is due to compensating subsidence in the clear air between the cumulus.

The local vertical transport of moisture aloft by cumulus is an important factor in pre-conditioning the atmosphere to locally accept deeper convective activity. In a study of non-precipitating cumulus convection, Betts (1973) showed that cumulus clouds change their immediate environment by moistening the entire cloud region while warming its lower portion and cooling it above. Esbensen (1978) showed that the primary role small cumulus played in the development of deep convection was through their moistening of the lower cloud layer. The above cited works correlate well with the direct observations of Jensen and Lenschow (1978) that show a direct correlation between penetrative convection and the local increase in height and moisture of the capping inversion. While whether or not growing non-precipitating cumulus directly warm or cool their local environment remains an open question, they do locally moisten the environment thus preconditioning it for deeper convective activity.

In a satellite image, the organized convective and clear regions in the air in advance of the arc cloud line reflect certain dynamic and thermodynamic features of that airmass. Pre-existing convergence and

vertical motion coupled with deep layer moistening in the cumulus regions, versus gradual subsidence in the clear regions, makes the cumulus regions more favorable for deep convective development if vertical forcing takes place. How may this be quantified? Present technology does not allow the direct measurement of convergence and vertical motion on local scales over large areas. However, certain information concerning the atmosphere's ability to utilize local scale forcing for the development of deep convection are detectable using satellite sounding data.

Sounding information from GOES/VAS can detect small and significant temporal variations in atmospheric temperature and moisture. The sounder's instrument characteristics that relate to vertical resolution are shown in table 2.1. From GOES-VAS sounding data we have: 1) near instantaneous observations through a column in the atmosphere; 2) moderate vertical resolution; 3) high spatial resolution (in the absence of clouds); 4) and one uniformly calibrated sensor making all of the measurements. With GOES-VAS, sounding data may be taken over an area the size of the United States at hourly intervals.

For many mesoscale applications, it is the gradient of atmospheric parameters and their change in time that is important. This is one area where the new observational data from VAS is helping lead to a better understanding of mesoscale atmospheric processes. The moisture structure of the atmosphere, both in the horizontal and vertical, has long been know to be an important factor in storm development (Doswell & Lemon, 1979), however, significant moisture variance exists within the mesoscale range at horizontal distances less than 100 km. Using

sounding information from polar orbiting satellites, Hillger and Vonder

Haar (1981) were able to extract moisture information at a much finer

resolution than was available using conventional data sources.   Similar

results concerning mesoscale moisture distribution have been

demonstrated using VAS data (Smith, et al, 1981; Petersen and Mostek,

1982).

Based on analyses of VAS satellite soundings, Zehr (1986) has been

able to show striking differences between airmasses on the mesoscale.

Figure 6.12 is a goes image over the central USA in June of 1984:   the

numbers within the image give the location of selected VAS soundings

for the time period just prior to the time of the image.   Notice that

sounding 23 is representative of an airmass modified by thunderstorm

outflow (it is within the cold dome) while sounding 32 is in air that

has not experienced thunderstorm activity.   VAS soundings at those two

locations are presented in figure 6.13.   Notice that although the VAS

information is presented for rather thick layers, the general

characteristics one should expect are evident - that is a cooler and

more stable low level airmass at location 23 versus that at location

32.   VAS sounding 63 is within the cooler air behind a slow moving cold

front that is pushing westward across Kansas while VAS sounding 59 is

in the more unstable air to its west.   These soundings are presented in

figure 6.14:   again the results appear as one should expect.   Soundings

similar to those presented here may be taken by VAS at hourly intervals

over cloud free areas of interest.   Those soundings contain information

on the atmosphere's thermal and moisture characteristics at a spatial

and temporal resolution never before available.   Purdom (1985) has

shown how adjacent satellite soundings, such as those presented above,
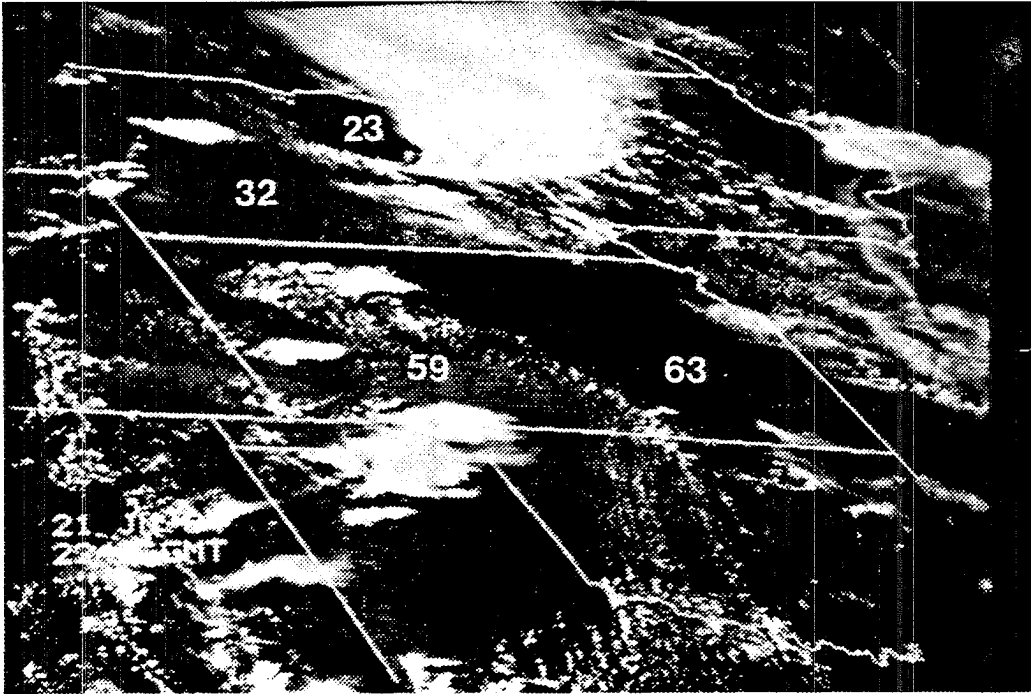
Figure 6.12. GOES-West 1 km visible image for 21 June 1984 at 2315 GMT. Numbers indicate locations of VAS soundings.
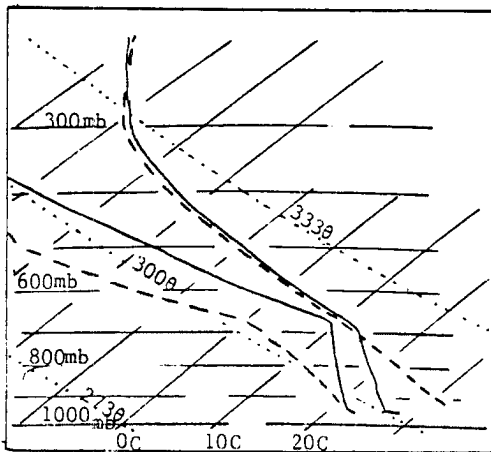
Figure 6.13. VAS soundings at locations 23 (T and T_d solid lines) and 32 (T and T_d dashed lines) in figure 6.12.
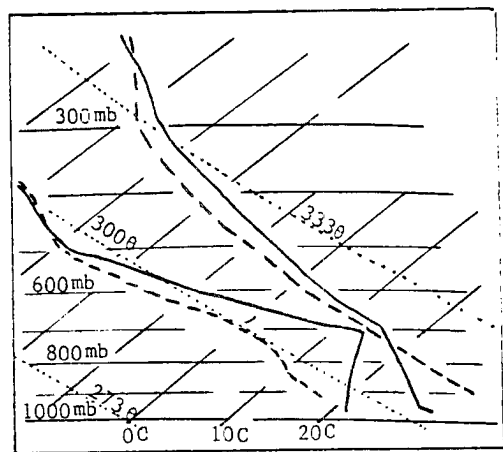
Figure 6.14. VAS soundings at locations 59 (T and T_d dashed lines) and 63 (T and T_d solid lines) in figure 6.12.

may be used to assess a local airmasses ability to support deep convection. Based on considerations of parcel buoyant energy, one may calculate a variety of parameters related to thunderstorm development and intensity. For example:

1) Positive Buoyant Energy - positive area between a local sounding's level of free convection (LFC) and equilibrium temperature;

2) Negative Buoyant Energy, surface to lifting condensation level (LCL) - amount of energy input required to lift a mixed parcel from the surface layer to condensation; and

3) Negative Buoyant Energy, LCL to LFC - amount of energy input required to lift a parcel from its LCL to its LFC.

One may assume that air in a convective region in advance of the arc cloud line reflects the local scale dynamics of that region, and consequently has already had sufficient energy input to reach its LCL. Furthermore, depending on the amount of cumulus development (cumulus to towering cumulus) some portion of the input energy required to attain free convection has also been realized. In the clear regions, on the other hand, energy input is still required for the first stages of cumulus development.

Purdom (1985) has shown that the differences of input energy required to overcome the amount of negatively buoyant air and attain free convection between clear and cumulus filled regions may be substantial. In figure 6.15, notice the differences shown in the satellite cloudiness shower in three regions: 1) the clear slot extending through southwest Georgia to the South Carolina border; 2) the cumulus cloud region immediately to the clear region's east which

Figure 6.15. TIROS visible image for 2100 GMT, 28 March 1984.
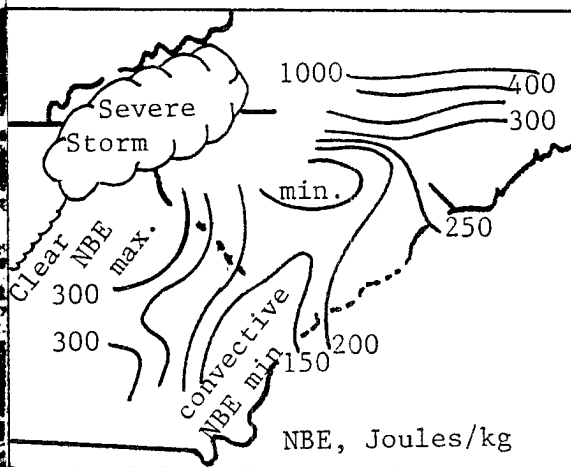
Figure 6.16. TIROS Negative Buoyant Energy (NBE) field.
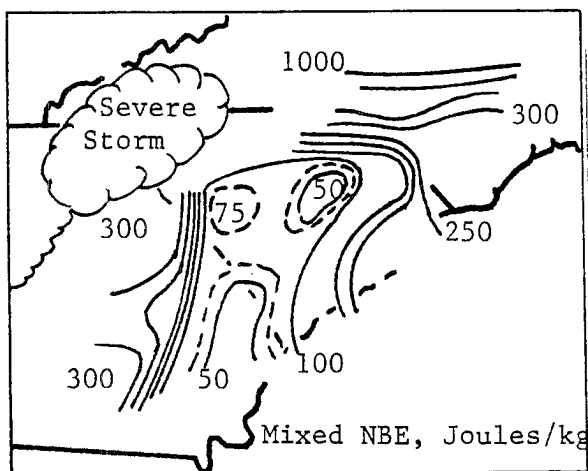
Figure 6.17. As figure 6.16 above, but with NBE between LCL and LFC in convective regions.
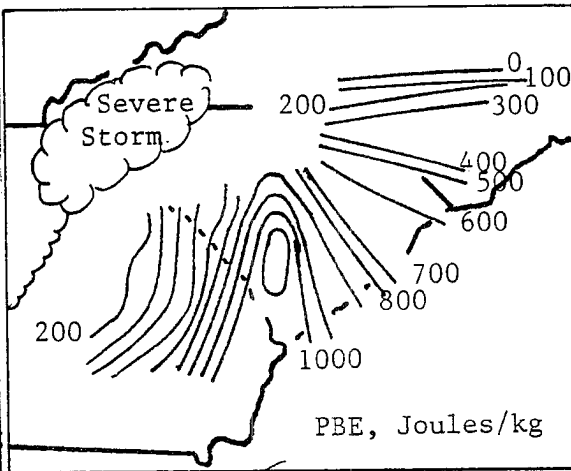
Figure 6.18. TIROS Positive Buoyant Energy field.

extends through southeast Georgia and well into central South Carolina

and 3) the clear region in South Carolina and North Carolina to the

north of an old thunderstorm outflow boundary. The image in figure

6.15 was taken by the NOAA-7 polar orbiting satellite. That satellite

also has an atmospheric sounding capability. A number of scientists

(Hillger et al, 1985, Purdom 1985, Hayden and Taylor, 1985) have used

sounding radiance from the NOAA-7 TIROS Operational Vertical Sounder

(TOVS) to compute temperature and water vapor profiles for the area

shown in figure 6.15, at a horizontal resolution of approximately 35 km

x 35 km. From each of those soundings, Purdom (1985) derived the

buoyant energy parameters previously mentioned in this section. Those

parameters, shown in figures 6.16 (total negative buoyant energy), 6.17

(negative buoyant energy LCL to LFC), and 6.18 (positive buoyant

energy), were used by Hillger et al (1985) and Purdom (1985) to explain

differences in convective development as the supercell in northeast

Georgia, figure 6.15, evolved on that day. In the negative buoyant

energy field, notice that the highest negative buoyant energies are

found in North Carolina to the north of the outflow boundary.

Differences in negative buoyant energy fields are also seen between the

air in Georgia versus that in the more central and southern parts of

South Carolina. Taking into account that much of the air in the

convective region has attained its lifting condensation level, allows

replacement of the total negative buoyant energy values in the cumulus

region with values of negative buoyant energy between the lifting

condensation level and the level of free convection. If this is done,

as shown in figure 6.17, a marked difference between the amount of

energy required to lift the air to free convection in central Georgia

versus the energy required in eastern Georgia and central and southern

South Carolina is readily evident. Furthermore, inspection of figure

6.18, which shows the distribution of positive buoyant energy, reveals

that the cumulus filled air in eastern Georgia and central and southern

South Carolina is much more suited for supporting intense convective

activity that the air in the clear region in Georgia or that air which

is to the north of the outflow boundary. Therefore one might surmise

from an analysis of the satellite sounding data that: 1) the air in

eastern Georgia and central and southern South Carolina is much more

sensitive to vertical forcing and free convective cloud development

than air within the other parts of the image; and 2) southern South

Carolina is much more suited to supporting intense convective activity

than air in the other regions. This helps explain the intensification

of the supercell storm that is located over northeast Georgia at the

time of figure 6.15 to tornadic and downburst proportions as it moved

into South Carolina, as well as the later development of the squall

line to the south of the supercell.

Through the combined use of satellite image and sounding data it

is possible to assess the convective potential of different portions of

a mesoscale airmass. In the next section, information from this

section and the previous section will be combined to help explain the

convective scale interaction phenomena.

6.3 Convective Scale Interaction

Based on aircraft and satellite observations, the previous two

sections of this chapter have explored the life cycle and dynamics of

the arc cloud line as well as differences in the thermodynamic

characteristics of the air into which it advances. That information

will now be used to bring into sharper focus the four properties of

convective scale interaction stated in section 3 of chapter 3.

Property #1

Thunderstorm outflow boundaries may maintain their
identity as arc cloud lines for several hours after they
have moved away from their parent source.

In the undisturbed convective environment, in advance of the arc

cloud line, small buoyant thermals rise from the surface boundary layer

and rapidly mix with the surrounding environment. Because of their

size and lack of organization and rapid mixing, they are unable to

sustain an updraft core and in most cases never reach the condensation

level; a few may produce short-lived fair weather cumulus. However, as

the outflow moves away from its parent thunderstorm, lifting occurs,

creating a new local environment in the vicinity of the density surge

line. This new local environment is much more favorable for the growth

of convective elements because of its organization, size and stronger

vertical motion field. Thus, the lifting of the relatively warm, moist

environmental air by the leading edge of the outflow leads to the

development of a warm buoyant updraft above the DSL which initiates the

development of the arc cloud line. For the arc cloud line to maintain

its identity for several hours requires that its parent energy source

provide a continuous outflow of cold air for maintenance of both the

DSL's depth and field of vertical motion (refer to figure 6.9 and its

discussion). Furthermore, rain showers are observed beneath some of

the cumulus congestus along the arc cloud lines. This precipitation/

evaporation process, and the production of new negatively buoyant air

behind the arc cloud line is important in maintaining its strength, and the ensuing regeneration of convective clouds along arc cloud lines.

Property #2   (Refer to figure 6.19)

The arc cloud line outflow boundary can, and often does, cause deep convection to develop along it at distances well over 150 km from its point of generation.

The ability of an arc cloud line to trigger new and vigorous convective development is a function of both the strength of the vertical motion generated along the leading edge of the DSL, as well as the stability of the environment into which the DSL is advancing.   As can be seen from tables 6.4 and 6.5, DSL's whose source gradually decreases in intensity are able to produce stronger vertical motions at greater depths than those whose source decreases rapidly in intensity. For example, referring to tables 6.4 and 6.5 the following comparisons may be made:

a) 81% source strength at 100 km gives a mean vertical motion of 3.87 m sec^{-1} at a height of 1.21 km

b) 64% source strength at 100 km gives a mean vertical motion of 2.73 m sec^{-1} at a height of 0.96 km

c) 49% source strength at 100 km gives a mean vertical motion of 1.84 m sec^{-1} at a height of 0.74 km

d) dissipated source at 100 km gives a mean vertical motion of 0.68 m sec^{-1} at a height of 0.32 km

Thus, given similar local environments (same stability) into which arc cloud lines advance, the more vigorous their parent source remains,the more capable a DSL is of forcing parcels to greater vertical depths.   However, it should be recognized that the vertical forcing along a mature arc cloud line's DSL is relatively weak: for example, assuming no mixing, an initial vertical motion of 3.87 m sec^{-1}
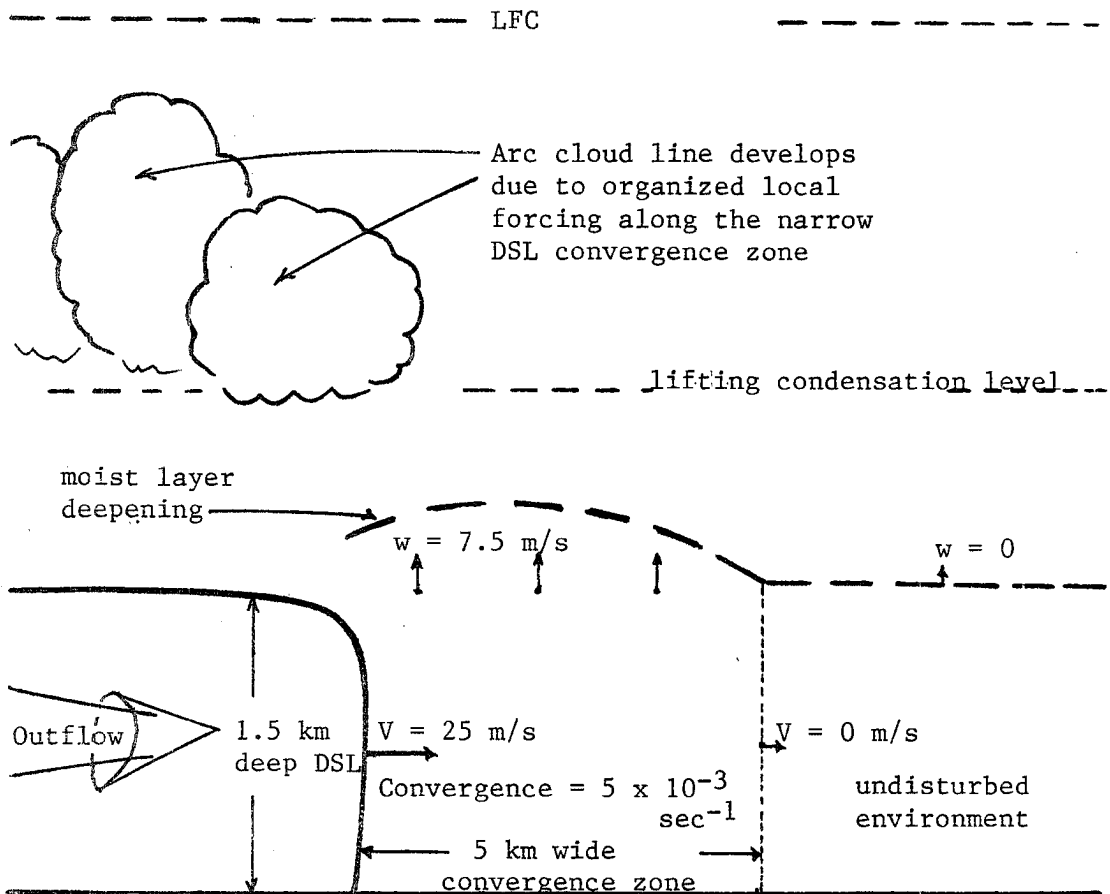
Figure 6.19. Schematic of convective development along an arc cloud
line. The strength of the convection that develops along the arc
cloud line depends on how much of the negative buoyancy between the
top of the DSL and the level of free convection (LFC) is able to be
overcome by vertical motion generated in the narrow convergence zone.

is only capable of overcoming a mean negative buoyancy of 1° C at ($\bar{T}$ = 295°C) over a vertical depth of 225 meters. Thus, for deep convective development along an arc cloud line to be as dominating an influence on deep convective development as is indicated by figure 4.13, some other factors must be taken into account. These other factors are discussed in properties #3 and #4 which follow.

Property #3   (Refer to figure 6.20)

Deep convective development along an outflow boundary
is a selective process - it only occurs where the arc
cloud line merges with a cumulus region or intersects
another boundary. When the arc cloud line moves into
clear skies no deep convection develops.

Merger is defined to occur when an arc cloud line moves into a region of pre-existing cumulus and cumulus congestus cloudiness and triggers new deep convective storms. As was pointed out when discussing property #2, the ability of an arc cloud line to trigger new vigorous convection is a function of both the strength of the vertical motion along the leading edge of the DSL, as well as the stability of the environment into which the DSL is advancing. The DSL/outflow boundary moves into the environment ahead of it with a relatively narrow and concentrated band of vertical motion occurring along its leading edge. The strength of this organized band of vertical motion generally decreases in time: this helps explain the radius of interaction results, figures 6.7a and 6.7b, which show that arc cloud lines are most effective in forcing new deep convection early in their life. Furthermore, the air mass into which an arc cloud line moves is in no way uniform in its ability to support new deep convection. Such

LFC

New strong
convection develops
due to arc merger
with cumulus region

LCL

Depth of remaining
negatively buoyant
layer

Cumulus
Region

Cumulus
Region

w = 7.5 m/s

w > 0

Outflow

1.5 km
deep DSL

V = 25 m/s

Convergence = 5 x 10^{-3}
sec^{-1}

5 km wide
convergence zone

V=0

Pre-existing
convergence ahead
of outflow, w > 0
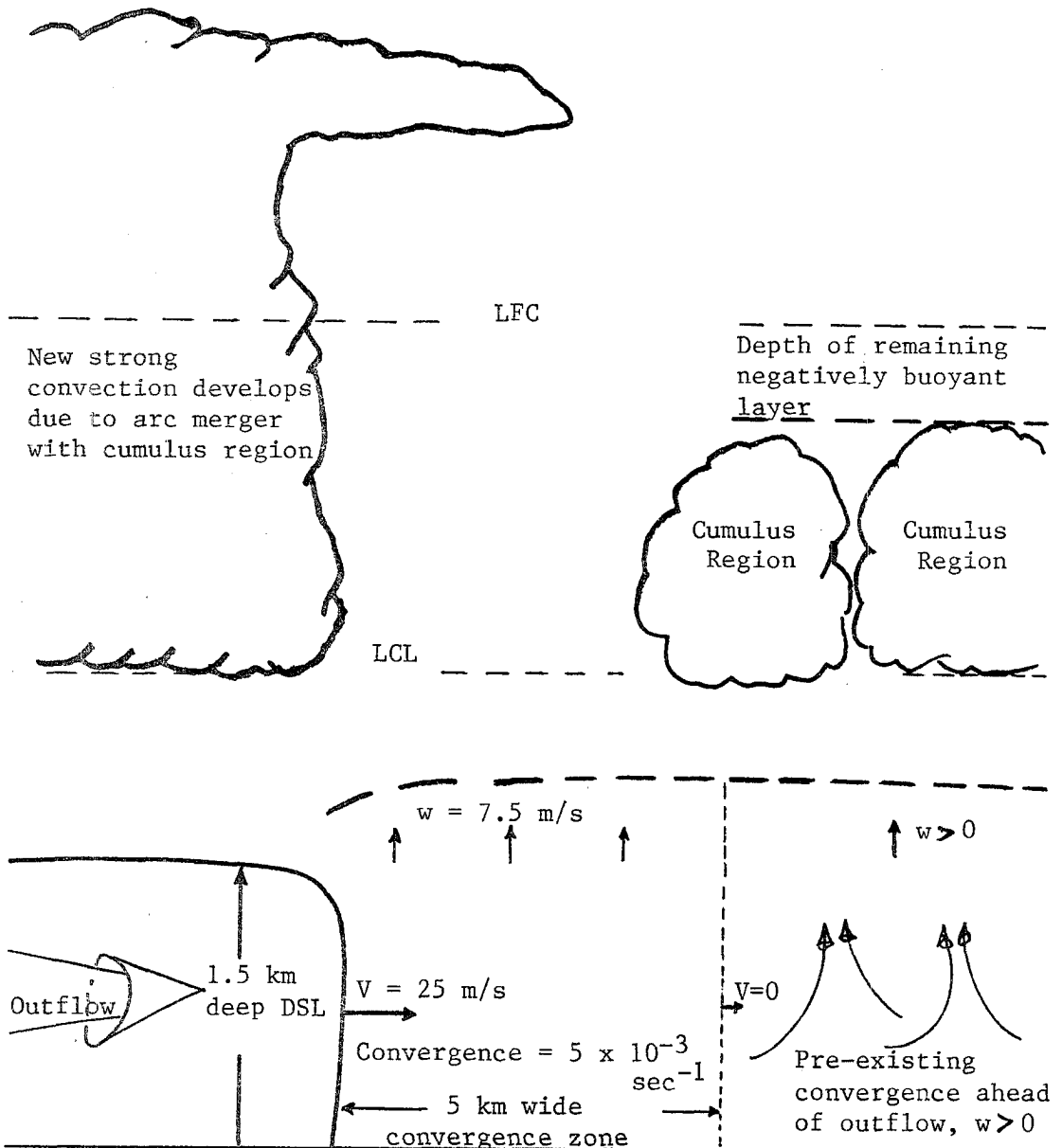
Figure 6.20. Schematic of strong convective development along an arc
cloud line due to merger with a pre-existing cumulus region. Due to
convergence in the environment ahead of the arc cloud line, a region
of organized cumulus convection develops. Those cumulus represent a
region where some of the vertical motion required to overcome the
the negative buoyancy in the environment between the lifting condensa-
tion (LCL) and level of free convection (LFC) has already been
realized. Therefore, the vertical motion generated along the narrow
convergence zone in advance of the arc cloud line's DSL is able to
force the less stable air in the cumulus region to deep convection.

an environment already exhibits a certain amount of convective

organization. As the arc cloud line moves into a cumulus filled

region, it provides a band of organized vertical motion to a relatively

moist and locally unstable (as shown in figures 6.17 and 6.18) airmass.

Thus convective scale interaction due to merger with pre-existing

convection often leads to the development of new cumulonimbus which in

turn reinforces the cold pool which is driving the arc cloud line's

DSL. On the other hand, as the arc cloud line's DSL moves into a clear

region it encounters air that is stable with respect to that in a

cumulus region. When the arc cloud line's DSL interacts with that air,

it produces cumulus cloudiness along its leading edge as in property

#1. Taking into account the normal diurnal heating cycle and its

influence on convective development helps explain the strong influence

merger imposes on new deep convective development in the noon to 4pm

time frame as is shown in figure 4.8.

Property #4   (Refer to figure 6.21)

As the cumulus regime evolves on a given day, and much
of the cumulus field dies away, the majority of new
thunderstorms are confined to arc cloud line intersection
points.

Intersection is defined to occur when two arc cloud lines come

into direct contact and trigger new deep convective storms. As the two

arc cloud lines approach one another, increasing convergence between

them results in a deeper moist layer. As two arc cloud lines

intersect, a greater degree of organization and stronger forcing of the

boundary layer's vertical motion field occurs (as compared to a single

are cloud line). This causes the development of a highly organized and

strong buoyant updraft at the location of the intersection. It is the
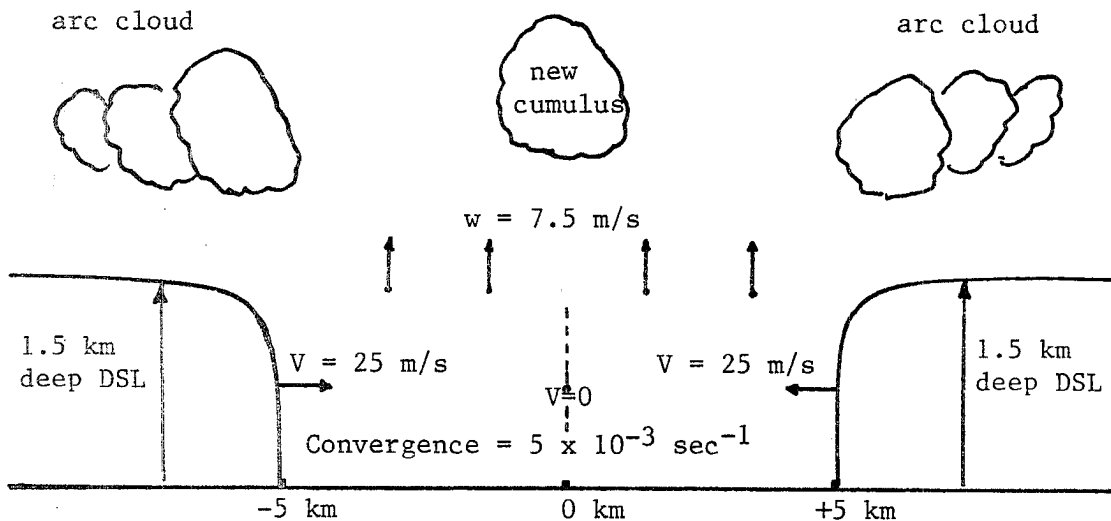
A. Intersection begins, arc cloud lines 10 km apart
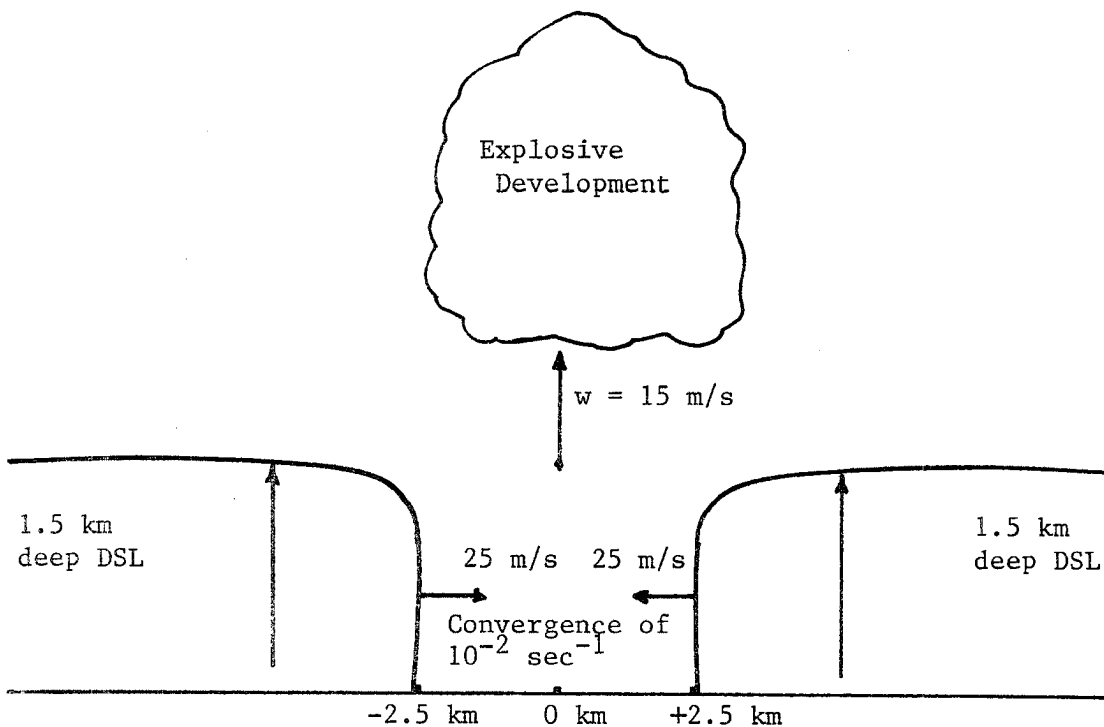
B. Intersection continues, arc cloud lines 5 km apart.

Figure 6.21. Schematic of convective development due to arc cloud lines intersecting one another. A narrow and concentrated region of upward vertical motion develops as Intersection occurs. This is one of the reasons that storms (and their updrafts) that develop at intersection points tend to move in the direction of the moving intersection point, as shown in figure 3.5.

formation of these highly organized and strong buoyant updrafts that lead to the development of intense thunderstorms at points of arc cloud line intersection. As with property #3, the dominating influence that the intersection mechanism imposes on new deep convective development late in the diurnal cycle may be seen by inspecting figure 4.8. Since the late afternoon is a time of cumulus dissipation and stabilization, arc cloud line intersection areas naturally become the most suited regions for new deep convective development.

7.0 SUMMARY AND CONCLUSIONS

7.1 General

This paper uses satellite data and research aircraft data to

provide new understanding concerning the mesoscale development and

evolution of deep convection in an atmosphere typified by weak synoptic

scale forcing. The major topic covered is the dominating role that

convective scale interaction (Purdom, 1979) plays in locally forcing

the development and evolution of deep convection. Convective scale

interaction manifests itself through the merger and intersection of

thunderstorm produced outflow boundaries (arc cloud lines) with other

convective lines, areas or boundaries. The local convergence that

occurs along these arc cloud lines is on the order of 10^{-2} to 10^{-3}

per second.

These findings concerning convective development under weak

synoptic forcing fit well into the broader context of convective

development accompanied by strong vertical forcing. For example,

Newton (1966) pointed out the symbiotic relationship between an intense

thunderstorm's updraft and downdraft in maintaining that storm's

structure in a sheared environment. Maddox (1980) related the

importance of the large mass of rain-cooled air and resulting outflow

boundary development to the life cycle of mesoscale convective

complexes. Gray (1973) showed the need for a substantial up-moist and

down-dry vertical circulation and the importance of recycling due to

cumulus convection in the maintenance of tropical cloud clusters.

Frontal zones and squall lines have long been recognized as

regions where vertical forcing is localized. Tepper proposed (1950)

and later developed a simple "pressure jump" model (1955) to explain

the localized vertical forcing necessary for squall line and convective

development. Fujita (1955), pointed out that most of Tepper's

"pressure jumps" were actually the result of large thunderstorm high

pressure systems caused by the squall line thunderstorms.

Fujita (1955) also pointed out that mechanical forcing was

important in maintaining the squall line. Similar results concerning

the importance of mechanical forcing (rather than buoyant) were found

by Browning and Harold (1970) concerning convection along a cold

frontal zone. A study of Carbone (1982) showed that convergence in

a narrow zone on the order of 10^{-2} to 10^{-3} sec^{-1} was responsible for

convective development along a narrow cold frontal rain band. Similar

results were found by Shapiro et al. (1985) in a mesoscale study of a

nonprecipitating Colorado cold front. An interesting feature of the

studies of Carbone (1982) and Shapiro et al. (1985) is that they related

the speed of movement of those phenomena to that of a density current.

The information and findings in this presentation are based on

three separate but closely related efforts. They are:

1) the discovery of the convective scale interaction (csi)

process based on geostationary satellite observations, and an

investigation of csi's effects on thunderstorm development and

evolution;

2) an analysis of the arc cloud line phenomena using data from a series of focused field research programs specifically designed to combine research aircraft data with geostationary satellite data; and,

3) the development of a physical model to describe the convective scale interaction process.

7.2 Satellite Related Findings

Convective scale interaction is directly associated with outflow boundaries produced by precipitating convective storms. Until recently such interactions had only been observed using animated geostationary satellite imagery. There are a number of reasons for this; foremost among them:

a) routine surface observational spacing is far too coarse for mesoscale meteorological studies, compare to geostationary satellite imagery which offers a 10^6 improvement in resolution; and,

b) operational noncoherent radar lacked the power (Wilson and Carbone, 1984), resolution and network spacing density required to routinely observe arc cloud lines.

A number of examples of the arc cloud line and the convective scale interaction phenomena were presented in chapter 3. Based on those observations, four important properties of arc cloud lines and convective scale interaction were presented. Restated below, they served as the impetus for the remainder of the work undertaken in this paper.

#1. Thunderstorm outflow boundaries may maintain their identity as arc cloud lines for several hours after they have moved away from their parent source.

#2. The arc cloud line outflow boundary can, and often does, cause deep convection to develop along it at distances well over 150 km from its point of generation.

#3. Deep convective development along an outflow boundary is a selective process - it only occurs where the arc cloud line merges with a cumulus region or intersects another boundary. When the arc cloud line moves into clear skies no deep convection develops.

#4. As the convective regime evolves on a given day, and much of the cumulus field dies away, the majority of the new thunderstorms that develop are confined to arc cloud line intersection points.

Because of the apparent dominance of convective scale interaction in controlling deep convective development, a study was undertaken to determine its relative importance in new storm generation and ensuing rainfall. Using satellite visible and infrared data, Purdom and Marcus (1982) classified new storm development and intensity as a function of storm generation mechanism over the southeast United States. Results show (section 4.3) that convective scale interaction is the primary cause for afternoon thunderstorm development over that region of the country, being responsible for 85 to 90 percent of the more intense convective storms (tops colder than $-42^\circ C$) that are active by late afternoon (6 p.m. local time): see figure 4.9. Furthermore, when the convective activity is correlated with heavy rainfall occurring during the same period, it is apparent that an overwhelming majority of the measured summertime rainfall is produced by storms that have been triggered through convective scale interaction (figure 4.12). It is because of convective scale interaction that the majority of the summertime rainfall occurs over the southeast United States. To account for the deep convection and rainfall that occurs over the southeast United States, the thunderstorm activity that results from

normal diurnal differential heating must be augmented by new storms produced through convective scale interaction. This finding helps answer a question indirectly posed by Lopez (1972) when he observed: "Evidently a strong dynamic forcing in the sub-cloud layer is necessary to develop any deep cumulus convection... The precise mechanism by which the synoptic boundary layer convergence is concentrated into smaller areas of intense inflow under the clouds is not well understood."

7.3 Aircraft Related Findings

Because of the importance of arc cloud lines in the development of deep convection and its ensuing rainfall, a series of focused field research programs were undertaken. In those programs, designed to study the arc cloud line phenomena, research aircraft data were taken in conjunction with three minute interval GOES data (Sinclair and Purdom, 1983, 1984). This was the first time that an experiment to obtain in-situ research aircraft measurements of a satellite observed mesoscale phenomena had been undertaken. Only through careful planning was it possible to go to the field with confidence that well defined experimental goals would be met. The success in meeting the experimental goals indicates the dedication of those involved in the planning and execution of this effort. Work continues in the investigation of arc cloud lines using research aircraft data and geostationary satellite data in coordination with the MIST (MIcroburst and Severe Thunderstorm) program to be undertaken in the Huntsville, Alabama area during the summer of 1986.

The aircraft used in the investigations was a Cessna Turbo 207, which was specially instrumented to provide direct measurements of

temperature, dew point, pressure and the atmosphere's three dimensional velocity field. The flights were the first specifically designed to employ a research instrumented aircraft to investigate the arc cloud line phenomena. The major experimental goal for the aircraft flights was to investigate the dynamic and thermodynamic characteristics of arc cloud lines in three critically important regions. Those regions (refer to figure 5.2) were: 1) within the cool outflow region between the parent storm and the arc cloud line's density surge line (DSL) interface; 2) the DSL interface region between the cool outflow air and the relatively warm environmental atmosphere, and, 3) the updraft region below the base of the arc cloud line's cumulus cloudiness and above the top of the DSL. Based on the aircraft observations, the following information concerning the three regions (figure 5.2) was deduced:

A) Region 1 (cool outflow, refer to figure 5.9):

1. Subsidence was found at all levels below cloud base, once penetrations were a few kilometers within the DSL or the region above it. This leads to a more stable cloud form (debris) above the DSL, and if sinking is sufficiently vigorous, clearing skies develop above the DSL.

2. A cold outflow leads to strong convergence at the DSL and undisturbed environment interface. This helps account for the updraft region within the cold air behind the DSL interface.

3. Precipitation along the outflow arc contributes to negatively buoyant air within the outflow boundary. This

helps the arc maintain its identity in the absence of strong thunderstorm activity.

B) Region 2 (interface region, refer to figure 5.13):

1. A solenoidal circulation exists within the DSL. This supports the updraft circulation within the cold air just behind the DSL frontal surface.

2. The lifting of warm environmental air by the cold outflow air gives rise to a significant vertical motion field just ahead of the arc-line gust front.

C) Region 3 (arc line cloud base region, refer to figure 5.14):

1. Except in the late stages of the DSL's life, a strong warm moist updraft core exists beneath the arc cloud line. Descending motion is evident around the main updraft region.

2. The strong turbulence and shear across the DSL interface contributes to a modified updraft structure that feeds the cumulus clouds of the arc cloud line.

The lateral extent of the vertical motion field along the DSL compared to the cloud scale indicates that the main driving force for the initial cloud development along the arc-line is controlled by the thunderstorm outflow(s) interacting with the convectively unstable air of the environment. This initiating process appears to be sufficient in nature to control the maintenance of the updraft region above the DSL to cloud base strictly on the initial momentum field generated near the outflow interface. That is, the buoyancy field appears to act as a secondary energy source for the initiation of the updraft region below the arc cloud line.

Research aircraft measurements of the type undertaken in this study of arc cloud lines are extremely important for developing a better understanding of mesoscale meteorological phenomena observed using satellite data. While the geostationary satellite allows meteorologists to observe convective development on space and time scales compatible with the mechanisms responsible for their development, those observations do not provide the detailed in-situ measurements required for physical understanding. It is only through the use of a research aircraft that such in-situ information may be obtained. The importance of integrating research aircraft data with satellite observations cannot be overstated. Through such an effort the dominant factor (previously unrecognized) influencing deep convective development over the southeast United States has been investigated. Without the integration of research aircraft data with satellite data this would not have been possible. There are a variety of mesoscale meteorological phenomena awaiting similar exploration!

7.4 Physical Model Results

Based on satellite and research aircraft observations, three stages of the arc cloud line's life cycle have been defined. Those stages are the formative stage, the mature stage and the dissipating stage. The three stages of the arc cloud line's life cycle were found to be most readily distinguished, one from the other, by their link to their parent source.

The formative stage of the arc cloud line's life cycle is characterized by a highly channeled storm outflow. Within the cold outflow air, convergence of high momentum air into the rear of the DSL interface along with the development of a solenoidal circulation and

dynamic pressure forces leads to organized vertical motions within that

negatively buoyant air. The lifting of warm environmental air by the

cold outflow air, as well as possible dynamic pressure forces, gives

rise to a significant vertical motion field just ahead of the arc-line

gust front. Mixing of air from within the density surge line, DSL,

with the warm and more unstable air ahead of it contributes to a

modified updraft structure that feeds the cumulus clouds along the arc

cloud line. Figure 5.11 is representative of the vertical circulations

one should expect to encounter during the late formative stage of an

arc cloud line's life cycle.

As the formative stage evolves to the mature stage, the DSL

becomes well established and moves out from the parent storm as a

density current. During this stage of the arc cloud line's life cycle

it may move over 100 km from its parent source and continue to trigger

new deep convection. As the arc cloud line matures, and its parent

storm begins to weaken, the speed of motion of the arc cloud line and

depth of its DSL begin to decrease. Since both of those factors are

important in determining the amount of low level convergence generated

along an arc cloud line's DSL, the rate of dissipation of the parent

storm becomes an important factor in a DSL's ability to generate new

deep convection. Furthermore, as the DSL sinks and spreads out as it

advances into the warmer environment ahead of it, considerable

subsidence occurs within the cool air; this accounts for the marked

clearing observed to occur within the interior portion of mature arc

cloud lines. As the parent storm weakens during the mature stage, so

does the strength of the cool outflow jet and any solenoidal

circulations present. With a decrease of convergence into the rear of

the DSL, and a weakening of any solenoidal circulation present, vigorous mixing of negatively buoyant air from within the DSL interface region into the arc cloud line updraft region decreases. Convergence in the warm environmental air due to the outwardly moving DSL results in the generation of a warm and moist positively buoyant updraft region beneath the arc cloud line. Figure 5.5 is representative of the type updraft encountered during the mature stage.

The dissipation stage of the arc cloud line begins with the dissipation of its parent source, the thunderstorm downdraft. During the dissipating stage, the DSL becomes shallow and slow moving with only weak vertical motions found in the convergence zone along its leading edge. Figure 5.9 is representative of the type updraft encountered during the dissipating stage. Although vertical motions are weak during this portion of the arc cloud line's life cycle, if sufficient instability exists in the warm environment, cumulus cloudiness or deep convection may still develop.

Based on aircraft data, satellite imagery and satellite sounding data, significant differences were found in the ability of a mesoscale air mass to support deep convective development due to vertical forcing. In a satellite image, the organized convective and clear regions in the warm environment in advance of an arc cloud line reflect the dynamic and thermodynamic characteristics of that region. Pre-existing convergence and vertical motion coupled with deeper layer moistening in the cumulus regions, versus the clear regions, make the cumulus regions more favorable for deep convective development if vertical forcing occurs. These mesoscale air mass differences can be detected using satellite sounding data.

Knowledge concerning the stability of a local air mass and the vertical forcing along an arc cloud line's density surge line are important elements in the understanding of the convective scale interaction phenomena. In the undisturbed convective environment, in advance of the arc cloud line, small buoyant thermals rise from the surface boundary layer and rapidly mix with the surrounding environment. As the outflow moves away from its parent thunderstorm, lifting occurs, creating a new local environment in the vicinity of the density surge line. Thus, the lifting of the relatively warm, moist environmental air by the leading edge of the outflow leads to the development of a warm buoyant updraft above the DSL which initiates the development of the arc cloud line. For the arc cloud line to maintain its identity for several hours requires that its parent energy source provide a continuous outflow of cold air for maintenance of both the DSL's depth and field of vertical motion. In addition, rain showers are observed beneath some of the cumulus congestus along arc cloud lines. This precipitation/evaporation process, and the production of new negative buoyant air behind the arc cloud line is an important factor in maintaining its strength.

The ability of an arc cloud line to trigger new and vigorous convective development is a function of both the strength of the vertical motion generated along the leading edge of the DSL, as well as the stabililty of the environment into which the DSL is advancing. DSL's whose parent cold air source gradually decreases in intensity are able to produce stronger vertical motions at greater depths than those whose parent cold air source rapidly dissipates. The DSL/outflow boundary moves into the environment ahead of it with a relatively

narrow and concentrated band of vertical motion occurring along its leading edge, figure 6.19. The air mass into which an arc cloud line moves is in no way uniform in its ability to support new deep convection. As the arc cloud line moves into a cumulus filled region, figure 6.20, it provides a band of organized vertical motion to a relatively moist and locally unstable airmass. Thus convective scale interaction due to merger with pre-existing convection often leads to the development of new cumulonimbus which through new precipitation and evaporative cooling reinforces the pressure gradient force which is driving the arc cloud line's DSL. As the two arc cloud lines approach one another, increasing convergence between them results in a deeper moist layer. As two arc cloud lines intersect, figure 6.21, a greater degree of organization and stronger forcing of the boundary layer's vertical motion field occurs (as compared to a single arc cloud line). This causes the development of a highly organized and strong buoyant forced updraft at the location of the intersection. Since the late afternoon is a time of cumulus dissipation and stabilization, arc cloud line intersection areas naturally become the most suited regions for new deep convective development.

7.5 Implications

A number of important implications may be drawn from the above results. Several are listed below.

A) Nowcasting.

Geostationary satellite data will become one of the major footings upon which mesoscale forecasting programs of the future are based. By combining satellite data with more conventional data, such as radar and

surface observations, many of the features important in mesoscale
weather development and evolution may be better analysed and
understood. This improved analysis and understanding of mesoscale
processes is necessary if very-short-range forecasting is to be
successful.

A certain amount of success has already been realized in the
nowcast area through the use of satellite data at the National Severe
Storm Forecast Center (NSSFC). For example, using the concept of
convective scale interaction, NSSFC forecaster's placed a remarkably
accurate tornado watch over the Carolinas on March 28, 1984, see figure
3.9.

B) Thunderstorm life cycle

We must rethink what is meant by thunderstorm life cycle. This
does not mean that previous models of life cycle are incorrect.
Rather, those models need to be expanded in light of these new
observations, especially insofar as a storm's arc cloud line's
interactions with the environment are concerned. Such interaction may
occur at great distances from the parent storm, and even after the
parent thunderstorm has dissipated.

C) Weather Modification

Seeding strategies must be developed to take advantage of the arc
cloud line merger and intersection mechanisms. If an intense storm's
lifetime is able to be extended, its cold outflow will remain stronger.
Extending a storm's lifetime would increase its outflow's longevity and
intensity, and thus its chances to trigger new deep convection.

Furthermore, early in the day, organized convective areas should be targeted for seeding because of their merger potential.

Information in satellite imagery can be used to reduce the inherent noise in weather modification programs by improving short term prediction (nowcasts) of favored areas for seeding. Surprisingly, the satellite data may prove most useful in retrospective analysis to determine true cause-and-effect relationships and help move the assessment analysis from its noisy statistical world.

D) Future Mesoscale Field Experiments

High-resolution satellite data from GOES is helping to open the door for a new era in mesoscale meteorology. Many of the mesoscale processes important in the initiation and maintenance of convection are readily detectable in the imagery. By combining research aircraft data with GOES data mesoscale processes in the atmosphere can be analysed and more fully understood.

By early 1990, a truly new era of mesoscale meteorology will begin with the advent of an impressive array of meteorological sensors. They include the GOES-NEXT satellites, NEXRAD Doppler radar networks, upper air wind profiler arrays and the next generation of TIROS polar orbiting satellites. Mesoscale observations previously requiring special networks will routinely be available. The use of research aircraft in focused field programs should become routine.

E) Mesoscale Modeling

If forecast from mesoscale numerical models are to be locally specific, those models must be able to handle an individual

thunderstorm's life cycle. This must include thunderstorm precipitation and sub-cloud evaporation for outflow boundary production. In addition, the models must be able to predict the natural evolution of local circulations that develop in a warm sector.

F) Mesoscale Meteorology

Geostationary satellite data is leading the way for a golden age in mesoscale meteorology. Prior to meteorological satellites the mesoscale was a data sparse region. The geostationary satellite has the unique ability to frequently observe the atmosphere (sounders) and its cloud cover (visible and infrared) from the synoptic scale down to the cumulus scale. This ability to provide frequent, uniformly calibrated data sets over a broad range of meteorological scales places the geostationary satellite at the very heart of understanding mesoscale weather development. By combining satellite data with conventional meteorological data, many of the features important in mesoscale weather development and evolution may be better analyzed and understood. This is especially true when a field program may be focused to study a particular phenomena, as was the case in this paper where satellite data were integrated with research aircraft data.

8.0 REFERENCES

Achtemeier, G.L., 1983: The relationship between the surface wind field and convective precipitation over the St. Louis area. J. Clim. and Appl. Meteor., 22, 982-999.

Adler, R.F. and D.D. Fenn, 1977: Satellite based thunderstorm intensity parameters. Preprints, 10th Conf. on Severe Local Storms, Omaha, Amer. Meteor. Soc., 8-15.

Adler, R.F. and D.D. Fenn, 1979: Thunderstorm intensity as determined from satellite data. J. Appl. Meteor., 18, 502-517.

Barnes, S.L., (ed.), 1979: SESAME 1979 Data User's Guide. NOAA/ERL, U.S. Department of Commerce, Boulder, CO, 236 pp.

Bartels, D., J.M. Skradski and R.D. Menard, 1984: Mesoscale Convective Systems: A satellite data based climatology. NOAA-TM ERL ESG-6, NTIS#PB85-187862, 58 pgs.

Benjamin, T.B., 1968: Gravity currents and related phenomena. J.Fluid Mech.,31, 209-248.

Betts, A.K., 1973: Non-precipitation cumulus convection and its parameterization. Quart. J. Roy. Meteor. Soc., 99, 178-196.

Betts, A.K., 1976: The thermodynamic transformation of the tropical subcloud layer by precipitation and downdrafts. J. Atmos. Sci., 33, 1008-1020.

Bohan, W.A., 1981: The importance of thunderstorm outflow boundaries in the development of deep convection. WAB 456, 16mm color sound movie, The Walter A. Bohan Co., 2026 Oakton Street, Park Ridge, IL, 29 minutes.

Brandes, E.A., 1978: Mesocyclone evolution and tornadogenesis: Some observations. Mon. Wea. Rev., 106, 995-1101.

Browning, K.A., 1964: Airflow and precipitation trajectories within severe local storms which travel to the right of the winds. J. Atmos. Sci., 21, 634-639.

Browning, K.A., 1982: Nowcasting, Academic Press Inc., London, New York (U.S. edition), 256 pp.

Browning, K.A., and T.W. Harrold, 1970: Air motion and precipitation growth at a cold front. Quart. J. Roy. Meteor. Soc., 96, 369-389.

Byers, H.R. and R. Braham, 1949: The thunderstorm. Government Printing Office, Washington, DC, 287 pp.

Caracena, F., R.A. Maddox, J.F.W. Purdom, J.F. Weaver and R.N. Green, 1983: Multi-scale analyses of meteorological conditions affecting Pan American World Airways Flight 759. NOAA-TM ERL ESG-2, NOAA/ERL, Boulder, CO, 53 pp.

Carbone, R.E., 1982: A severe frontal rainband. Part I: Stormwide hydrodynamic structure. J. Atmos. Sci., 39, 258-279.

Changnon, S.A., 1976: Effects of urban areas and echo merging on radar echo behavior. J. Appl. Meteor., 15, 561-570.

Charba, J., 1974: Application of gravity current model to analysis of squall-line gust front. Mon. Wea. Rev., 102, 140-156.

Crowson, D.L., 1949: Cloud observations from rockets. Bull. Amer. Meteor. Soc., 30, 17-22.

Davies-Jones, R.P., 1974: Discussion of Measurements inside High-Speed Thunderstorm Updrafts, J. Appl. Meteor., 13, 710-717.

Davis, P.A., 1974: Application of satellite imagery to estimates of precipitation over northwestern Montana. Stanford Research Institute, Standford, Calif., 90 pp.

Doswell, C.A., III, and L.R. Lemon, 1979: An operational evaluation of certain kinematic and thermodynamic parameters associated with severe thunderstorm environments. Preprints, 11th Conf. on Severe Local Storms, Kansas City, Amer. Meteor. Soc., 397-402.

Droegemeier, K., and R.B. Wilhelmson, 1983: Three dimensional numerical simulation of the interaction between a shallow cumulus field and thunderstorm outflow boundary. Preprints, 13th Conf. on Severe Local Storms, Tulsa, Amer. Meteor. Soc., 245-248.

Esbensen, S., 1978: Bulk thermodynamic effects and properties of small tropical cumuli. J. Atmos. Sci., 35, 826-837.

Espy, J.P., 1841: The Philosophy of Storms, Charles C. Little & James Brown Co., 347 pp.

Fankhauser, J., 1971: Thunderstorm-environment determined from aircraft and radar observations. Mon. Wea. Rev., 99, 171-192.

Foltz, G.S. and W.M. Gray, 1979: Diurnal variation in the troposphere's energy balance. J. Atmos. Sci., 36, 1450-1466.

Fujita, T.T., 1955: Results of detailed synoptic studies of squall lines. Tellus, 7, 405-436.

Fujita, T.T., 1959: Precipitation and cold air production in mesoscale thunderstorm systems. J. Meteorol., 16, 454-466.

Fujita, T.T., 1978: Manual of downburst identification for Project NIMROD. SMRP Research Paper No. 156, Univ. of Chicago, 103 pp.

Goff, C.R., 1976: Vertical structure of thunderstorm outflows. Mon. Wea. Rev., 104, 1429-1440.

Gray, W.M., 1973: Cumulus convection and larger scale circulations I. Broadscale and mesoscale considerations. Mon. Wea. Rev., 101, 839-855.

Griffith, C.G., W.L. Woodley and P.G. Grube, 1978: Rain estimation from geosynchronous satellite imagery -- Visible and infrared studies. Mon. Wea. Rev., 106(8), 1153-1171.

Gurka, J.J., 1976: Satellite and surface observations of strong wind zones accompanying thunderstorms. Mon. Wea. Rev., 104, 1484-1493.

Hayden, C.M. and Brian F. Taylor, 1985: The application of AVHRR data to fine scale temperatuer and moisture retrievals obtained from NOAA satellites. Preprints, 14th Conf. on Severe Local Storms, Indianapolis, Amer. Meteor. Soc., J22-J28.

Hess, S.L., 1959. Introduction to Theoretical Meteorology, Holt, Rinehart and Winston, New York, 362 pp.

Hillger, D.W. and T.H. Vonder Haar, 1981: Retrieval and use of high-resolution moisture and stability fields from Nimbus 6 HIRS radiances in pre-convective situations. Mon. Wea. Rev., 109, 1788-1806.

Hillger, D.W., J.F.W. Purdom and T.H. Vonder Haar, 1985: An anlysis of various mesoscale air masses for 28 March 1984 using NOAA-7 TOVS. Preprints, 14th Conf. on Severe Local Storms, Indianapolis, Amer. Meteor. Soc, 36-39.

Holle, R.L. and M. Maier, 1980: Tornado formation from downdraft interaction in the FACE mesonetwork. Mon. Wea. Rev., 108, 1010-1028.

Humphreys, W.J., 1914: The thunderstorm and its phenomena. Mon. Wea. Rev., 42, 348-380.

Jensen, O.N. and D.H. Lenschow, 1978: An observational investigation of penetrative convection. J. Atmos. Sci., 35, 1924-1933.

Kellogg, W.W., 1982: Early satellite program developments. The Conception, Growth, Accomplishments and Future of Meteorological Satellites. NASA Conf. Pub. 2257, NASA, Scientific and Technical Information Branch, Washington, DC, 101 pp.

Keulegan, G.H., 1958: The motion of saline fronts in still water. 12th Progress Report on Model Laws for Density Currents, U.S. Nat. Bur. Standards, No. 5831.

Klemp, J.B. and R.B. Wilhelmson, 1978: The simulation of three-dimensional convective storm dynamics. J. Atmos. Sci., 35, 1070-1096.

Kuettner, J., 1959: The band structure of the atmosphere. Tellus, 11, 267-294.

Kuettner, J., 1971: Cloud bands in the earth's atmosphere: Observations and theory. Tellus, 23, 406-425.

Leverson, V.H., P.C. Sinclair and J.H. Golden, 1977: Waterspout wind, temperature and pressure structure deduced from aircraft measurements. Mon. Wea. Rev., 105(6), 725-732.

Lilly, D.K. (ed.), 1977: Project SESAME: Planning documentation volume. NOAA/ERL, U.S. Department of Commerce, Boulder, CO, 308 pp.

Lopez, R.E., 1972: Cumulus convection and larger-scale circulations, part I. Atmospheric Science Paper No.188, Department of Atmospheric Science, Colorado State University, Ft. Collins, CO., 100 pp.

Maddox, R.A., et al., 1979: A study of thermal boundary/severe thunderstorm interactions. Preprints, 11th Conf. on Severe Local Storms, Kansas City, Amer. Meteor. Soc., 401-410.

Maddox, R.A., 1980: Mesoscale convective complexes. Bull. Am. Meteor. Soc., 61, 1374-1387.

Middleton, G.V., 1966: Experiments on density and turbidity currents, I. Motion of the head. Can. J. Earth Sci., 3, 523-546.

Miller, R.C., 1972: Notes on analysis and severe-storm forecasting procedures of the Air Force Global Weather Central. AWS Technical Report 200 (rev), Air Weather Service (MAC), U.S. Air Force, 190 pp.

Mitchell, K.E. and J.B. Hovermale, 1977: A numerical investigation of the severe thunderstorm gust front. Mon. Wea. Rev., 105, 657-675.

National Climatic Data Center, 1983. Storm Data, 25, (12). Ashville, NC, December, 1983.

Negri, A.J. and R. Adler, 1981: Relation of satellite-based thunderstorm intensity to radar-estimated rainfall. J. Appl. Meteor., 20, 66-78.

Newton, C.W., 1966: Circulations in large sheared cumulonimbus. Tellus, 18, 699-713.

Paltridge, G.W. and C.M.R. Platt, 1976. Radiative Processes in Meteorology and Climatology, Elsevier Scientific Publishing Co., New York, 318 pp.

Parker, H.A. 1983; An analysis of the thunderstorm overshooting-top phenomena. ATS Paper 372, M.S. Thesis, Colorado State University, 100 pgs.

Parker, W.T. and R.D. Hickey, 1980: The Cheyenne tornado of 16 July 1979. Nat. Wea. Digest, 5, 45-62.

Petersen, R.A. and A. Mostek, 1982: The use of VAS moisture channels in delineating regions of potential convective instability. Preprints, 12th Conf. on Severe Local Storms, San Antonio, Amer. Meteor. Soc., 168-171.

Pielke, R.A., 1984: Mesoscale Meteorological Modeling, Academic Press, Inc., New York, 599 pp.

Pryor, S.P., 1978: Measurement of thunderstorm cloud-top parameters using high-frequency satellite imagery. M.S. Thesis, Dept. of Atmospheric Science, Colorado State University, Fort Collins, CO, 101 pp.

Purdom, J.F.W., 1971: Satellite imagery and severe weather warnings. Preprints, 7th Conf. on Severe Local Storms, Kansas City, Amer. Meteor. Soc., 120-127.

Purdom, J.F.W., 1973: Meso-highs and satellite imagery. Mon. Wea. Rev., 101, 180-181.

Purdom, J.F.W., 1974: Satellite imagery applied to the mesoscale surface analysis and forecast. Preprints, 5th Conf. Weather Forecasting and Analysis, St. Louis, Amer. Meteor. Soc., 63-68.

Purdom, J.F.W., 1976: Some uses of high-resolution GOES imagery in the mesoscale forecasting of convection and its behavior. Mon. Wea. Rev., 104, 1474-1483.

Purdom, J.F.W., 1979: The development and evolution of deep convection. Preprints, 11th Conf. on Severe Local Storms, Kansas City, Amer. Meteor. Soc., 143-150.

Purdom, J.F.W., 1982: Summary report: Satellite Facilities Committee. Proceedings, 6th Annual Workshop on Meteorological and Environmental Inputs to Aviation Systems, 26-28 Oct., University of Tennessee Space Institute, Tullahoma, TN.

Purdom, J.F.W., 1985: The application of satellite sounding and image data to the Carolina tornado outbreak of 28 March 1984. Preprints, 14th Conf. on Severe Local Storms, Indianapolis, Amer. Meteor. Soc.

Purdom, J.F.W. and J.G. Gurka, 1974: The effect of early morning cloud cover on afternoon thunderstorm development. Preprints, 5th Conf. on Weather Forecasting and Analysis, St. Louis, Amer. Meteor. Soc., 58-60.

Purdom, J.F.W. and K. Marcus, 1982: Thunderstorm trigger mechanisms over the southeast United States. Preprints, 12th Conf. on Severe Local Storms, San Antonio, Amer. Meteor. Soc., 487-488.

Purdom, J.F.W. and T.H. Vonder Haar, 1983: Product user's guide, enhancing GOES infrared imagery for nowcast applications. Cooperative Institute for Research in the Atmosphere, Colorado State University, Ft. Collins, CO, 21 pp.

Purdom, J.F.W., R.N. Green and H.A. Parker, 1982: Integration of satellite and radar data for short range forecasting and storm diagnostic studies. Preprints, 9th Conf. Weather Forecasting and Analysis, Seattle, Amer. Meteor. Soc., 100-105.

Schereschewsky, P., 1945: Clouds and states of the sky. Handbook of Meteorology, (ed. by Berry, Bollay and Beers), McGraw-Hill, New York, 1068 pp.

Segal, M. and J.F.W Purdom, J.L. Song, R.A. Pielke, and Y. Mahrer, 1986. Evaluation of cloud shading effects on the generation and modification of mesoscale circulations, Mon. Wea. Rev., May (12 pgs).

Seiter, K.L., 1983: The effect of arc cloud generation on thunderstorm gust front motion. Preprints, 13th Conf. on Severe Local Storms, Tulsa, Amer. Meteor. Socl, 249-252.

Shapiro, M.A., T. Hampel, D. Rotzoll and F. Mosher, 1985: The Frontal Hydraulic Head: A Micro-α Scale (~ 1 km) Triggering Mechanism for Mesoconvective Weather Systems. Mon. Wea. Rev., 113, 1166-1183

Simpson, J.E., 1969: A comparison between laboratory and atmospheric density currents. Quart. J. Roy. Meteor. Soc., 95, 758-765.

Simpson, J.E., 1972: Effects of the lower boundary on the head of a gravity current. J. Fluid Mech., 53, 759-768.

Simpson, J.S. and A.S. Dennis, 1974: Cumulus clouds and their modification. Weather Modification, (W.N. Hess, ed.), Wiley, New York, 229-280.

Sinclair, P.C., 1969: Vertical motion and temperature structure of severe convective storms. Preprints, Sixth Conf. Thunderstorm Phenomena, Severe Local Storms, Chicago, Amer. Meteor. Soc., 346-350.

Sinclair, P.C., 1973: Severe storm air velocity and temperature structure deduced from penetrating aircraft. Preprints, 8th Conf. on Severe Local Storms, Denver, Amer. Meteor. Soc., 25-32.

Sinclair, P.C., 1974: Severe storm turbulent energy structure. Preprints, Sixth Conf. on Aerospace and Aeronautical Meteorology, El Paso, Amer. Meteor. Soc., 13 pp.

Sinclair, P.C. and J.F.W. Purdom, 1982: Integration of research aircraft data and 3 minute interval GOES data to study the genesis and development of deep convective storms. Preprints, 12th Conf. on Severe Local Storms, San Antonio, Amer. Meteor. Soc., 269-271.

Sinclair, P.C. and J.F.W. Purdom, 1983: The genesis and development of deep convective storms. CIRA Paper No. 1, Cooperative Institute for Research in the Atmosphere, Colorado State University, Ft. Collins, CO, 56 pp.

Sinclair, P.C. and J.F.W. Purdom, 1984: The genesis and development of deep convective storms: A new approach to their prediction and possible modification. CIRA, Cooperative Institute for Research in the Atmosphere, Colorado State University, Ft. Collins, CO, 47 pp.

Smith, W.L., V.E. Suomi, W.P. Menzel, H.M. Woolf, L.A. Stromousky, H.E. Revercomb, C.M. Hayden, D.N. Erickson and F.R. Mosher, 1981: First sounding results from VAS-D. Bull. Amer. Meteor. Soc., 62, 232-236.

Tepper, M., 1950: A proposed mechanism of squall lines: The pressure jump line. J. Meteor., 7, 21-29.

Tepper, M., 1955: On the generation of pressure jump lines by the impulsive addition of momentum to simple current systems. J. Meteor., 12, 287-297.

von Karmen, T., 1940: The engineer grapples with nonlinear problems. Bull. Am. Math. Soc., 46, 615-683.

Wakimoto, R.M., 1982: The life cycle of thunderstorm gust fronts as viewed with doppler radar data. Mon. Wea. Rev., 110, 1060-1082.

Wallace, J.M., 1975: Diurnal variations in precipitation and thunderstorm frequency over the conterminous United States. Mon. Wea. Rev., 103, 406-419.

Weaver, John F. and Stephan P. Nelson, 1982: Multiscale aspects of thunderstorm gust fronts and their effects on subsequent storm development, Mon. Wea. Rev., 110(7).

Weiss, C.E. and Purdom, J.F.W., 1974: The effect of early morning cloud cover on squall line activity. Mon. Wea. Rev., 102, 400-401.

Willett, H.C., 1938: Characteristic properties of North American air masses. An Introduction to the Study of Air Mass Analysis. (Jerome Namias, ed.), October 1938, American Meteorological Society, 65-100.

Wilson, J. and R. Carbone, 1984: Nowcasting with Doppler radar: forecaster-computer relationship. Preprints, Nowcasting II Symposium, Norrkoping, Sweden, European Space Agency, 177-186.

Zehr, R.M., 1982: Thunderstorm motion analyses. Preprints, 9th Conference on Weather Forecasting and Analysis, Seattle, Amer. Meteor. Soc., 455-458.

Zehr, R.M., 1986: Analysis of mesoscale air masses with VAS retrievals. Preprints, 2nd Conference on Satellite/Remote Sensing and Applications, Clearwater Beach, Amer. Meteor. Soc., 94-98.

Zipser, E.J., 1984: The National STORM program STORM central phase preliminary program design. National Center for Atmospheric Research, Boulder, CO, 147 pp.